# POLITECNICO DI TORINO

## MASTER's Degree in ELECTRICAL ENGINEERING


*MASTER's Degree Thesis*

# FINITE ELEMENT MODELING AND ANALYSIS OF A THREE-PHASE INDUCTION MOTOR UNDER AMBIENT AND CRYOGENIC CONDITIONS

**Supervisors:**

Prof. Silvio VASCHETTO

Prof. João Filipe Pereira FERNANDES

Prof. Inês Santos Perdigão PEIXOTO

**Candidate:**

Vittorio COLAIEMMA

**July 2025**

# Abstract

The worldwide energy transition is accelerating the electrification of industrial and transport networks. In this scenario, new technologies must be adopted to meet the new technological challenges. Cryogenic cooling leads to important performance increases in electric motors, making them suitable for specific types of application such as future electric aircraft, superconducting machines, or Liquefied Natural Gas (LNG) pumping systems, where their potential is most effectively harnessed due to the cryogenic environment already available. In these cases, the added cooling infrastructure already present allows the performance benefits to be harnessed without introducing excessive complexity or cost.

The thesis investigates the performance of a 15 kW squirrel-cage induction motor under ambient and cryogenic temperatures to evaluate the performance improvement offered by cryogenic cooling. The motor is modeled using the finite element method in COMSOL Multiphysics. Experimental validation is carried out by no-load, locked-rotor, and load tests available for the real machine, following IEEE Std 112-1991 standards. Particular care is taken while matching important parameters such as the air-gap and the rotor bridges, taking into account also 3D elements to make the model as accurate as possible.

The torque-speed curve is obtained by imposing a set of constant load torques on the machine and simulating the corresponding dynamic balance. The results show that cryogenic operation significantly improves motor performance in terms of efficiency and torque, demonstrating the potential of cryogenically cooled induction motors for important specific applications.

# Contents

# List of Figures

# 1 Introduction

New and more challenging engineering problems are constantly emerging as a result of the rapid technological advancement. Industrial automation, energy and aerospace are at the center of this development, requiring more compactness, environmental restrictions, harsh operating conditions, and greater efficiency. In most of these cases, the available technologies are pushed to their limits, and custom solutions must be created to provide performance levels that are outside the capabilities of traditional systems. Among these new technologies, cryogenically cooled induction motors are gaining increasing attention. Thanks to the drastic reduction in electrical resistivity, the motors operate with higher efficiency, higher torque density, and better thermal stability. Although not appropriate for general use, they are an extremely valuable solution where optimal performance or compatibility in cryogenic environments is required.

In the literature, various studies explore the consequences of cryogenic cooling on induction motors using experimental measurements and laboratory tests by comparing a typical machine with a cryogenically cooled counterpart[12] [3], showing the possible benefits of cryogenic operation. However, it is relatively uncommon to find this kind of comparison using finite element modeling. Most of the analysis that has taken place is experiment-based, and only few of them use Finite Element Model (FEM). This thesis attempts to do this by designing and calibrating a FEM model of the original machine, and studying then its behavior at cryogenic temperatures.

Although the overall theme of this thesis is that of the electromagnetic performance of the motor at cryogenic temperatures, it is interesting to present a general overview of the role that these motors currently have in the engineering and industrial context.

## 1.1 The Strategic Importance of Electric Motor Efficiency

According to the *International Energy Agency's report Walking the Torque: Proposed Work Plan for Energy-Efficiency Policy Opportunities for Electric Motor-Driven Systems (2011)*[18], Electric Motor-Driven Systems (EMDS) consume more than $40\%$ of the world's electricity, rising up to two thirds in industrial applications, representing one of the largest users of electrical energy in the world.

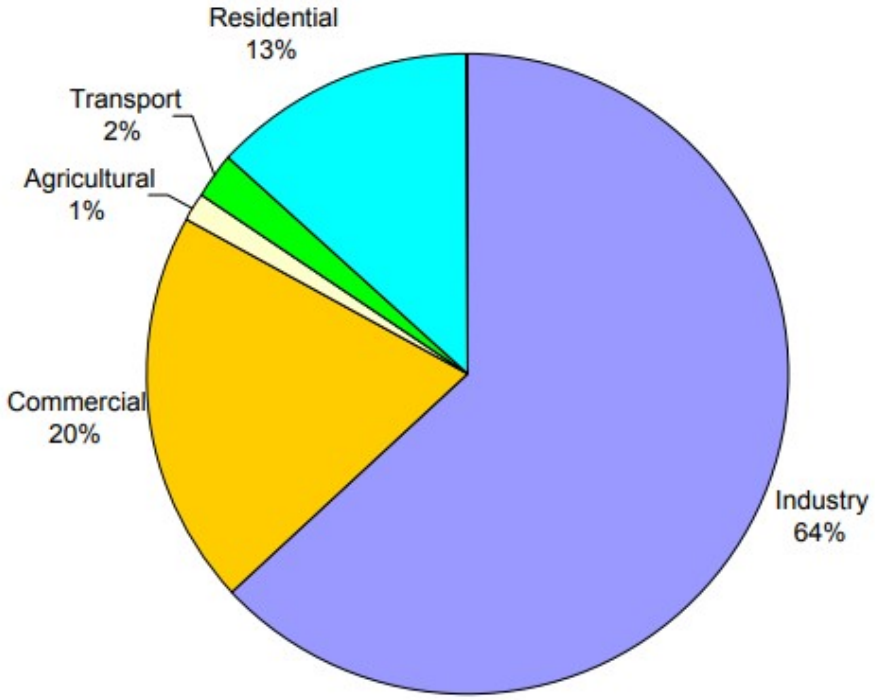


**Figure 1:** EMDS energy use by sector[18].

Although they are universal in their use and their technology is mature, there are great opportunities to improve their efficiency, particularly in the realm of motor selection, sizing, operation, and cooling. In fact, the potential to improve energy efficiency of motor systems is in the order of $20\%$ to $30\%$.

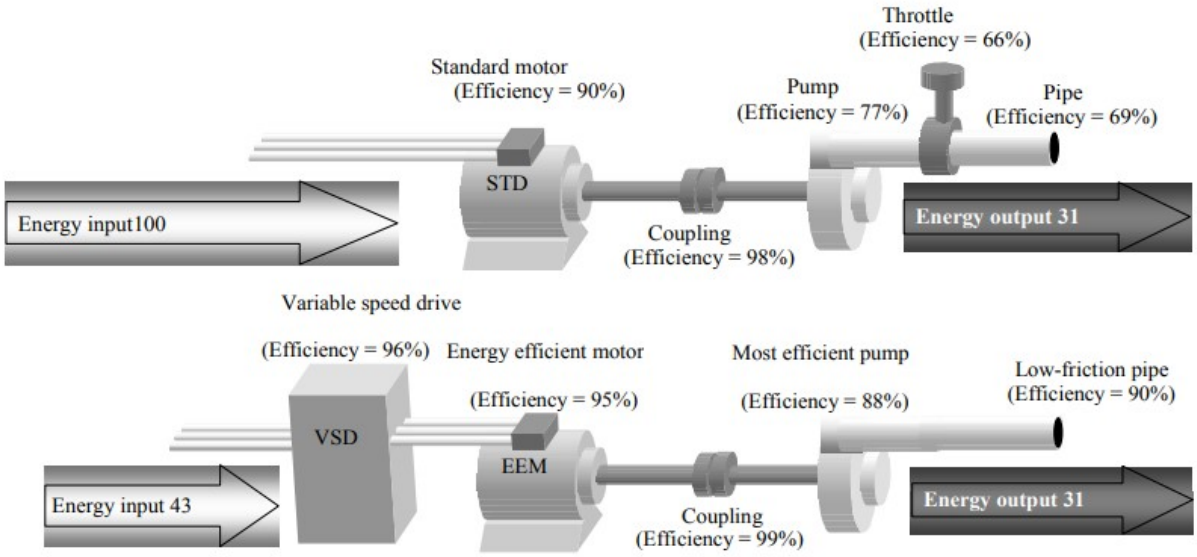


**Figure 2:** Components of the Motor System, showing the relevance of System Optimization[18].

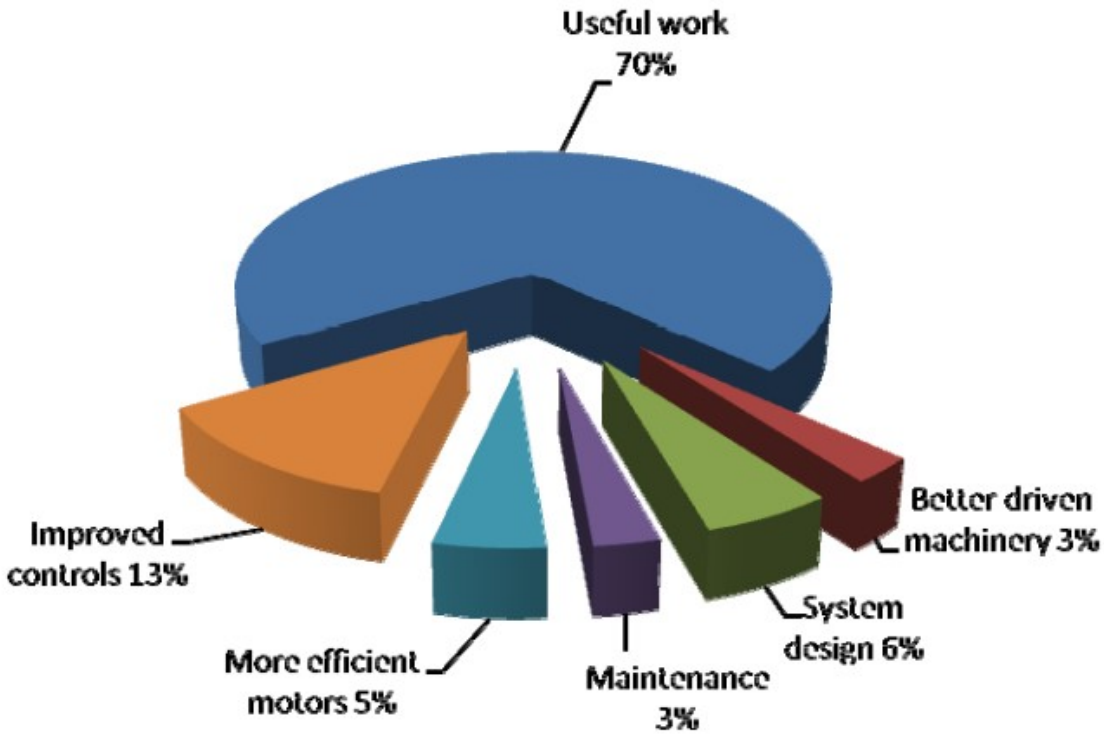


**Figure 3:** Potential for Energy Savings in EMDS[18].

The IEA has estimated that cost-effective improvements in energy efficiency in motor-driven systems could save up to 10% of global electricity use, making the idea the scale of the opportunity. These savings are achievable not only through improved system integration and

control, but also through improving the intrinsic performance of the motors themselves. In this case, research on alternative cooling techniques — i.e., cryogenic operation — could be an interesting area of research for future applications (i.e. electric aircraft [39]). Applications where cryogenic motors are most successful are scenarios where a cryogenic environment is already available, such as Liquefied Natural Gas (LNG) pumping systems[19][4], as explained in Sec.1.3.1. In these cases, the added cooling infrastructure already present allows the performance benefits to be harnessed without introducing excessive complexity or cost.
A cryogenic motor is a motor that operates at cryogenic temperatures thanks to special cooling systems. This type of technology has considerable advantages, principally: a significant decrease in stator and rotor resistances followed by decreases in joule losses; an increased efficiency, also due to the higher rotational speeds at which a cryogenic motor operates at the same torque as a conventional one; a high power and torque density, which allows to obtain the same performance using much smaller volumes; possibility of having a maximum torque value much higher than the standard one. However, the disadvantages must also be carefully managed: greater losses in iron due to its increased electrical conductivity; greater mechanical losses due to the friction of the cryogenic fluid in the motor; lower starting torque due to the decrease in rotor resistance; high complexity and cost of the cooling system, which represents a fundamental part of the motor. In this sense, the main types of cooling for a cryogenic machine are analyzed below.

## 1.2 Cryogenic Cooling Techniques for Electric Machines

A fluid is considered "cryogenic" when its boiling point lies below $-150\ ^{\circ}C$ (123 K) under atmospheric pressure. Among the most widely used cryogenic fluids, there is liquid nitrogen ($LN_2$) with a boiling temperature of $77K$ ($-196\ ^{\circ}C$). It is widely utilized, inert, non-toxic, and comparatively inexpensive, making it an economical choice for cooling electric motors that do not require superconducting environments. Liquid helium ($LHe$) with a much lower boiling temperature of 4.2 K is widely used in superconducting systems, but due to its high cost and complexity of handling, its utilization is limited to some scientific and aerospace environments.
Various cooling methods have been developed for electric machines in cryogenic operation, each with its strengths and weaknesses depending on the application and type of machine.

As noted in *"Perspectives on Electric Machines with Cryogenic Cooling"*[27], the most common cryogenic cooling methods are the following:

- **Cryocoolers**: Small-scale refrigeration units capable of reaching cryogenic temperatures (below 120K). They operate in a closed cycle and incorporate technologies such as Gifford–McMahon, Stirling, or pulse tube cycles. They are especially appropriate for low-power or laboratory-scale superconducting devices.

- **Forced-flow cooling**: In this technology, liquid nitrogen ($LN_2$) or liquid helium ($LHe$) is actively circulated through channels inside the machine to abstract heat. It can be applied in stator and rotor windings and allows for continuous operation at well-stable lower temperatures. Developments like rotary cryocoolers placed inside the shaft are also being studied.

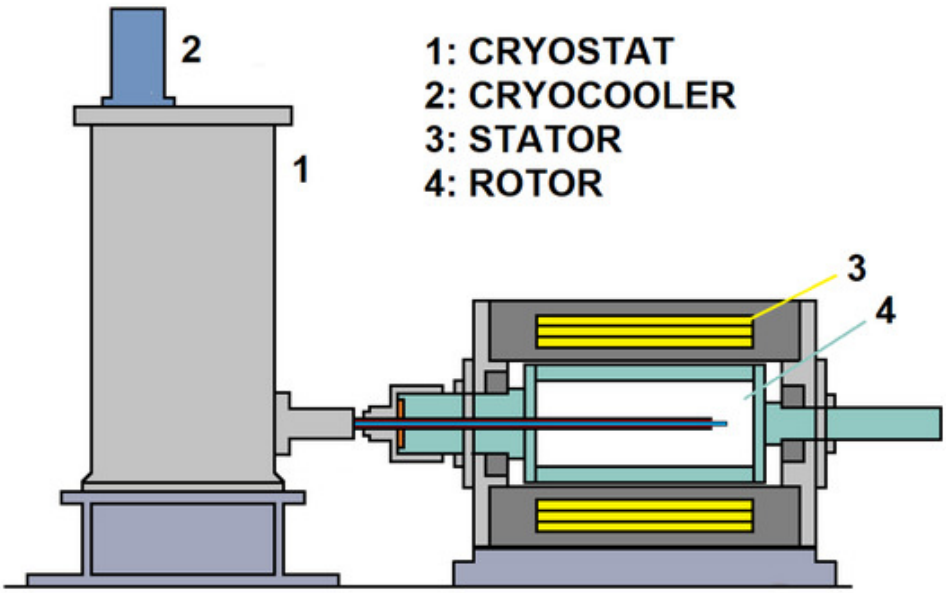


**Figure 4:** Electric machine with rotating cryostat for rotor cooling[27].

- **Immersion cooling**: The windings are completely submerged in a bath of $LN_2$ or $LHe$. This technique has high efficiency and good thermal contact but complex insulation and containment systems.

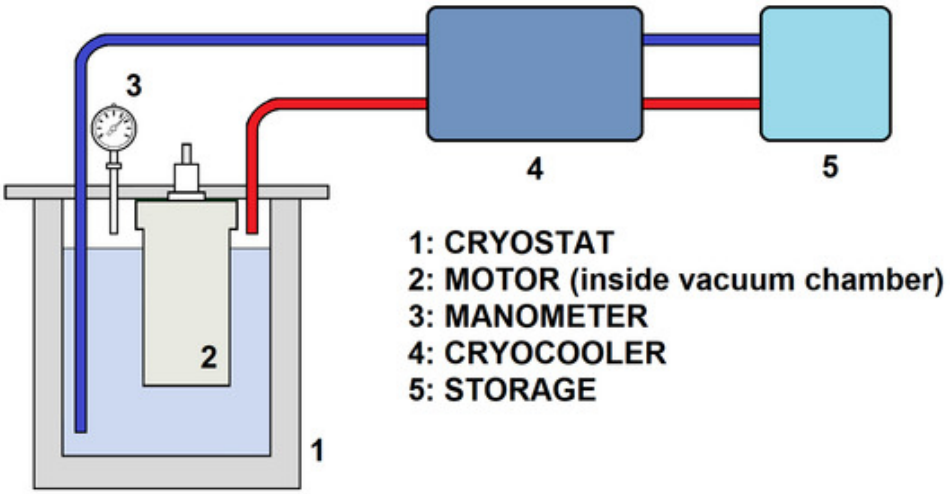


**Figure 5:** Electric machine cooled in the cryostat[27].

- **Pumped Two-Phase ($P2P$) cooling**: Both phases of a cryogenic fluid, liquid and gaseous, are employed. The liquid absorbs heat, while the gas phase transports it away. The process has high heat transfer effectiveness and good control.

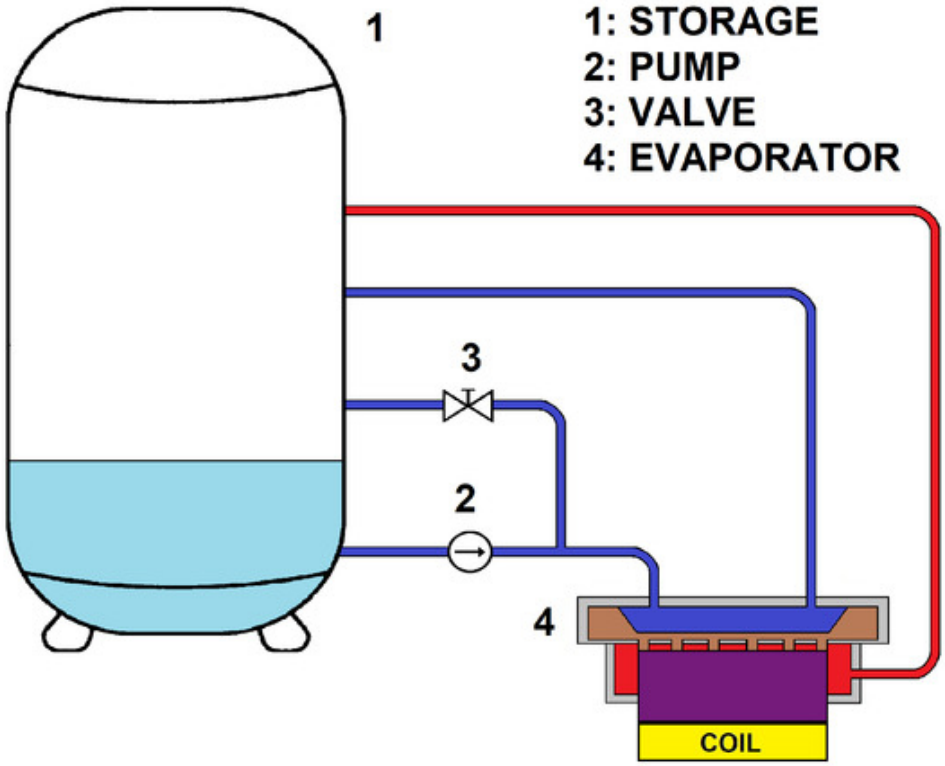


**Figure 6:** Typical structure of the pumped two-phase ($P2P$) cooling[27].

- **Spray cooling**: $LN_2$ is sprayed directly onto stator windings. It is simpler to apply, but it offers less efficiency than immersion.

The choice between these methods is determined by factors such as the machine's power level, available space, heat load, and whether the application has to be portable or fixed. Higher-power machines have a tendency to employ immersion or forced-flow cooling, while cryocoolers are common in small or portable applications.

## 1.3 Main Applications of Cryogenic Motors

### 1.3.1 LNG: Liquefied Natural Gas

The use of cryogenic IMs is strictly related to that of submerged cryogenic pumps, which play a fundamental role in the transport of cryogenic fluids such as liquid hydrogen ($LH_2$), liquid nitrogen ($LN_2$) or liquefied natural gas ($LNG$)[4].
LNG and natural gas are some of the keys that could enable the energy transition from sources such as coal or heavy fossil fuels to renewable sources. In power generation, for example, it emits $45\%$ to $55\%$ less greenhouse gases than coal[19]. Its use is of great interest in various applications: in the industrial sector, for example, LNG represents a good opportunity where high calorific fuels are requested in the production process with a greater reluctance to electrification. Moreover, it represents an alternative solution to traditional biomass in heating and cooking, but also LNG can lead to a significant reduction in emissions and pollution in the transport sector. Therefore, LNG plays a central role in the energy transition, with the IEA estimating that natural gas use will increase by $45\%$ over the next 25 years[19].

**Figure 7:** Transportation of LNG

LNG must be transported and stored at very low temperatures (around $162\ ^{\circ}C$), so any equipment that works directly with the fluid — such as submerged pumps — must be built to survive and operate under cryogenic conditions. Thus, direct immersion-cooled induction motors employing LNG or cryogenic integrated systems have several advantages. The cost and effort associated with the installation of low-temperature systems is considerably minimized because the cryogenic environment is already present. Furthermore, the very low temperature of LNG represents a ”natural” way to cool the motor, maintaining low resistive losses and increasing torque density without the need for active refrigeration.
In an LNG transport system, a cryogenic induction machine can have several key roles. For example, this type of cryogenic motor is used in pumps that transfer liquefied natural gas from cargo ships to their respective destinations. Various motor prototypes coupled with pumps are available on the market, making this technology ideal for this type of application.

**Figure 8:** DEMSI - Deepwell Cargo and Booster Pumps for Gas Carriers.

In *"Electrical motor for liquid gas pump"*[16][23] it is presented the design and investigation of performance characteristics of 3-phase high voltage squirrel-cage submerged motor. The objective of the motor is to feed a cryogenic pump useful to unload the tanks of a LNG cargo ship, determining its steady-state and dynamic behavior.

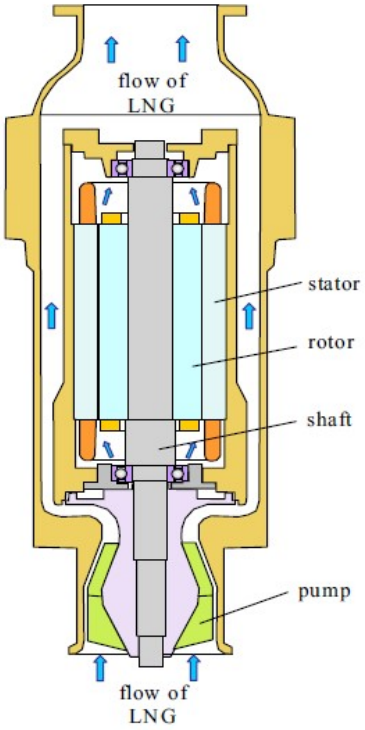


**Figure 9:** Submerged squirrel-cage motor with pump[16].

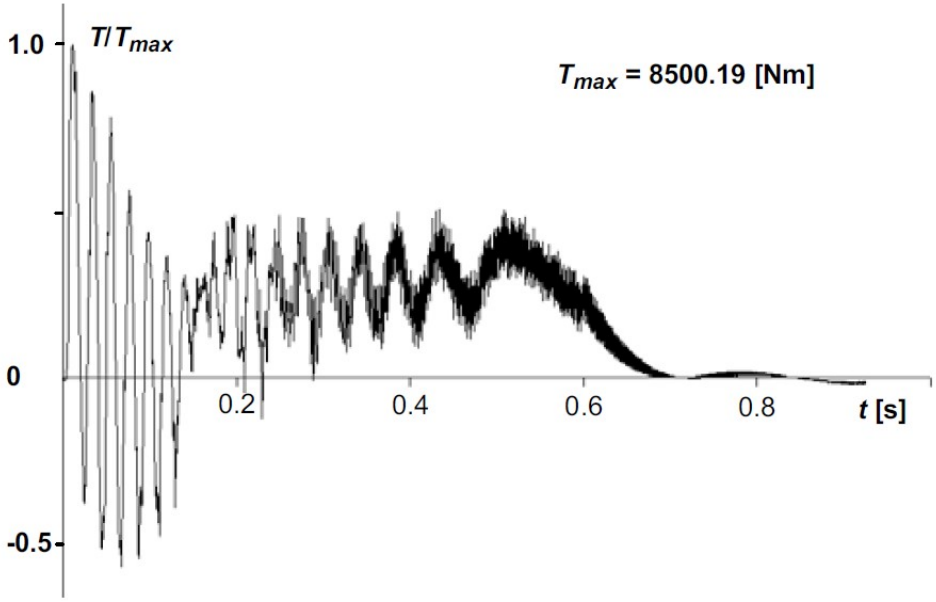


**Figure 10:** Torque time characteristics during starting of no-load motor for $U = 5500\ V$, $f = 50\ Hz$, $T = -196\ °C$ for the Motor Designed in [16].

The methods and software presented in the paper were used to evaluate the performance of the cryogenic motor, taking into account the non-linearity of the magnetic circuit and the

skewing of the slots. The electromagnetic circuit of the motor has a mass about twice smaller than a conventional motor of the same power.

In the literature, there is also an increasing focus on filling the gaps in design, modeling, and analysis strategies of electric machines for cryogenic pumps. An example is shown in *"Design and Analysis of High-Speed Induction Machines for Submerged Cryogenic Pumps"*[4], where an existing three-phase $7300\ rpm$ $7.5\ kW$ induction motor already designed to work with a three-stage cryogenic pump is redesigned to work at a new high-speed of $15000\ rpm$ delivering $15k\ W$ while maintaining the same outer diameter. From Fig.11 it is interesting to note that the flow of LNG follows two parallel paths: the pump flow and the motor flow, which is used to cool the motor and to lubricate the bearings.

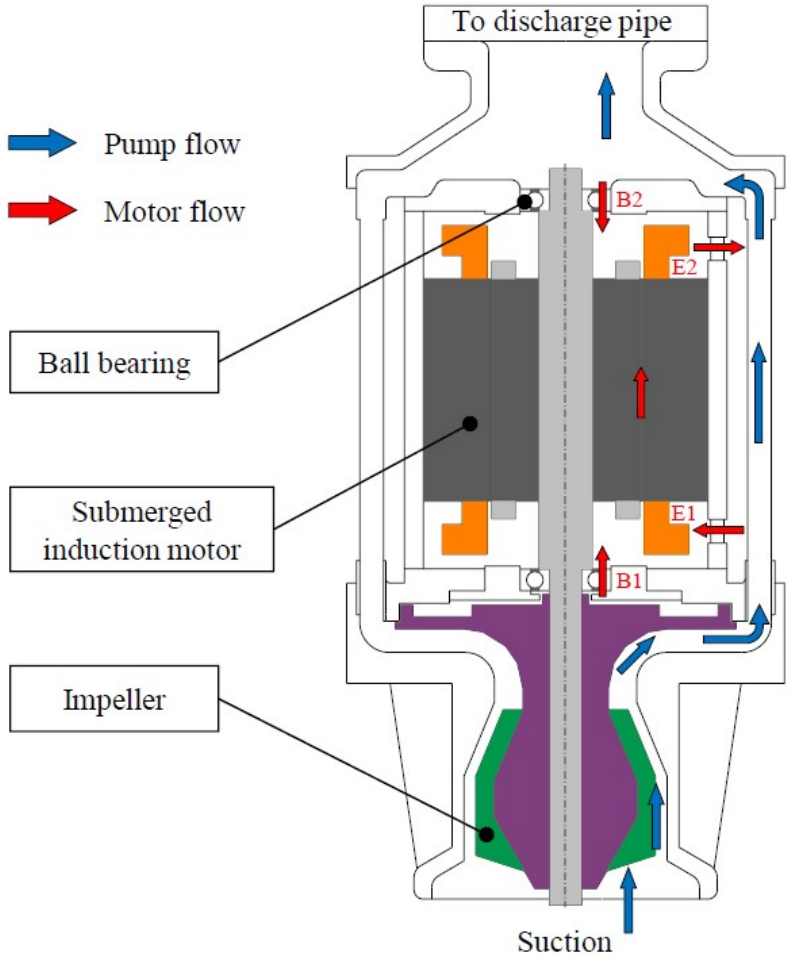


**Figure 11:** Simplified structure of a single-stage submerged cryogenic pump[4].

Moreover, in order to load efficiently LNG into the cargo tanks, a part of it must be sprayed using a pressure pump for cooling inside. In *"Design of Cryogenic Induction Motor Submerged in*

*Liquefied Natural Gas"*[22], the design of a cryogenic induction motor submerged in liquefied natural gas for operating LNG spray pump is presented. The electromagnetic performances of a motor change dramatically from ambient to VLT (Very Low Temperatures). Therefore, in order to obtain the performance characteristics originally desired, it is appropriate to redesign the motor in its most intrinsic aspects: dimensions, shapes of slots and rotor bars, materials and so on. This study shows the benefits of this re-design:

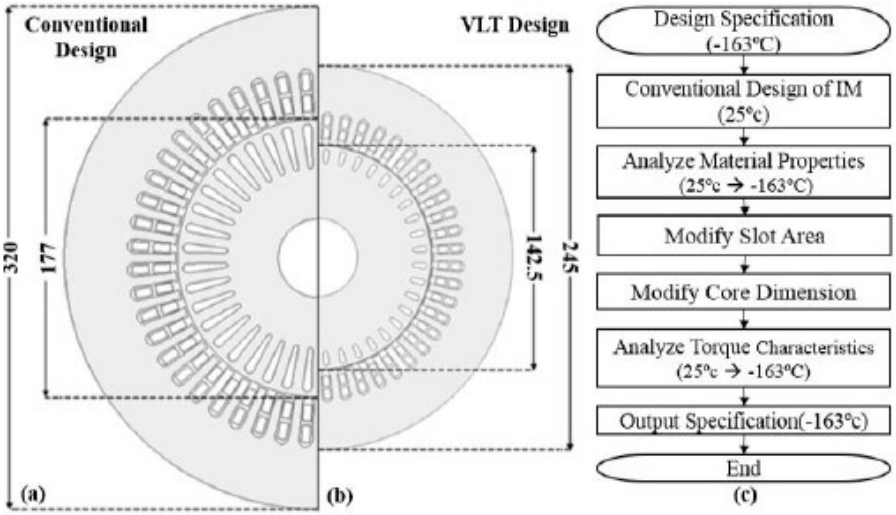


**Figure 12:** Design of cryogenic induction motor. (a) Conventional design. (b) VLT design. (c) Design algorithm.[22]

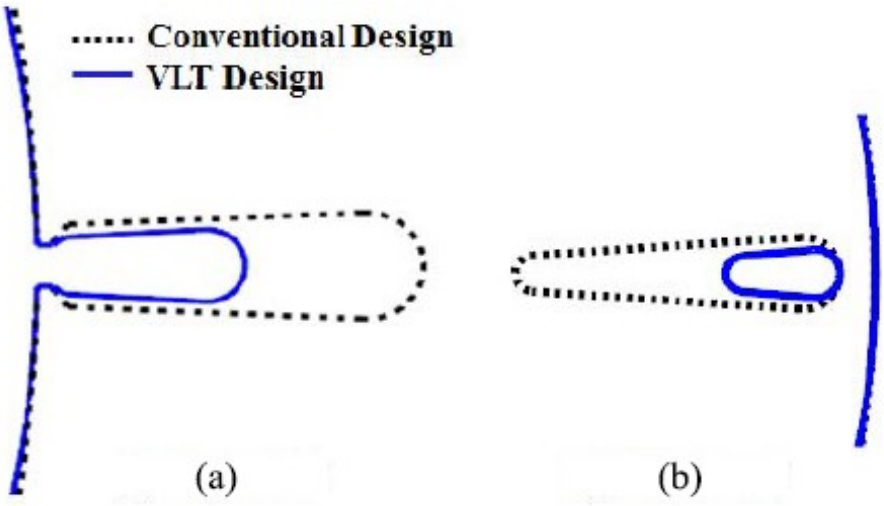


**Figure 13:** Change of slot areas from redesigned process. (a) Stator. (b) Rotor.[22]

In addition, this type of machine can be used as an electrical generator in a critical step of the gas liquefaction process, which consists in reducing rapidly the pressure of the condensate fluid to low levels. Traditionally, it was done using a Joule–Thomson valve (Fig.14).

**Figure 14:** Joule-Thomson Valve

However, it has the drawback of causing a slight temperature rise in the expanded fluid, typically around $1$ to $2$ $^{\circ}C$[33]. They can be replaced by cryogenic turbines that allow a more efficient reduction of pressure during the liquefaction process. In fact, unlike the valves mentioned above, they are able to reduce the kinetic energy of the liquid flow and consequently

reduce the evaporation of the liquid caused by friction losses and heat transfer. By minimizing heat transfer and vaporization, the turbine-driven process can improve the overall process efficiency by up to $5\%$[24]. This increase is particularly valuable in the LNG service, where even small reductions in vaporized product translate into huge energy and cost savings.

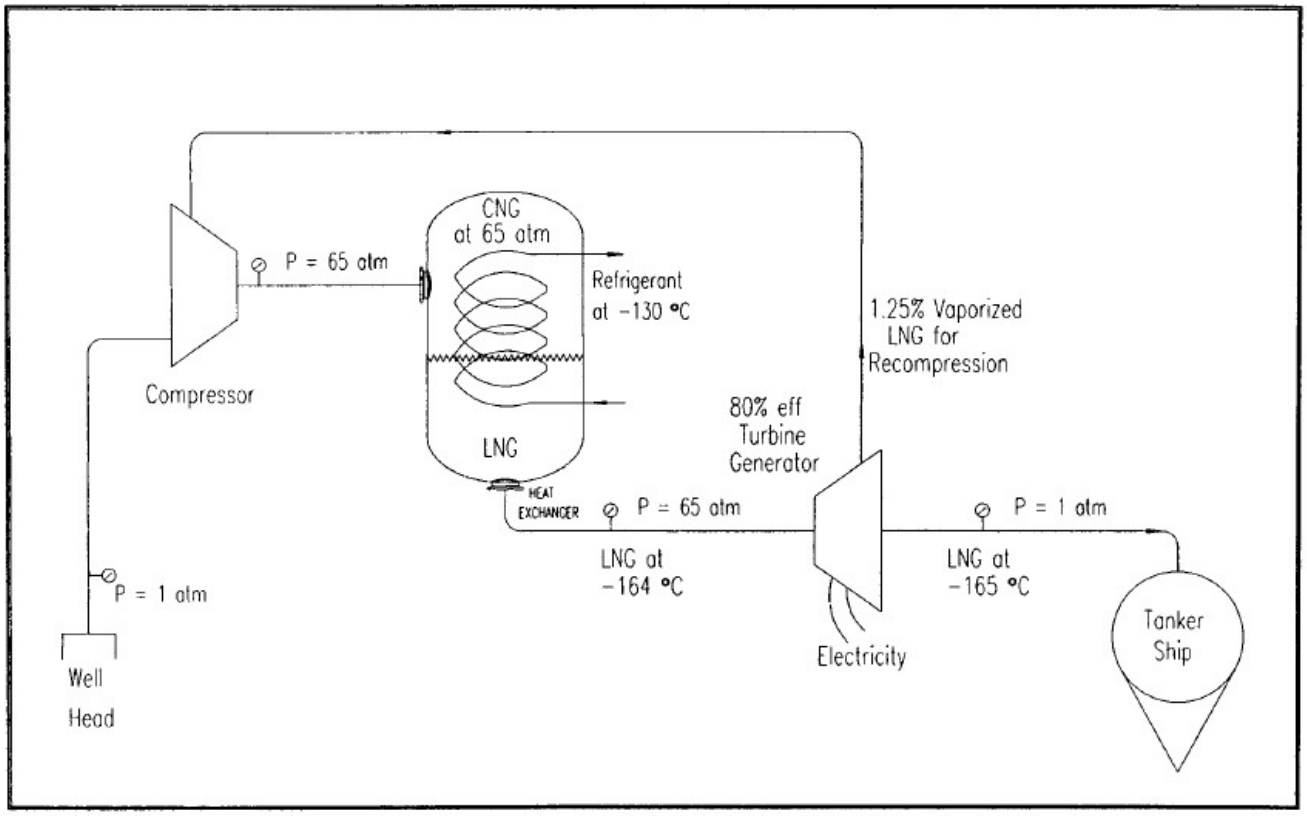


**Figure 15:** Turbine Generator - Process Design[24].

In *"Development of a Submerged Winding Induction Generator for Cryogenic Applications"*[33] is presented the development of a series of 1 MW induction generator to be used while totally submerged in liquid methane at -161°C. In this way, it is possible to increase the overall efficiency by replacing all inline Joule-Thompson expansion valves with cryogenic turbine generators, producing electric power.

### 1.3.2 Aerospace Applications

The aviation sector is under growing pressure from an ecological point of view since it is a large source of greenhouse gas emissions, considering that these are being emitted at higher altitudes, where their effect on the atmosphere is enhanced. In response, the European Commis-

sion launched ambitious de-carbonization projects such as FlightPath 2050[15], whose goals include the $75\%$ $CO_2$ reduction, $90\%$ reduction of $NO_X$, and $65\%$ reduction of emission noise level respect to the current aircraft performances. Altough incremental improvements in conventional gas turbines will contribute to emission reduction, they are not sufficient by themselves to reach these aggressive goals. Thus, electric propulsion systems are increasingly being taken into account as an obligatory technology shift for the future of aviation. Electric machines have the potential to offer a range of environmental benefits: reduced emissions, reduced thermal impact on the atmosphere, reduced noise, and better system reliability. These advantages fit very well into the evolving requirements for sustainable air travel.
A way to replace conventional fuel, thanks to its high specific energy, is liquid hydrogen, using it as a source for a turbofan or in a fuel cell to generate electrical power. Although much work is underway to make the most of hydrogen as an energy source, it remains essential to develop an ultra-efficient electric or hybrid propulsion system for the future aircraft. In this sense, if a cryogenic source like liquid hydrogen is available on board, it can be used in two ways to increase performance of electrical components:

- Cryogenic technologies: Cryogenic cooling alone allows for a significant increase in performance.
- Superconducting technologies (discussed briefly later in Section1.3.3) .

ASCEND project (*Advanced Superconducting and Cryogenic Experimental powertraiN Demonstrator*), led by Airbus, is a notable example which represents the first integrated demonstrator that combines superconducting and cryogenic technology, and low voltage HTS (High-Temperature Superconductor) distribution systems. The project aims to validate a 500 kW cryogenic-electric powertrain with efficiencies in excess of $97\%$, and a power-to-weight ratio more than double that of conventional systems.

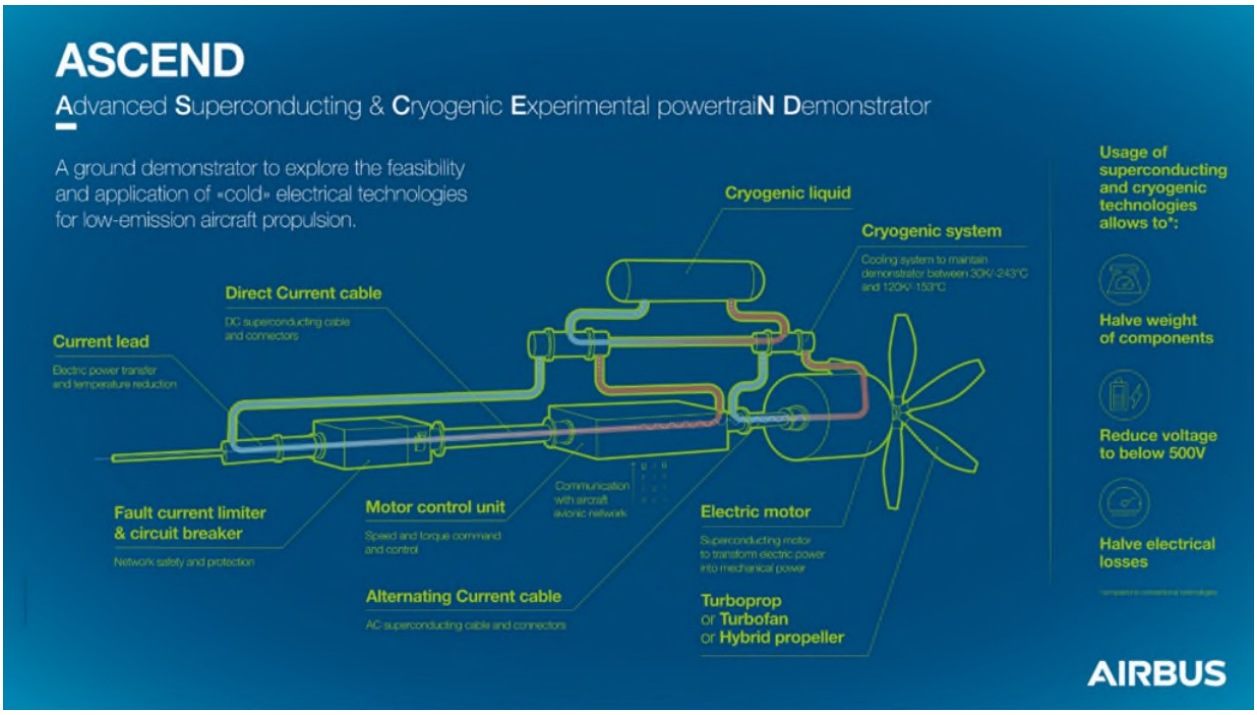


**Figure 16:** ASCEND demonstrator.[39]

Although the ASCEND demonstrator does not yet rely on liquid hydrogen for cooling, its architecture is designed to be compatible with future hydrogen-fueled aircraft, further reinforcing the strategic value of cryogenic electric propulsion. Projects like ASCEND illustrate the potential for cryogenic systems to play a central role in next-generation high-efficiency electric aviation, providing a real-world benchmark for what cryogenically cooled electric machines can achieve when properly integrated and optimized. Various electrified aircraft projects that require cryogenic and HTS technologies on board can give an idea of the potential of these cutting-edge technologies: *"NASA STARC-ABL"*, *"NASA N3-X"*, *"Airbus E-Fan X"* [34].

**Figure 17:** STARC-ABL concept aircraft.[34]

### 1.3.3 Superconducting Electrical Machines

In this section, a brief overview of superconducting machines is given as they are closely related to cryogenic technology and are being developed in parallel with cryogenic motors. Superconductors have almost zero DC electrical resistance at operating temperatures below their critical temperature $T_c$.

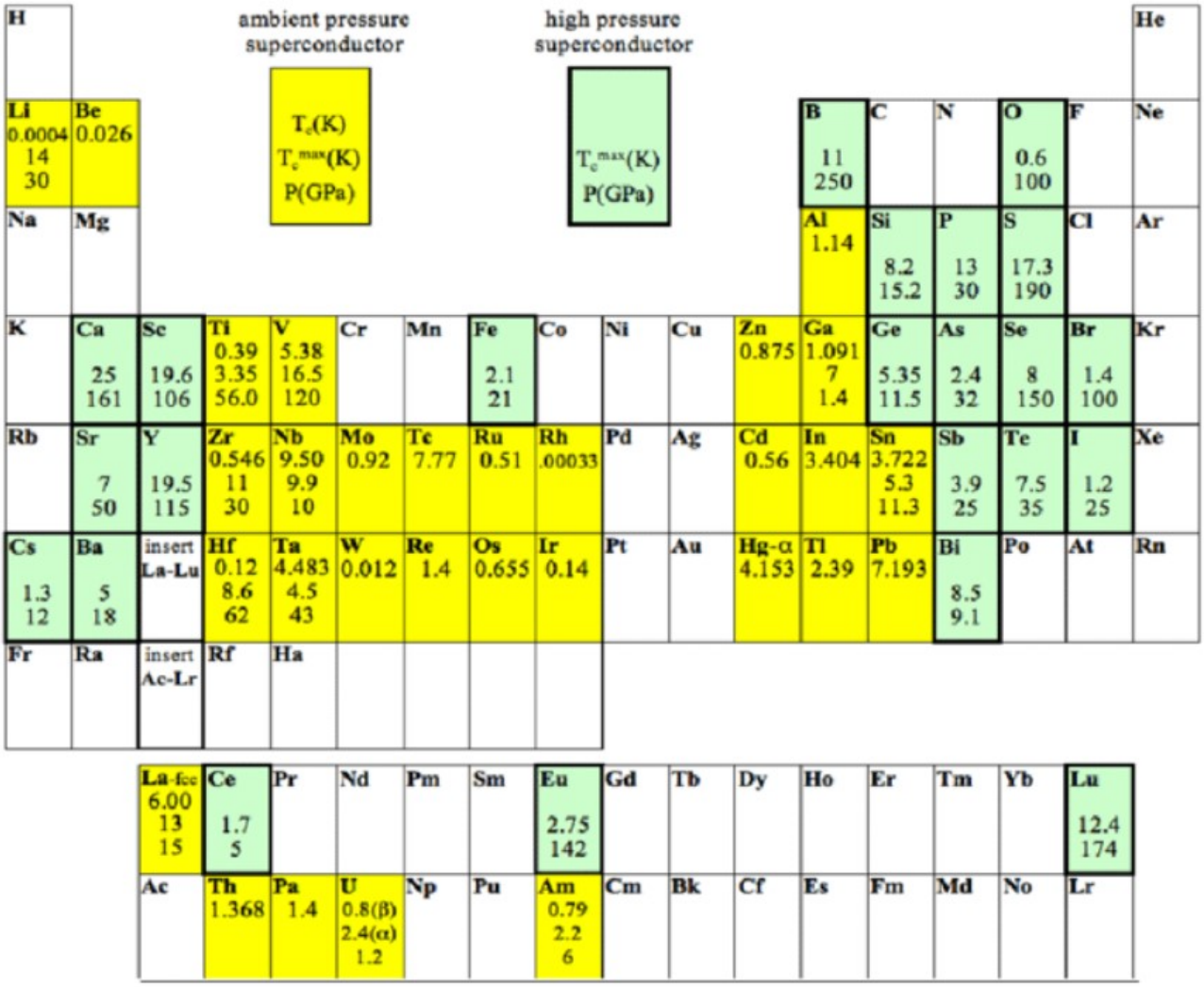


**Figure 18:** Periodic Table of Superconductivity: 30 elements superconduct at Ambient Pressure, 23 more superconduct at High Pressure.[32]

The Superconducting State is characterized by three fundamental parameters (Fig:19):

- critical current density $J_C$;
- critical magnetic field $H_C$;

- critical temperature $T_C$.

If one of these parameters (not constant) is exceeded, the material leaves superconductivity.

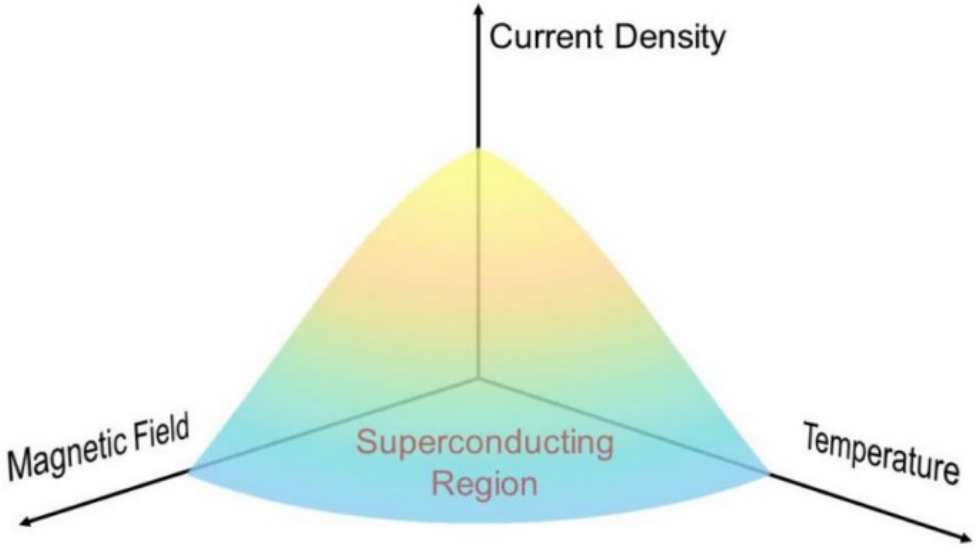


**Figure 19:** Fundamental Parameters of Superconductivity.[1]

They can assume a tape or bulk shape according to their function.

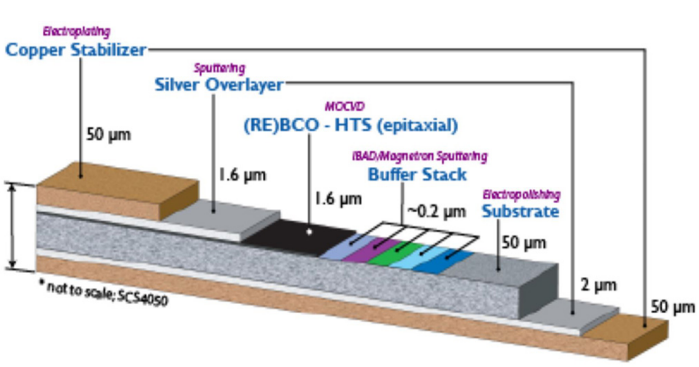


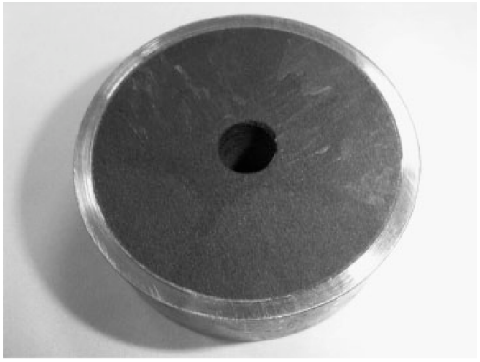

(a) (b)

**Figure 20:** HTS Tape (a) and Bulk (b).[28]

Superconducting materials are divided into:

- **LTS (Low Temperature Superconductors)**: they are ”low temperature” because of the very low critical temperature, up to around 30K. Around 1960, they were used with liquid helium at a temperature of 4.2K. This extreme cooling makes LTS applications extremely complicated and energy- and cost- intensive, leaving to a greater use of HTS in the field of electric motors.

- **HTS (High Temperature Superconductors)**: the "high temperature" refers to the fact that they can be used above 35 K. This new technology allowed for very important developments in the area of electrical applications, especially in electric motors [6, 36, 35, 38].

Since the discovery of superconductors, in 1911, scientists and engineers from all over the world have hardly worked to study their behaviors in many applications. The most popular ones are in medical devices and instruments, such as Magnetic Resonance Imaging (MRI) and Superconducting Quantum Interference Device (SQUID). However, as scientific research advances, the potential of this technology is being demonstrated in more and more forms, such as several electrical power devices like motors, generators, transformers, fault current limiters, power transmission cables, and superconducting magnetic energy storage systems (SMES) [17]. In particular, consistent developments have been conduced in the field of electrical machines adopting this technology. An electrical motor with superconductors, in fact, is able to develop the same power with reduced volume and mass, higher efficiency and reduced losses, making them suitable for special applications where reduced weight and high power density are required (AirCraft, Ship Propulsion[21][37], Wind Turbines[25] etc.)

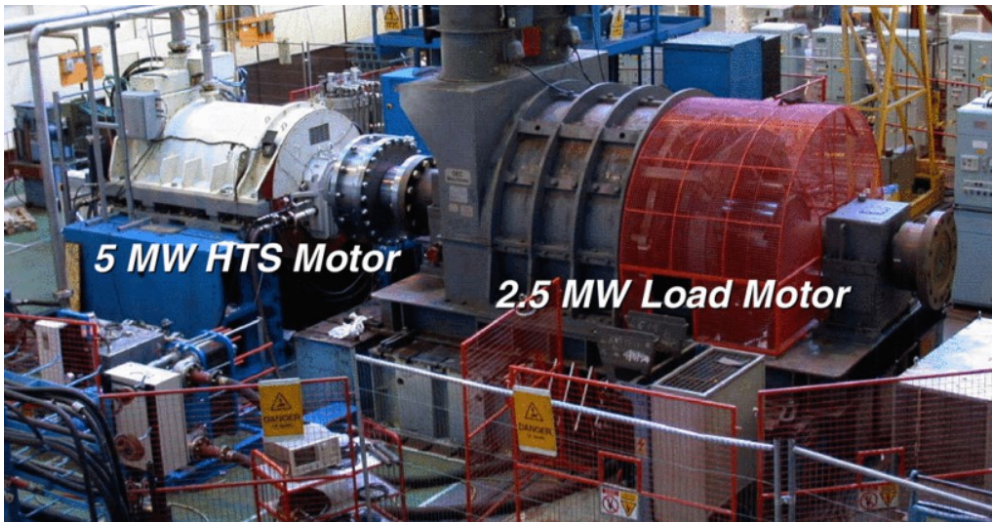


**Figure 21:** A HTS $5\ MW, 230 - rpm$ ship propulsion motor (on left) and a conventional $2.5\ MW$ motor (on right).[37]

In *"A Comparison of Cryogenic-Cooled and Superconducting Electrical Machines"*[3] the steady-state operation of air-cooled, cryogenic-cooled and superconducting induction machines are compared, showing a considerable increase of torque and efficiency performances in the last

two respect that in the conventional, but also a peculiar mechanical characteristic that is typical of this type of motors:

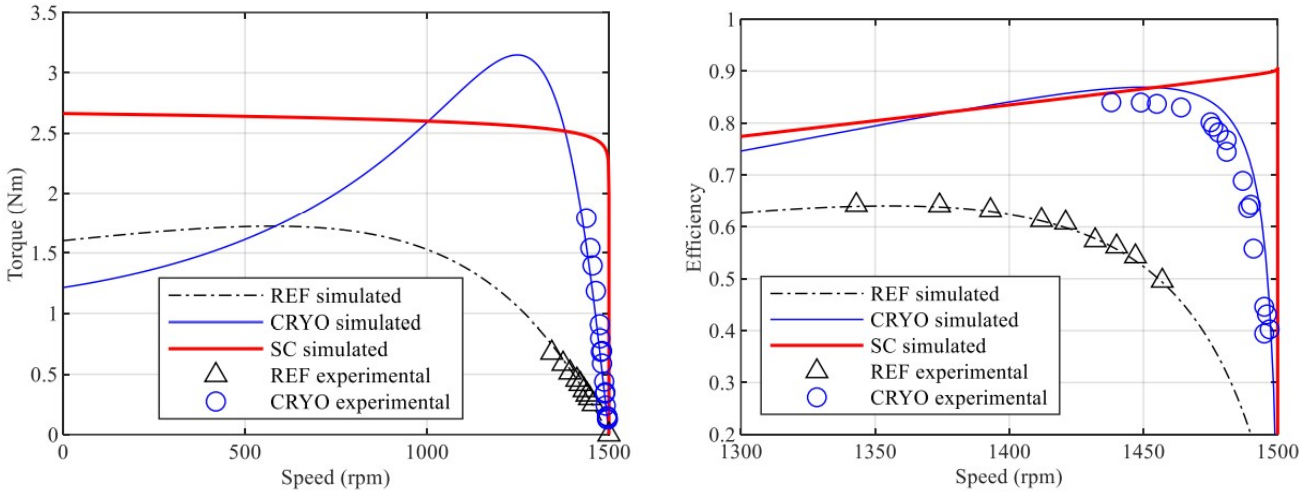


(a) (b)

**Figure 22:** The performance characteristics of the 90 W air-cooled (REF), cryogenic-cooled (CRYO) and superconducting (SC) machine concepts. (a) Torque vs. speed, and (b) Efficiency vs. Speed.[3]

# 2 Approach and Motor Characteristics

## 2.1 Approach Used in the Thesis

The approach of this thesis relies on the realization of an accurate finite element model of the 15 kW squirrel-cage induction motor, created in COMSOL Multiphysics, and its validation by comparing it with actual test data. The aim is to create a reliable numerical model capable of replicating the motor operation at both ambient and cryogenic temperatures.
After implementing the first key-factors in Comsol (geometry, materials, mesh, winding etc.), the model accuracy is improved by including significant electromagnetic phenomena such as skin effect in rotor bars, end-rings and end-windings resistances and inductances. The model is initially verified under normal operating conditions using the traditional tests (no-load, locked-rotor, and load test) performed on the real motor in accordance with IEEE Std 112-1991[20]. These tests allow for the calibration of key parameters such as air-gap length and rotor bridge thickness.
Once the finite element model appears to be a faithful reflection of the real motor, cryogenic conditions are simulated by scaling the electrical conductivity of the materials to low-temperature levels (in this case $-196°C$ for liquid nitrogen environments). The motor torque-speed characteristic is then established by applying a series of constant load torques and measuring the resulting steady-state rotor speed.
This combined numerical–experimental approach ensures an accurate representation of real motor performance and allows a direct comparison between normal and cryogenic operation, showing the advantages that low-temperature applications can provide.

## 2.2 Starting Point: 15 kW Induction Motor

The starting point is an available asynchronous machine with nominal power of $15kW$. This will be the machine subject of the thesis experiment. Its main data, its geometrical data as well as the features of the stator windings are reported respectively in Tab.1, Tab.2 and Tab.3. The stator is double layer 3-phase with parallel teeth, and the rotor is a conventional squirrel cage rotor with aluminum bars. Finally, the iron is M400-50A.

| | |
|---|---|
| Nominam Power | 15 kW |
| Nominal Voltage | 400 V |
| Nominal Current | 30 A |
| Frequency | 50 Hz |
| Connection Type | Delta |

**Table 1:** Nominal Data

| | |
|---|---|
| Stator External Diameter | 260 mm |
| Stator Internal Diameter | 162 mm |
| Axial Length | 200 mm |
| Number of Stator Slots | 48 |
| Airgap Length | 0.4 mm |
| Internal Rotor Diameter | 60 mm |
| Number of Rotor Slots | 40 |

**Table 2:** Manufacturing Geometrical Data

| | |
|---|---|
| Number of Phases | 3 |
| Number of Poles | 4 |
| Slots per pole per phase | 4 |
| Shortening | 2 |
| Conductors in series per phase | 256 |

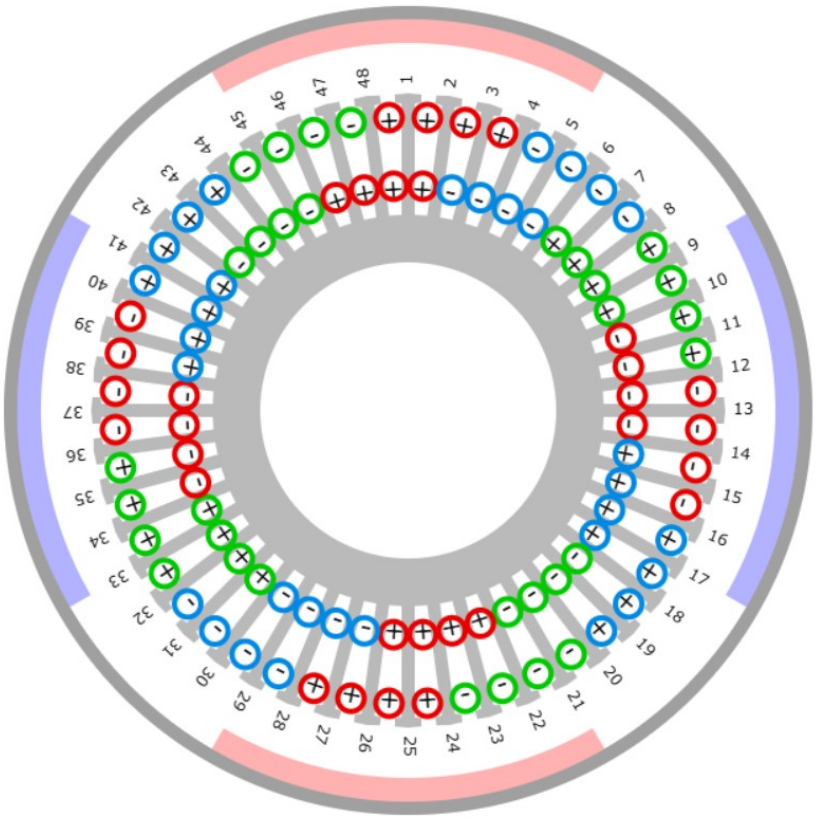

**Table 3:** Windings of the Motor

# 3 Implementation in COMSOL Multiphysics

## 3.1 Principles of COMSOL Operation

Comsol Multiphysics is a Finite Element Method which uses subdivision of a whole problem domain into simpler parts called finite elements to solve the problem by minimizing an associated error function. The *RMM, Rotating Machinery, Magnetic* in Comsol solves the Maxwell equations considering also the material properties to compute the distribution of the electromagnetic field. Once the electromagnetic fields are determined, it is possible to evaluate important characteristics of the machine, such as its torque. In time-dependent analysis, a magneto quasi-static approximation, which is suitable for the solutions of low-frequency problems in electromagnetics [30], is used.

In this interface, there are two different formulations of Maxwell's equations: the *vector potential formulation* and the *scalar potential formulation*. In order to describe the first formulation, it is necessary to introduce the magnetic vector potential **A**:

$$\mathbf{E} = -\frac{\partial \mathbf{A}}{\partial t} \tag{1}$$

$$\mathbf{B} = \nabla \times \mathbf{A} \tag{2}$$

Of course, in these equations, **B** is the Magnetic Induction and **E** is the Electric Field. Once the magnetic vector potential is defined, the Faraday's Law and the magnetic Gauss's Law are introduced:

$$\nabla \times \mathbf{E} = -\frac{\partial \mathbf{B}}{\partial t} \tag{3}$$

$$\nabla \cdot \mathbf{B} = 0 \tag{4}$$

The Ampere's Law is solved:

$$\nabla \times \mathbf{H} = \mathbf{J} \tag{5}$$

where **J** is the Current Density.

This formulation is easy to implement, and allows to compute accurately all magnetic fields problems. By default, the *RMM* applies the vector potential formulation to all domains. Then the scalar potential formulation is applied to all current-free domains (air-gap, non-conductive domains...) overwriting Ampere's Law. In the scalar potential formulation, a scalar field $\phi$ (magnetic scalar potential) is introduced, and the magnetic field is expressed as the gradient

of this potential. This formulation, on the other side, is easy to implement and faster to solve respect to the previous one. However, it can only be used in absence of currents.

## 3.2 Preliminary Calculations: Skin Effect of Rotor Bars and Inclusion of 3D effects

### 3.2.1 Evaluation of Skin Effect

In order to carry out a comprehensive analysis of the machine's behavior under both ambient and cryogenic conditions, it is essential to consider the skin effect and its variation with temperature. The skin effect, which refers to the tendency of alternating current to flow near the surface of a conductor, leads to an effective reduction in the cross-sectional area available for current flow at higher frequencies, thus increasing the effective resistance. This phenomenon becomes particularly significant in materials with high electrical conductivity, and its impact varies with temperature: at cryogenic temperatures, where conductivity increases, the skin depth tends to decrease, potentially altering the distribution of current within the conductors. While the skin effect can generally be neglected for the stator windings, typically composed of litz wire or stranded conductors designed to mitigate such effects, it cannot be disregarded in the rotor bars, in this case made of aluminum. In these components, especially under cryogenic conditions, the skin effect may significantly influence both the electromagnetic behavior and the overall performance of the motor[13].
It is evaluated for each frequency value according to the methodology exposed in "*The Induction Machines Design Handbook*"[11] and *"Computational Algorithms for Induction Motor Equivalent Circuit Parameter Determination—Part II: Skin Effect and Magnetizing Characteristics*[7]. In relatively large engines, the rotor bars take on an irregular shape to exploit the beneficial effects of rotor cages, like in this case. Thus, the solution is obtained by dividing the slot in $n$ layers of height $h_t$ and width $b_j$ (Fig.23), and by solving the Faraday's equation for each layers iteratively. For the $p^{th}$ layer:

$$R_p \overline{I}_p - R_{p+1} \overline{I}_{p+1} = -jSw_1 \Delta \overline{\Phi}_p \tag{6}$$

where $R_p$ and $R_{p+1}$ represent the resistances of the layers $p$ and $p+1$:

$$R_p = \frac{1}{\sigma_{Al}} \frac{l_{stck}}{b_p \, h_t} \tag{7}$$

$$R_{p+1} = \frac{1}{\sigma_{Al}} \frac{l_{stck}}{b_{p+1}\ h_t} \tag{8}$$

and

$$\Delta\Phi_p = \frac{\mu_0\ l_{stck}\ h_t}{b_p} \sum_{j=1}^{p} I_j \tag{9}$$

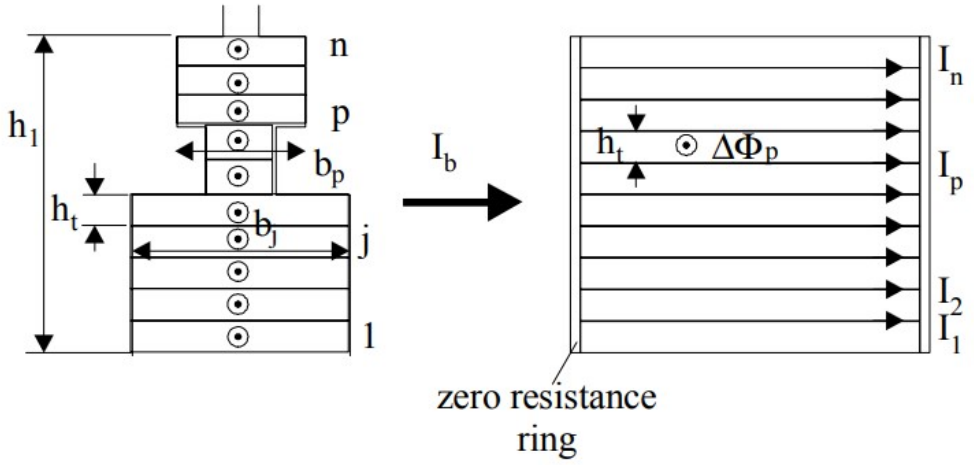


**Figure 23:** Division of a Bar of General Shape in $n$ layers [11].

Considering $L_p$ as the inductance of the $p^{th}$ layer, Eq6 becomes:

$$I_{p+1} = \frac{R_p}{R_{p+1}} I_p + j \frac{S w_1 L_p}{R_{p+1}} \sum_{j=1}^{p} I_j \tag{10}$$

with

$$L_p = \frac{\mu_0 \cdot l_{stack} \cdot h_t}{b_p} \tag{11}$$

The initial value of the current of the first layer is linked to the bar's current:

$$(\overline{I}_1)_{initial} = \frac{\overline{I}_b}{n} \tag{12}$$

where $I_b$ is the initial value of the current in the bar (chosen for simplicity equal to $1\ A$). Iteratively, it's possible to evaluate the currents of every layer leading to the calculation of $K_R$ and $K_L$:

$$K_r = \frac{P_{ac}}{P_{dc}} = \frac{\sum_{j=1}^{p} I_j^2 R_j}{\sum_{j=1}^{p} I_{jdc}^2 R_j} \tag{13}$$

$$K_L = \frac{\sum_{j=1}^{n} L_j \left| \sum_{k=1}^{j} I_k \right|^2}{\sum_{j=1}^{n} L_j \left| \sum_{k=1}^{j} I_{kdc} \right|^2} \tag{14}$$

In this particular case, the rotor bar has been divided into $n = 100$ layers, each with a height of $h = 27/100\ mm$ and a width of $b_j$:

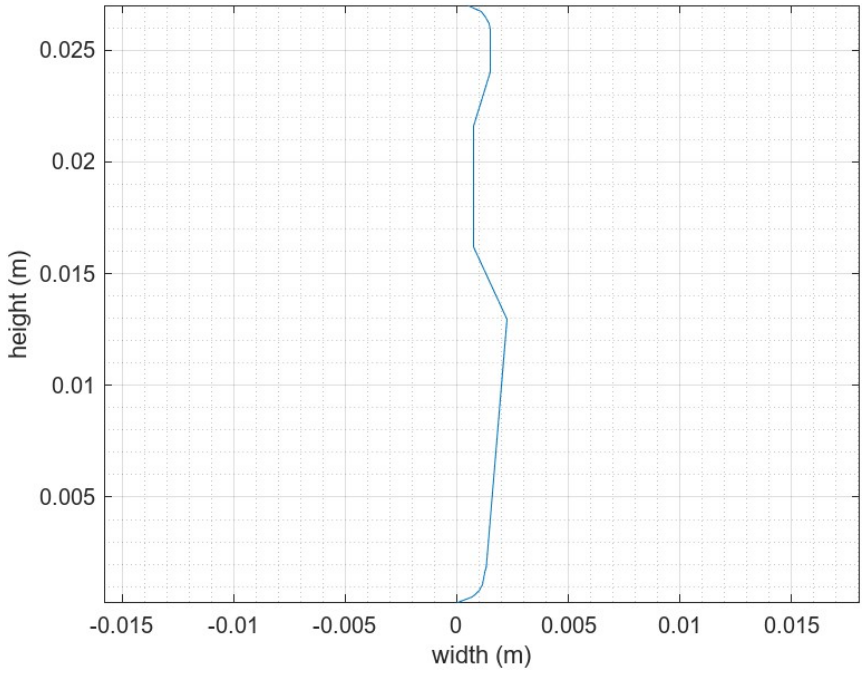


**Figure 24:** MatLab Script: Shape of Rotor Bar

At a temperature of about 80°C (the temperature at which the load tests were conducted), the obtained values are equal to:

$$K_R = 2.65;\ K_L = 0.65 \tag{15}$$

They are substantially different from those obtained under cryogenic conditions ($-196\ ^\circ C$):

$$K_R = 6.62;\ K_L = 0.19 \tag{16}$$

These results are qualitatively consistent with theoretical expectations[11]:

$$K_R = \xi\ \frac{(sinh\ 2\xi + sin\ 2\xi)}{(cosh\ 2\xi - cos\ 2\xi)} = \frac{R_{ac}}{R_{dc}}\ ;\ K_L = \frac{3}{2\xi}\frac{(sinh\ 2\xi - sin\ 2\xi)}{(cosh\ 2\xi - cos\ 2\xi)} = \frac{L_{ac}}{L_{dc}} \tag{17}$$

with

$$\xi = \beta h_s = \frac{h_s}{\delta}\ ;\ \beta = \frac{1}{\delta} = \sqrt{\frac{s\omega_1\mu_0\sigma_{Al}}{2}\frac{b_c}{b_s}} \tag{18}$$

Where $\sigma_{Al}$ is the aluminum conductivity.

As shown in Fig.25, both coefficients depend on the dimensionless parameter $\xi$, a dimensionless parameter that represents how much the current is "pushed" to the edges of the conductor.

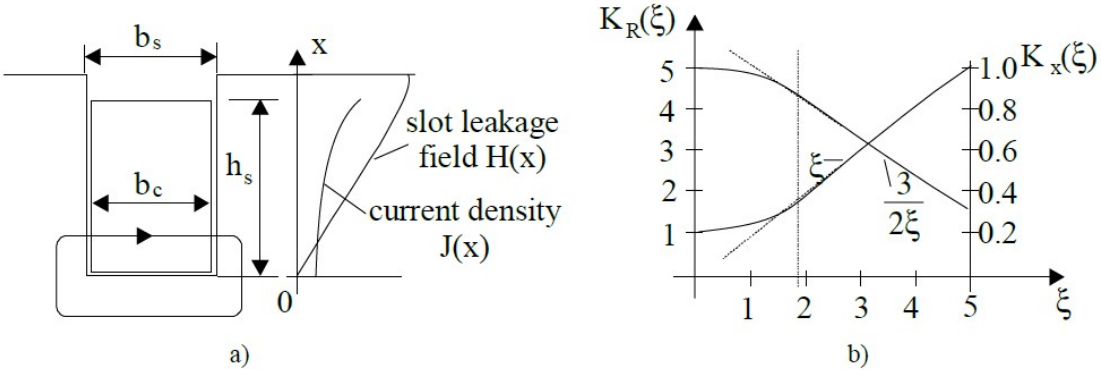


**Figure 25:** Rectangular Slot: a) slot field $H(x)$ and current density $J(x)$ distributions, b) resistance $K_R$ and slot leakage inductance $K_X$ skin effect correction factors.[11]

Since $\delta$ decreases at cryogenic temperatures due to lower electrical resistivity, $\xi$ will significantly increase. In particular, it will be: $\xi \propto \sqrt{\sigma_{Al}}$. As the conductivity of aluminum at 196 °C is about 11 times that at 83 °C, then $\xi$ under cryogenic conditions will increase by about 3-4 times than conventional conditions, resulting in a considerable increase in the skin coefficients.

### 3.2.2 Inclusion of 3D Effects of the Machine

In Comsol, a two-dimensional analysis is conduced, which results in reduced computation time and more straightforward interpretation of the field solutions. However, three-dimensional effects play a crucial role in accurately assessing the performance of a three-phase induction motor and must not be overlooked. These effects stem from the motor's finite axial length, specifically the stator end-windings, rotor end rings, and the skewing of rotor slots. They are particularly impactful on short and wide motors. In *"Calculation Methods and Effects of End-Winding Inductance and Permanent-Magnet End Flux on Performance Prediction of Nonoverlap Winding Permanent-Magnet Machines"*[31] are discussed several ways to take into account the leakage inductances of end-windings, but the same principle can be considered also for the other 3D effects. Generally, the most accurate way to take them into account is to implement a 3D geometry on Comsol, but it would require an incredible computational effort. To face it, it's also possible to include equivalent parameters external to the FEM simulation as shown in Fig.26 [2]:

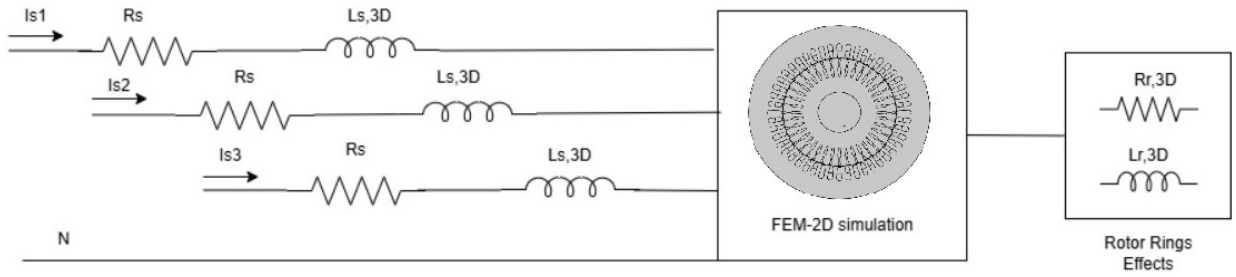


**Figure 26:** External Equivalent Circuit

In this case, for example, $R_s$ and $L_{s,3D}$ represent respectively the phase resistances and leakage inductances of the stator end-windings. $R_{r,3D}$ and $L_{r,3D}$, instead, modelize the resistance and the leakage inductance of the rotor rings (in case of a squirrel-cage induction motor) [2].
In the specific case of this thesis, the external circuit is introduced to take into account the leakage inductances related to stator end-windings, rotor rings and skewing effect. The end-windings and the rotor-ring resistances, on the other hand, are taken into account by means of two coefficients (respectively $k_{cu}$ and $k_{al}$) which are multiplied by the respective resistivities of the active parts of the machine:

$$R_{act} \cdot k_{cu} = R_{act} + R_{ew} \tag{19}$$

$$R_{bars} \cdot k_{al} = R_{bars} + R_{rings} \tag{20}$$

Where $R_{act}$ is the resistance of the active part of the stator windings, $R_{ew}$ is the end-windings resistance, $R_{bars}$ and $R_{rings}$ are respectively the resistance of rotor bars and rotor rings.
The calculation of $k_{cu}$ is presented in *"Computational Algorithms for Induction-Motor Equivalent Circuit Parameter Determination—Part I: Resistances and Leakage Reactances"*[9]: the average turn length is the contribution of two elements: $L_{core} = 0.2\ m$ is the axial length of the active wires, and $L_{ew}$ is the length of end-windings (Fig.27):

$$L_{ave,turn} = 2 \cdot (L_{core} + L_{ew}) = 2 \cdot (0.2 + 0.181) = 0.762\ m \tag{21}$$

$$L_{ew} = k_{ew}\tau_w = \frac{1.7}{2} \cdot 0.1063 = 0.181\ m \tag{22}$$

$$\tau_w = \left(1 - \frac{n_r N_{pole}}{N_{ss}}\right) \frac{\pi}{N_{pole}}(D_{is} + h_s) = \left(1 - \frac{2 \cdot 4}{48}\right) \frac{\pi}{4}(0.162 + 0.0004) = 0.1063\ m \tag{23}$$

where $k_{ew} = 1.7$, $N_{ss} = 48$ is the number of stator slots, $N_{pole} = 4$ is the number of poles, $n_r = 2$ is the pitch shortening, $D_{is} = 0.162\ m$ is the inner diameter of the stator, $h_s = 0.0004\ m$ is the air-gap length.

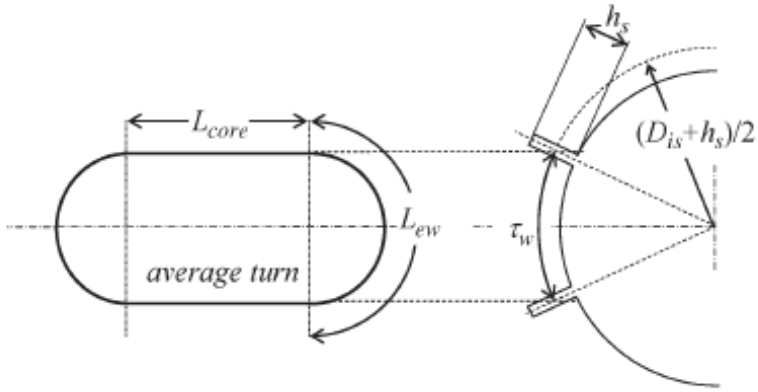


**Figure 27:** Determination of Winding Length

To calculate $k_{al}$, the resistances of bars and rings have to be calculated [9], considering that, in the locked rotor test, it must be taken into account the impact of skin effect (Section3.2.1) on the bars which has an important influence on the motor's performances (for simplicity, it is neglected in the rings). In addition, the temperature at which the locked rotor test was conducted is $75°C$. Thus, the resistance of a bar will be:

$$R_b(75\ °C) = K_r \cdot \rho \frac{l_{bar}}{S_{bar}} = 2.65 \cdot 3.42 \cdot 10^{-8} \cdot \frac{0.2}{75.68 \cdot 10^{-6}} = 2.4 \cdot 10^{-4}\ \Omega \tag{24}$$

where $\rho = 3.42 \cdot 10^{-8}\ \Omega m$ is the aluminum resistivity at $75\ °C$, $l_{bar} = 0.2\ m$ is the rotor bar length, $S_{bar} = 75.69\ mm^2$ is the bar section, $K_r = 2.65$ is the skin effect of the bar at 50 Hz calculated previously (Section3.2.1) [8]. The resistance of the ring, on the other side, is:

$$R_a = \rho \frac{\pi D_a}{S_a} = 3.42 \cdot 10^{-8} \cdot \frac{\pi \cdot 132.6 \cdot 10^{-3}}{302.76 \cdot 10^{-6}} = 4.71 \cdot 10^{-5}\ \Omega \tag{25}$$

where $S_a$ is the ring section and $D_a$ is the ring average diameter:

$$S_a = S_{bar} \frac{1}{2sen\left(\frac{2\pi p}{N_{bars}} \frac{1}{2}\right)} = 302.76\ mm^2 \tag{26}$$

$$D_a = D_{est,rot} - 2 \cdot (h_{bridges} + h_{bar}/2) = 132.6\ mm \tag{27}$$

where $N_{bars} = 40$ is the number of rotor bars, $p = 2$ is number of pole-pairs, $D_{est,rot} = 161.2\ mm$ is the external diameter of rotor, $h_{bar} \approx 27\ mm$ is the height of bars and $h_{bridges} = 0.8\ mm$ is the length of rotor bridges.

Considering each rotor bar as a phase of a multiphase winding, assuming $\beta_r = \frac{360°}{N_{bars}} = 9°$

as the mechanical angle between two consecutive rotor bars, the equivalent rotor-phase resistance will be:

$$R_r = R_b + \frac{2\ R_a}{4\ N_{bars}\ sin^2(p\ \beta_r/2)} = (2.4 + 0.241) \cdot 10^{-4}\ \Omega \tag{28}$$

Where the first contribution is due to the rotor bars (with skin effect), and second due to cage rings (neglecting skin effect). Hence, $k_{al}$ will be:

$$k_{al} = \frac{(2.4 + 0.241)}{2.4} \frac{10^{-4}}{10^{-4}} = 1.1 \tag{29}$$

Once the resistances of the end-windings and of rotor-rings have been calculated, and the way in which these parameters are inserted into the simulation has been explained, it is also appropriate to calculate their leakage inductances so that they can be inserted into Comsol via an external circuit.

As mentioned above, an external circuit is used to include the leakage inductances of stator end-windings, rotor rings and skewing effect. With regard to the latter effect mentioned, considering an inclination of the rotor bar equal to 1.1 times the stator pitch, it is obtained [9] (Fig.28):

- $\delta_i = 8.25°$
- $\gamma_i = 1.06°$
- $\tau_i = 3.69\ mm$

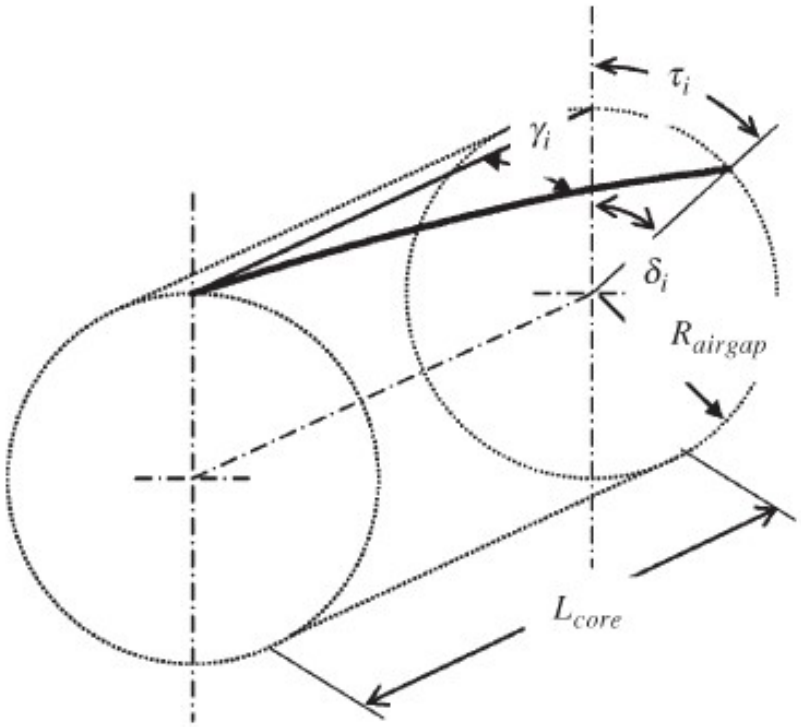


**Figure 28:** Geometrical Effect of Skewing

Thus:

$$\chi_i = sin\left(\frac{N_{pole} \cdot \delta_i}{4}\right) / \left(\frac{N_{pole} \cdot \delta_i}{4}\right) = 0.99654 \tag{30}$$

The values of leakage inductances due to skewing relative to stator and rotor, can be calculated with the following formulas:

$$L_{leak-skew,st} = (1-\chi_i) \cdot L_{m1,s} = (1-\chi_i)\,\frac{3}{2}\left(\frac{Z_{ph}\ k_{w,1}}{\pi\ N_{pole}/2}\right)^2 \frac{\mu_0\ \pi\ R_{airgap}\ L_{slot}}{K_{C,ave,sr}\ h_{airgap}} \tag{31}$$

$$L_{leak-skew,rot} = (1-\chi_i) \cdot L_{m1,r} = (1-\chi_i)\,\frac{N_{bars}}{2\pi^2}\frac{\mu_0\ \pi\ R_{airgap}\ L_{slot}}{K_{c,ave,sr}\ h_{airgap}} \tag{32}$$

Obtaining:

$$L_{leak-skew,st} = 9.7614 \cdot 10^{-4}\ H \tag{33}$$

$$L_{leak-skew,rot} = 9.27 \cdot 10^{-7}\ H \tag{34}$$

$$L_{leak-skew} = L_{leak-skew,st} + L_{leak-skew,rot} = 9.771 \cdot 10^{-4}\ H \tag{35}$$

In addition, rotor rings and stator end-windings leakage inductances are respectively calculated according to the analytical models presented below. This model allows to calculate the leakage inductance of a ring portion relative to an equivalent rotor phase:

$$L_{ei} = \mu_0\ L_i\ \lambda_{ei} \tag{36}$$

Where $L_i$ (Eq37; end-ring segment length) and $\lambda_{ei}$ (Eq38; geometrical permeance) are respectively calculated as:

$$L_i = \frac{\pi D_{ir}}{N_r} \tag{37}$$

$$\lambda_{ei} \approx \frac{2\ 3D_{ir}}{4N_r L_{stck} sin^2\left(\frac{\pi p}{N_r}\right)} log\left(4.7\frac{D_{ir}}{2(a+b)}\right) \tag{38}$$

In Eq38, $D_{ir} \approx 0.132$ is the average diameter of the rings. Moreover, $a$ and $b$ are the end-rings dimensions, assumed to be equal respectively to $0.02\ mm$ and $0.035\ mm$ (Fig.29):

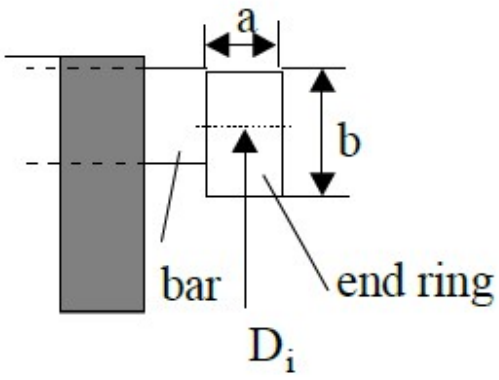


**Figure 29:** End-Rings Dimensions

Thus, multiplying $L_{ei}$ by the number of equivalent rotor phases, equal to the number of bars, and then by two (i.e. the number of rings) the leakage inductance of the rotor rings which, finally, can be reported to stator is obtained.

For the stator end-windings leakage inductances, the following expression is used[9]:

$$L_{ph,ew} = \frac{\mu_0\ Z_{ph}^2}{2\pi\ 2N_{poles}} log\left(\frac{L_h}{p_h}\right)\frac{4}{3}L_h \tag{39}$$

Where $L_h = 0.181\ m$ is the end-winding length and $p_h = 0.015\ m$ is the half-perimeter of the end-winding cross section.

Downstream of this, the phase inductances reported to the primary are:

$$L'_{ph,ew} = 4.28 \cdot 10^{-4}\ H \tag{40}$$

$$L'_{ph,rings} = 3.3 \cdot 10^{-4}\ H \tag{41}$$

### 3.2.3 Topology of External Circuit

The way in which these parameters are incorporated into the simulation is shown in Fig.30. *"RMM: COIL 1"*, *"RMM: COIL 2"* and *"RMM: COIL 3"* represent respectively the motor phases a, b and c simulated in the *"RMM: Rotating Machinery, Magnetic"* physics. Instead, $L_{ext}$ represents the sum of the leakage inductances calculated analytically previously and reported to the primary. Its value depends on the type of test that is carried out: in locked-rotor tests, $L_{ext}$ includes the end-winding leakage inductance, but also the end-rings and the skewing inductance as all parameters can be considered in series. However, in the no-load or load tests $L_{ext}$ is simply equal to the end-windings leakage inductance.

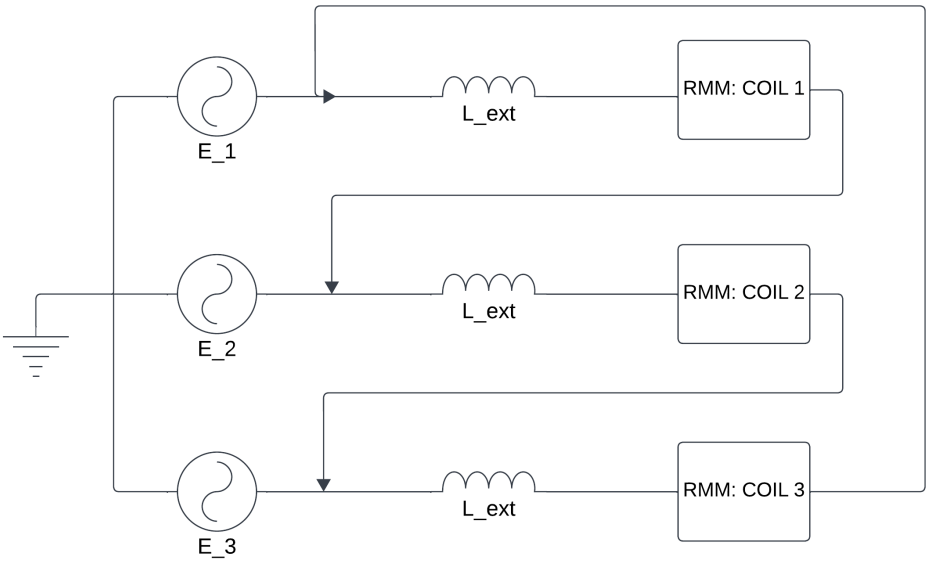


**Figure 30:** External Circuit Implemented in Comsol

As mentioned in Section2.2, the motor windings are delta connected. This means that the phase voltage corresponds to the line voltage, so the voltages $E_1$, $E_2$ and $E_3$ shown in the figure will be scaled by a factor $\sqrt{3}$ with respect to $V_{ph,1}$, $V_{ph,2}$ and $V_{ph,3}$ and will be $30°$ phase-shifted according to the phasor diagram shown below:

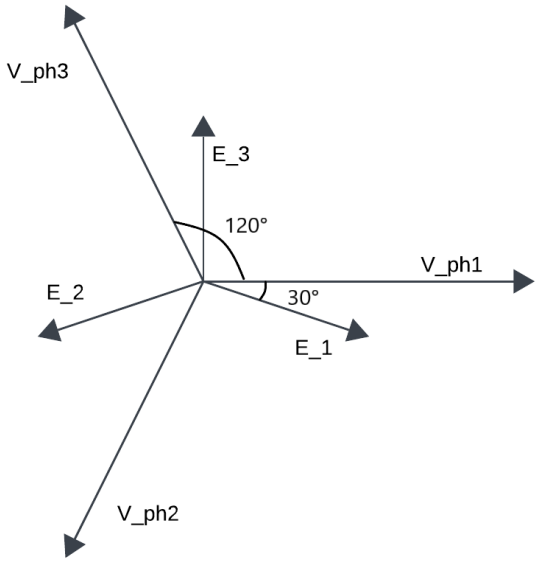


**Figure 31:** Phasor Diagram of Phase and Line Voltages

## 3.3 Geometry and Main Parameters

According to the data available in Tab.2, it's possible, first of all, to implement the geometry of the motor on COMSOL Multiphysics (Fig.32). This operation can be done either by building the geometry directly on Comsol through the union of several elementary geometric elements (arcs, segments...), or by importing the geometry directly from an external software. The first approach has been chosen. In this way, it is also possible to parametrize quantities so that the behavior of the machine, when these vary, can be studied. In this way, the length of the air-gap and the thickness of the rotor bridges have been calibrated to make the model faithful to the real motor (Section.4.2.1; Section4.3.1).

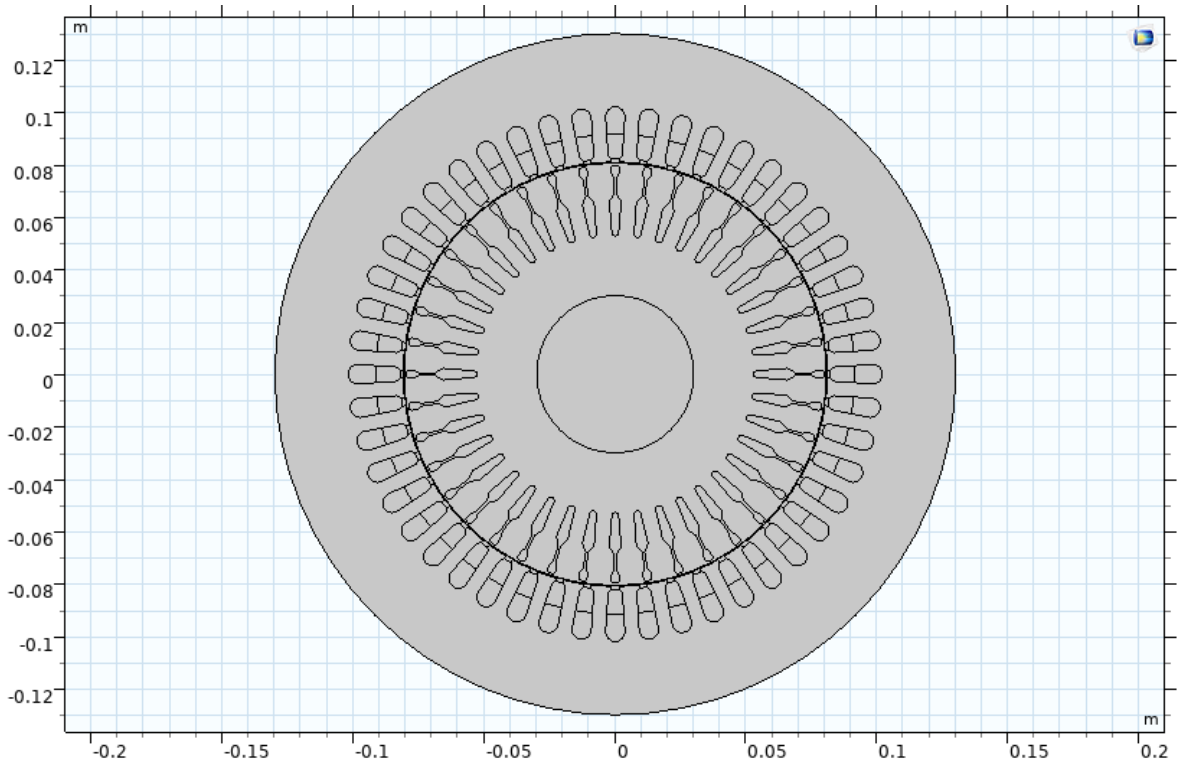


**Figure 32:** Geometry of the Motor.

At this point, the main parameters of the motor have been defined in the *"Parameters"* section of Comsol: test temperature, conductivity of copper and aluminum, fill factor, $k_{cu}$, $k_{al}$ and so on.

## 3.4 Materials

After defining geometry and main parameters, the next step to implement the motor in Comsol is to associate each domain with a material. According to the specifications of the motor, the core is made of non-oriented fully processed electrical steel M400-50A. It is possible to take the material directly from the Comsol library, and eventually it is possible to modify some of its characteristics. For example, one feature that could be modified is the BH curve of the iron. The saturation curve could be "calibrated" in such a way as to make the simulation closer to the real motor. The reason is due to a whole series of processes to which the iron is subjected during the assembly of the motor, altering its physical properties [26]. However, for the purposes of this thesis and due to the important time required for simulations, it was considered not essential to carry out such calibration, and the "original" saturation curve taken directly from Comsol was used.

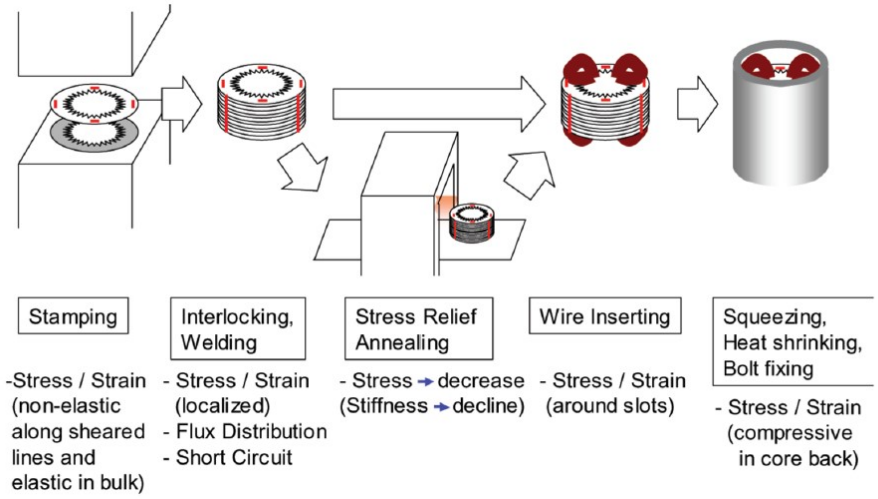


**Figure 33:** Iron Manifacturing Process [26].

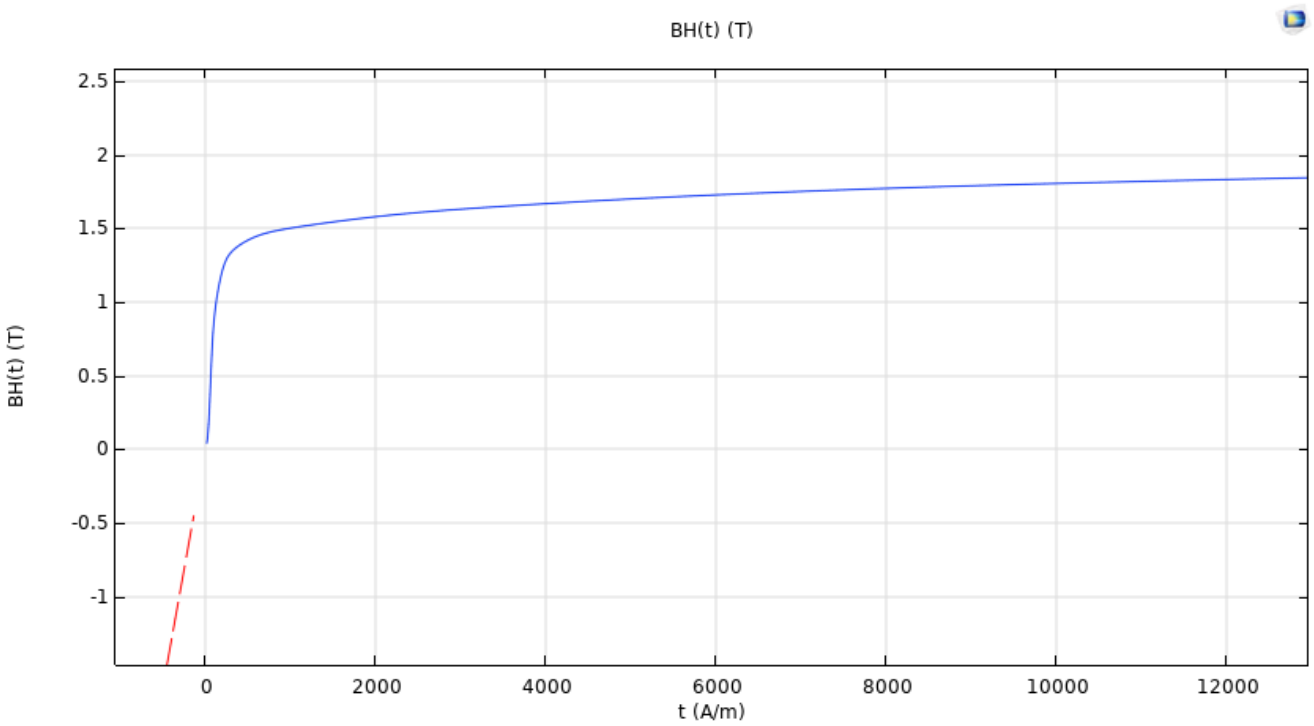


**Figure 34:** BH curve of M400-50A from Comsol's Library. On the "x-axis" the magnetic field [A/m], on the "y-axis" the magnetic induction [T]

For the rotor bars, on the other hand, the aluminum alloy 1100-0 was chosen. This was done by manually modifying the electrical conductivity of the aluminum once it was defined in the simulation parameters [14].
Regarding the stator slots, copper is simply chosen from the Comsol library as a material.

## 3.5 Coils Determination

Three voltage supplied *homogenized multi-turns*, one for each phase, are set as shown in Fig.35. Obviously, the voltages of the respective phases will be shifted by 120 electrical degrees. The number of conductors is also defined, as well as the copper conductivity and the active area of the copper. All these values have been defined in the *Parameters* section. For the $k_{fill}$, which is the filling coefficient, a value of 0.4 - typical for this type of machine - has been chosen.

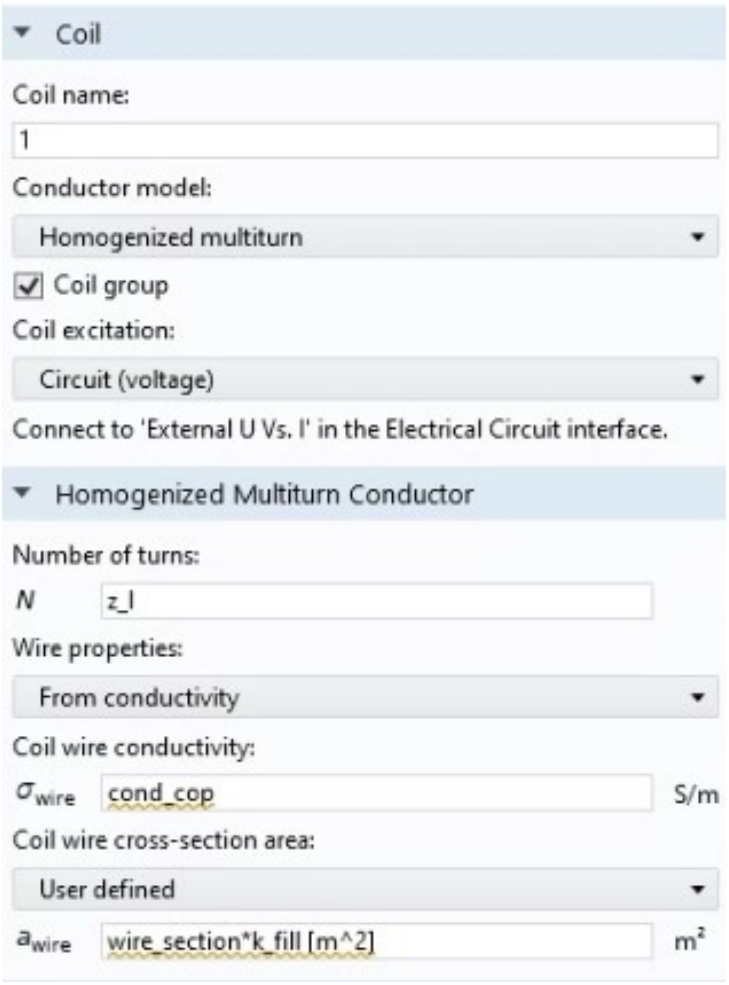


**Figure 35:** Layout of Coil's Settings

## 3.6 Mesh and Moving Mesh

At this point, the mesh must be modified properly. Choosing a mesh in FEM for the modeling of an electric motor is a very serious issue since its quality directly influences the accuracy and the computational efficiency of the simulation. Of course, a finer mesh allows for a very accurate evaluation of the physical phenomena, but carries a long computational effort. Vice

versa, a coarse mesh makes the simulation faster but approximates too much the real behavior. So, it's very important to reach a compromise between these two extreme conditions, in such a way to facilitate the simulation getting at the same time reliable results. Generally, in the FEM study of an electric motor, the mesh is very defined in correspondence of the air-gap and more coarse in the jokes. This is because the evaluation of the electromagnetic condition in correspondence of the air-gap is crucial to understand and evaluate properly the performances of the machine. Consequently, the mesh resembles like in Fig.36 :

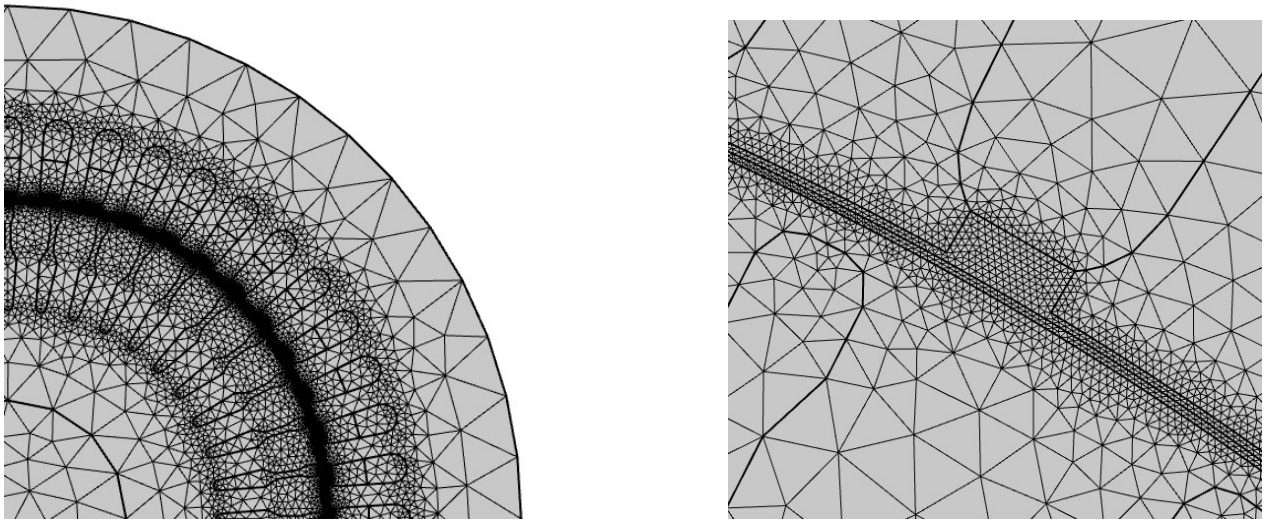

**(a)** Global Mesh **(b)** Air-Gap Mesh

**Figure 36:** Reassembly of Mesh used in Comsol.

The *Rotating Domain* feature within the *Moving Mesh* interface is used to simulate rotating parts of a geometry, such as the rotor in an electric machine. This approach allows the mesh in the rotating region to physically move or rotate over time while maintaining its shape, enabling accurate modeling of the relative motion between rotating and stationary parts. From the *Rotation type* list, it is possible to choose a type of rotation for the domain:

- **Specified rotational velocity** defines a rotational velocity expression for the moving domain. It can be constant or general revolution per time.
- **Rigid Body** specifies that the rotating domain behaves as if attached to a rigid body with the following parameters: Applied Momentum $M$ $[N \cdot m]$; Moment of Inertia $I$ $[kg \cdot m^2]$; Initial Angle $\alpha$ $[rad]$; Initial Angular Velocity $\omega_0$ $[rad/s]$.

The approach taken to carry out tests related to this thesis varies depending on the situation. To simulate a locked rotor test, for example, the rotor speed is simply set to zero. For the simulation of the no-load tests, instead, two approaches could be followed: on the one hand, the rotational speed of the rotor could be directly imposed synchronously with that of the rotating magnetic field. Alternatively, it would be possible to associate the rotor with inertia and refrain from applying any mechanical load. This last method is preferred since it allows a more natural evolution of the dynamics of the machine. Of course, the same method is also used to simulate load tests by changing the mechanical load applied.

# 4 Validation and Calibration of the Model

To validate the model implemented in Comsol, its values are compared with the ones got from the real tests. Time-dependent simulation have been launched on Comsol due to its working principle strictly related to the dependence of the electrical variables on time.
The tests performed on the machine were carried out in accordance with the guidelines set forth in IEEE Std 112-1991, titled *"IEEE Standard Test Procedure for Polyphase Induction Motors and Generators."*[20]. It is important to note that the mechanical losses, such as friction and windage ones, are neglected. These losses are typically captured during the no-load test as prescribed in the IEEE Std 112-1991, but are excluded from electromagnetic FEM simulations.

## 4.1 Analytical Calculation of the Stator Resistance

Before starting the analysis of the tests, it should be noted that the stator resistance is usually calculated from the DC test carried out on the machine. However, in this case, the stator resistance has been calculated analytically by following the approach presented in [9], considering a temperature of $25\ ^\circ C$:

$$R_s = \rho \frac{(Z_{ph}/2) \cdot L_{ave,turn}}{A_{wire}} = 1.756 \cdot 10^{-8} \cdot \frac{(256/2) \cdot 0.762}{3.08 \cdot 10^{-6}} = 0.556\ \Omega \tag{42}$$

where $A_{wire}$ is the section of the wire, $Z_{ph} = 256$ is the number of conductors in series per phase, $\rho = 1.756 \cdot 10^{-8}\ \Omega m$ is the copper resistivity at $25\ ^\circ C$, $L_{ave,turn}$ is the average turn length.

$$A_{wire} = k_{fill} \cdot \frac{S_{slot}}{N_c} = 0.4 \cdot \frac{123.2 \cdot 10^{-6}}{16} = 3.08 \cdot 10^{-6}\ m^2 \tag{43}$$

$k_{fill} = 0.4$ is the fill factor of the stator slots, $N_c = 16$ is the number of conductors per stator slot, $S_{slot} = 123.2\ mm^2$ is the surface of one stator slot. The average length of the stator turns has been calculated previously (Section3.2.2): $L_{ave,turn} = 2 \cdot (L_{stck} + L_{ew}) = 0.762\ m$.

## 4.2 No-Load Tests

The conventional No Load Test consists in the measurement of current and electric power absorbed by the machine when it is fed with a certain voltage and let it free to rotate without a mechanical load. In this condition, the speed is almost synchronous and the sink power is the sum of various contributions:

$$P_{sink} = P_{j,s} + P_{mech} + P_{iron} \tag{44}$$

which are, respectively, joule losses in the stator windings, mechanical losses due to friction and windage and iron losses. Its primary purpose is to determine the motor's core losses, friction and windage losses, and the magnetizing current required to establish the air-gap flux. As been said before, mechanical losses are neglected. The test temperature is considered to be equal to $T = 83\ ^{\circ}C$.

In the following table, the experimental data of the no-load test are shown, knowing that the mechanical losses are: $P_{mech} = 70.77\ W$.

**Table 4:** No Load Test: Experimental Data

| **Vph (V)** | **Iline (A)** | **Piron (W)** |
|---|---|---|
| 43.9 | 1.64 | 3.22 |
| 87.1 | 2.11 | 16.99 |
| 130.6 | 3.02 | 33.66 |
| 174.2 | 4.04 | 55.94 |
| 217.8 | 5.09 | 85.59 |
| 261.3 | 6.28 | 119.16 |
| 304.8 | 7.59 | 157.34 |
| 348.5 | 9.45 | 225.96 |
| 374.5 | 10.93 | 284.23 |
| 400.6 | 13.40 | 378.50 |

For all these voltage values, no-load simulations were carried out on Comsol. By imposing the voltage, it was possible to obtain the magnetizing current as output, as shown in the graph below:

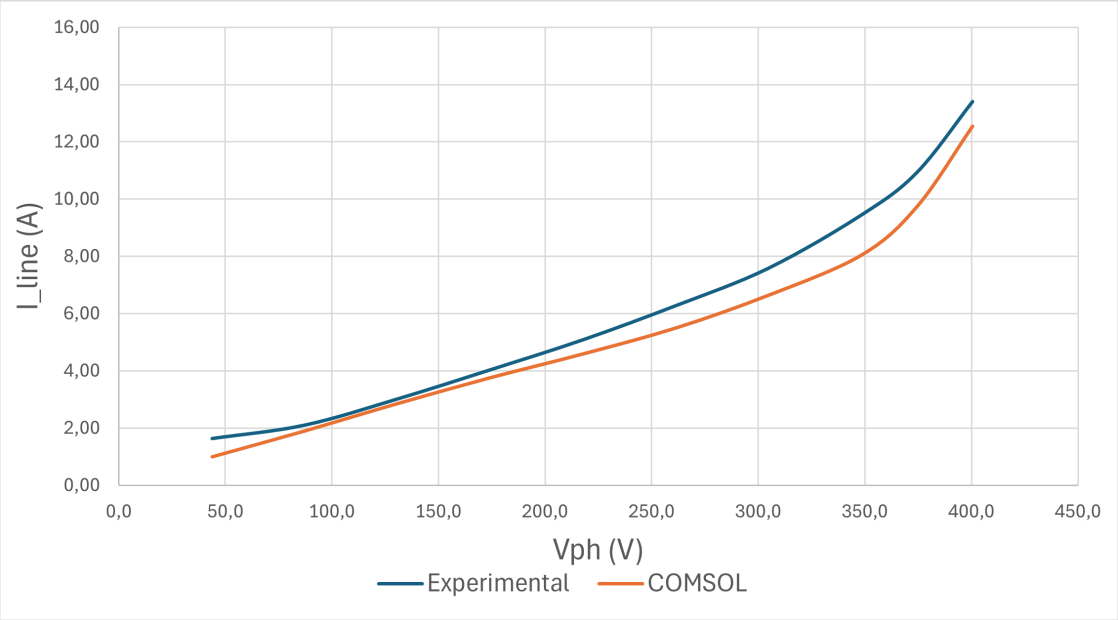


**Figure 37:** No-Load Test simulated in Comsol: Line Current $I_{line}$ $[A]$ as a Function of Phase (Line) Voltage $V_{ph}$ $[V]$

Although the general trend of the currents is roughly the same of the experimental one, they are still too low, reaching a maximum error of $1.4\ A$ ($\approx 15\%$) at $V_{ph} = 348.5\ V$. This discrepancy is due to an underestimation of the magnetizing current, which primarily depends on the magnetic reluctance of the air-gap. Thus, its calibration will be discussed in the following section.

### 4.2.1 Calibration of Air-Gap Thickness

To increase the magnetizing current, it is advisable to change the reluctance of the machine's magnetic circuit. Obviously, the section of magnetic circuit where the magnetomotive force fall is the highest, is in correspondence of the air-gap. Therefore, it will be necessary to calibrate this by a few mm for the characteristics to match properly.
As a first attempt, the thickness of the air-gap is increased from its nominal value of $0.4\ mm$ to the new value of $0.48\ mm$. The characteristic that follows is presented below:

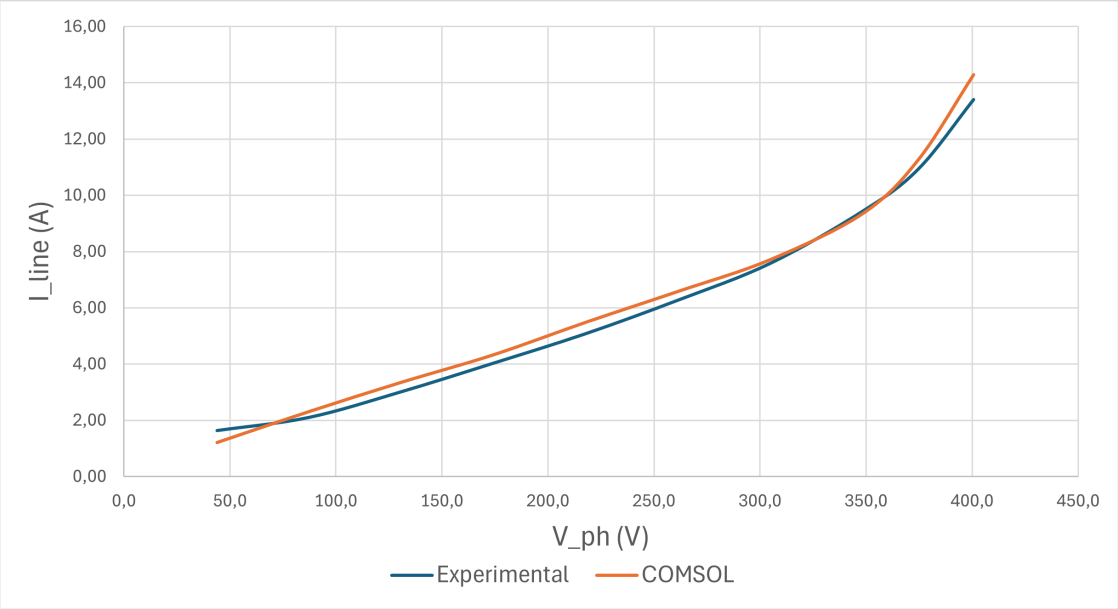


**Figure 38:** No Load Current-Voltage Characteristic: New Air-Gap Thickness of $0.48\ mm$

It is evident that the characteristics match more than before. The maximum error ($0.87\ A$ ; $6\%$), however, is at the nominal voltage (400 V), a value for which the transversal parameters of the equivalent circuit will be calculated later. It is therefore preferable to have a current value closer to the real value at this point. Therefore, the gap has been slightly reduced to $0.45\ mm$ presenting the following results:

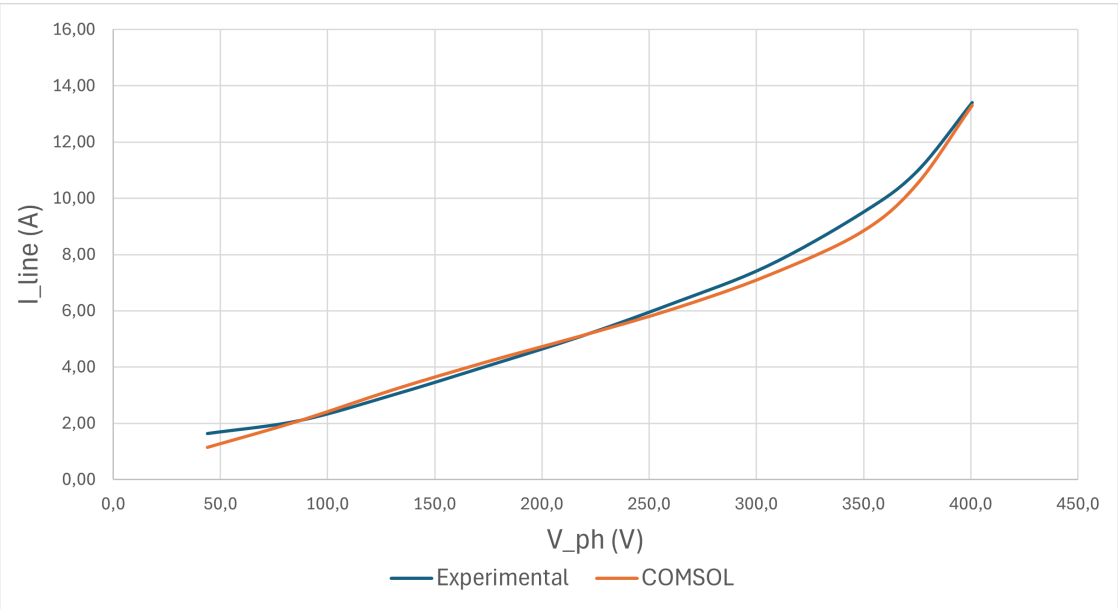


**Figure 39:** No Load Current-Voltage Characteristic: New Air-Gap Thickness of $0.45\ mm$

In this way, the curves are satisfactory. The almost perfect match of the linear zone of the

curves indicates that the reluctance of the magnetic circuit, and therefore the thickness of the air-gap, is calibrated correctly. For what concerns the knee of the curve, it is due to iron saturation. In order to match this feature perfectly, it would be advisable to carry out a further calibration of the B-H curve of the iron with which the machine is built. However, for the purposes of this thesis, such a study would be laborious and unnecessary. It is decided, therefore, to keep as the final thickness of the air-gap $0.45\ mm$.

## 4.3 Locked-Rotor Test

For this test, the rotor is locked and a 3-phase voltage is applied to the stator to generate a rotating magnetic field. This test is carried out at a temperature of $75\ °C$. According to the IEEE Std 112-1991[20], the machine must be powered with reduced voltage values to avoid short-circuit currents that would damage it.
The experimental data are shown subsequently:

**Table 5:** Locked-Rotor Test: Experimental Data

| **Vph (V)** | **Iline (A)** | **P (W)** | **Cosfi** |
|---|---|---|---|
| 35.28 | 12.24 | 335.76 | 0.449 |
| 52.73 | 20.90 | 946.81 | 0.496 |
| 73.72 | 31.52 | 2117.06 | 0.526 |
| 92.8 | 41.34 | 3589.42 | 0.540 |

As already done, the locked rotor motor is also simulated in Comsol by applying the voltage values in Tab.5 and imposing null rotor speed. What follows is the graph:

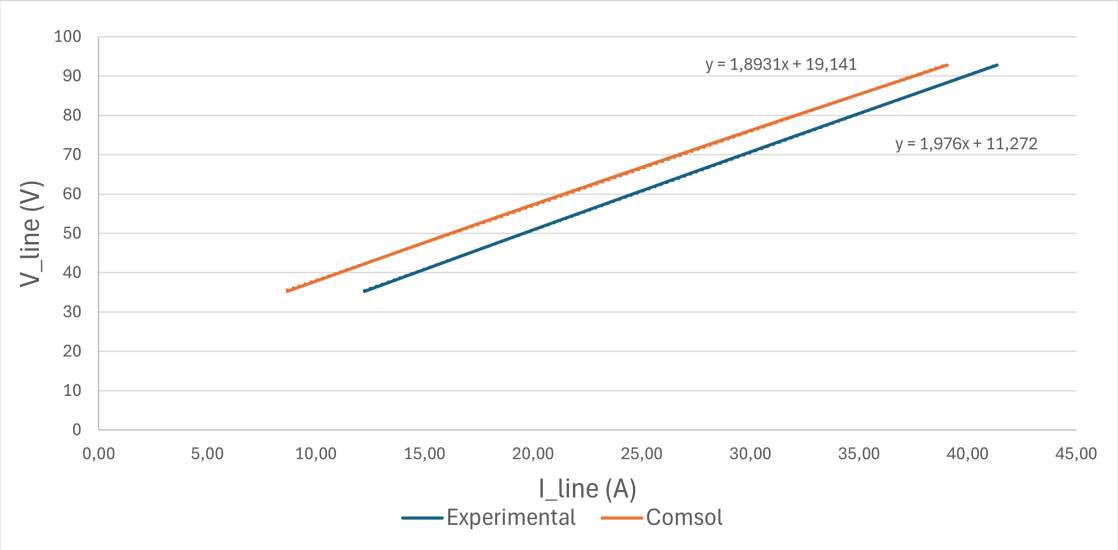


**Figure 40:** Locked Rotor Test simulated in Comsol: Phase (Line) Voltage Vline [V] as a Function of Line Current Iline [A]

The trend of the current appears to be consistent with the values obtained experimentally. However, the curve appears to be shifted. This is probably due to the saturation of the rotor bridges, which must be properly calibrated.

In "*Modelling of the closed rotor slot effects in the induction motor equivalent circuit*"[10], it is discussed how an induction motor with closed rotor slots is modeled. During motor operation, the narrow bridges that enclose the rotor slots become magnetically saturated at relatively low rotor current levels, effectively altering the motor's electromagnetic characteristics. The authors propose an enhanced single-phase equivalent circuit that includes an additional voltage source $V_0$ to represent the global saturation effect of these bridges. This voltage source is placed in series with the rotor impedance and models the resulting voltage drop due to magnetic saturation.

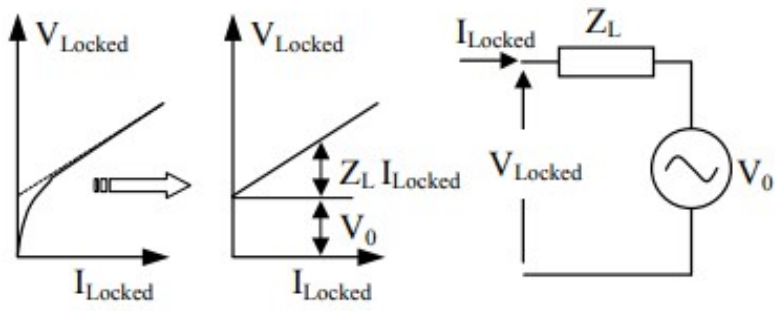


**Figure 41:** Voltage-Current characteristic during the locked rotor test for IM with closed rotor slots (ZL is the equivalent phase impedance in locked rotor condition)[10].

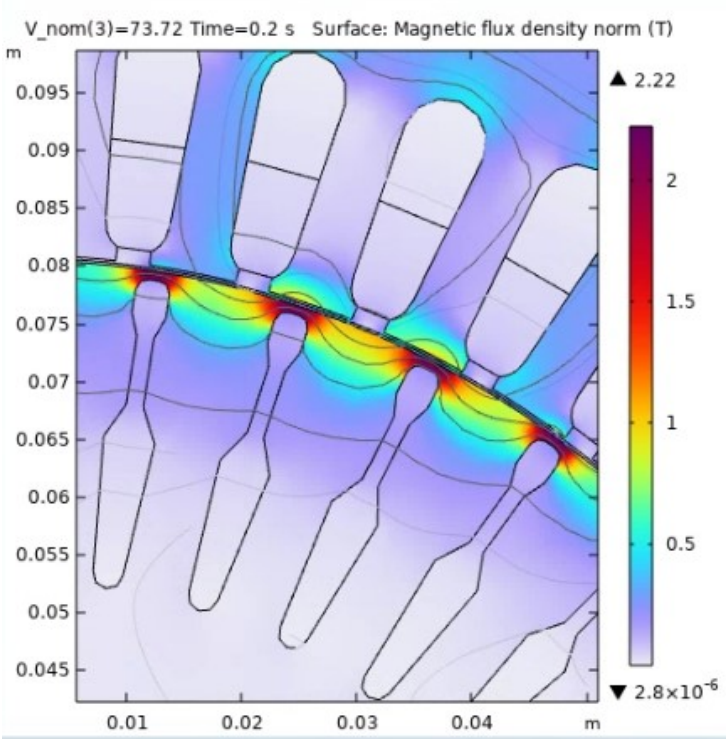


**Figure 42:** Magnetic Flux Density Norm [T] during Locked-Rotor Test: Saturation of Rotor Bridges

In the equivalent circuit the V0 voltage vector will be phase shifted of 90° respect to the current one because it manages reactive power.

### 4.3.1 Calibration of the Thickness of Rotor Bridges

As a first modification, their thickness has been reduced to $0.4\ mm$, leading to the following characteristic:

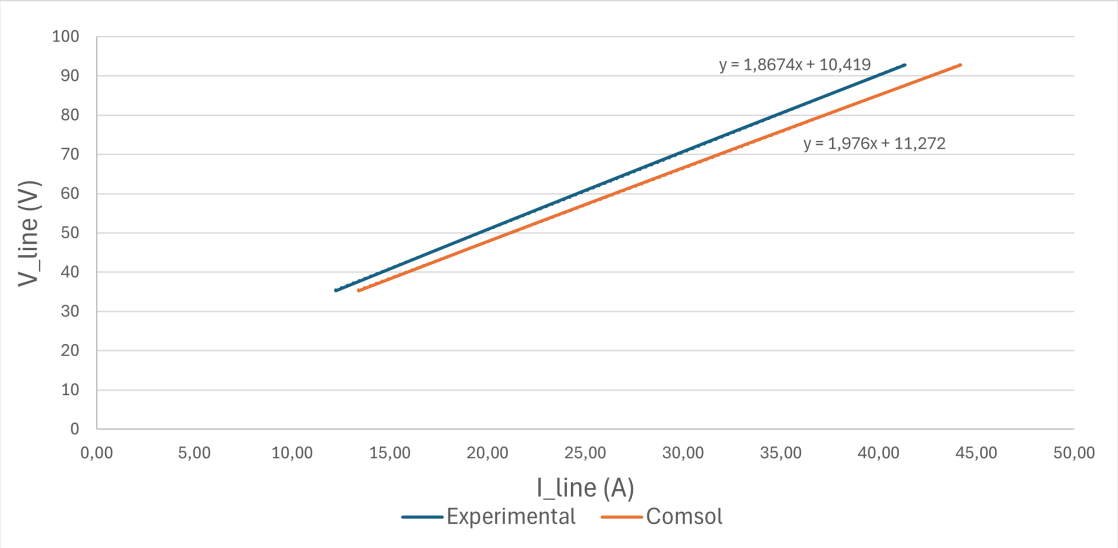


**Figure 43:** Locked-Rotor Voltage-Current Characteristic: New Rotor Bridges Thickness of 0.4 mm

As expected, the curve has undergone a substantial shift. However, the currents are now far too high in relation to the desired values. Therefore, a middle path is chosen and the thickness of the bridges is imposed equal to $0.6\ mm$:

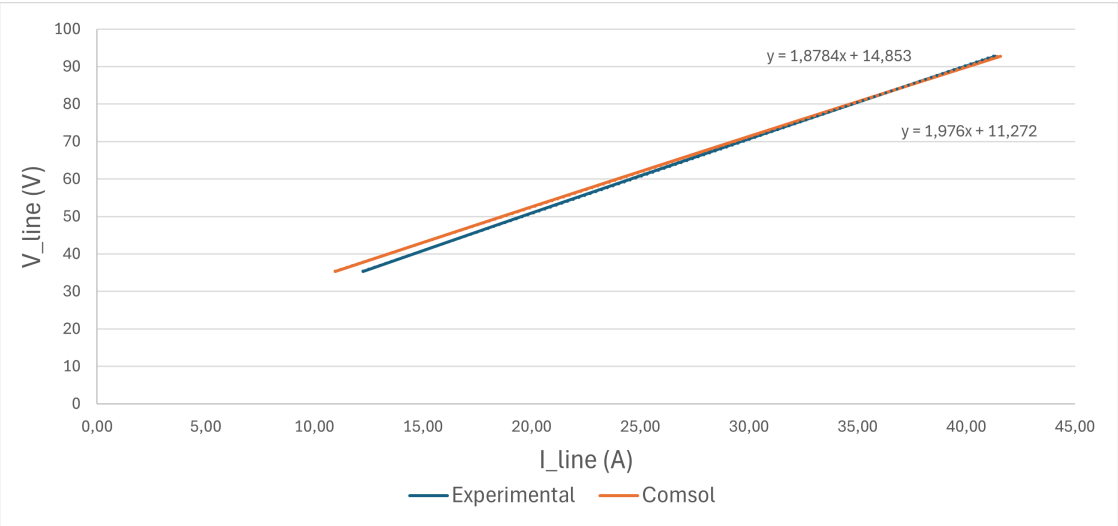


**Figure 44:** Locked-Rotor Voltage-Current Characteristic: New Rotor Bridges Thickness of 0.6 mm

## 4.4 Load Tests

To complete the experimental characterization of the induction motor and validate the accuracy of the finite element model under realistic operating conditions, a series of load tests were performed. These tests were conducted in accordance with the procedures outlined in IEEE Std 112-1991, which provide standardized methods for determining motor performance under mechanical load.

Load testing is essential for assessing the actual performance of the motor and verifying that the numerical model accurately reproduces the machine's behavior not only under ideal conditions (such as no-load), but also during energy conversion and torque production. The results obtained in this phase provide critical insight into the validity and practical applicability of the simulation-based design process.

The available data from experimental measurements are as follows:

**Table 6:** Load Tests: Experimental Data

| **RPM** | **Torque [Nm]** |
|---|---|
| 8.5 | 1497 |
| 34.8 | 1488 |
| 60.2 | 1479 |
| 84.5 | 1470 |
| 122.2 | 1455 |
| 156.4 | 1440 |

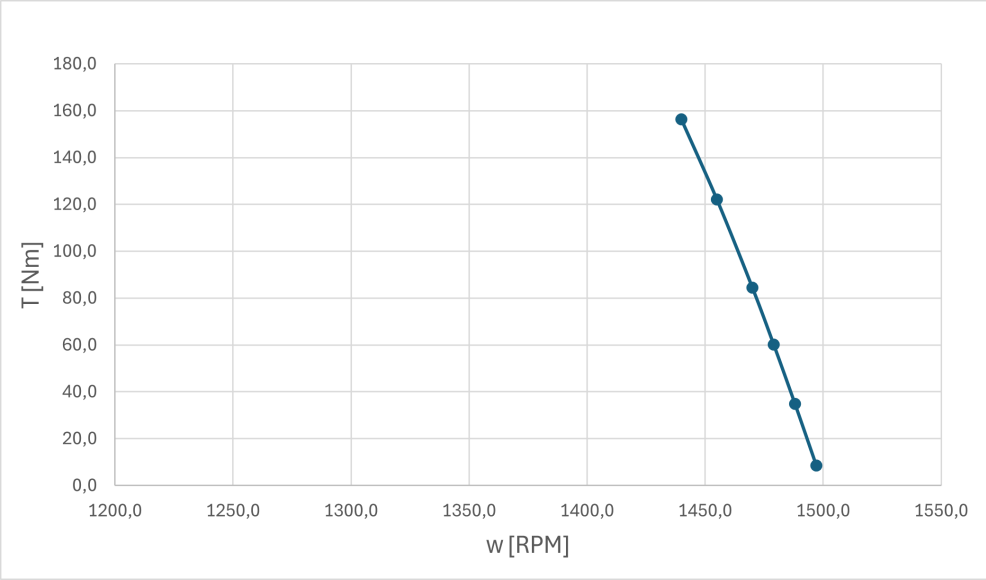


**Figure 45:** Stable Part of the Mechanical Characteristic, Experimental Values

The same characteristic has been obtained by simulations by parametrically varying the resistant torque as input, and obtaining the rotor speed in the dynamic equilibrium condition as output:

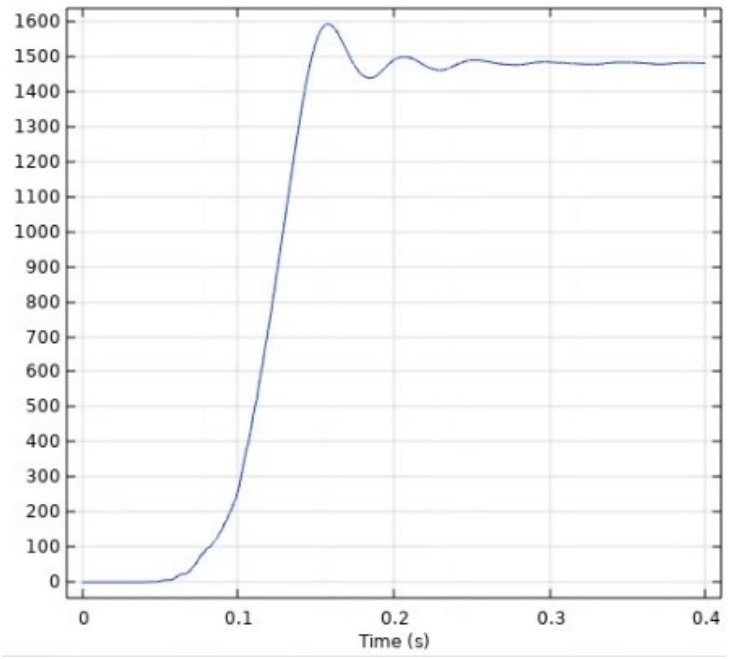


**Figure 46:** Evolution of Rotor Speed (RPM) as a function of Time (s) for an imposed load torque of $84.5\ Nm$.

This type of simulation was performed by varying the input load torque so as to have the same

experimental values. The results, compared with the experimental ones, are shown below:

**Table 7:** Load Test: Comparison between Experimental Data and Comsol Outputs

| Imposed Torque [Nm] | Experimental Speed [RPM] | Comsol Speed [RPM] |
|---|---|---|
| 8.5 | 1497 | 1498.5 |
| 34.8 | 1488 | 1492.1 |
| 84.5 | 1470 | 1479.6 |
| 122.2 | 1455 | 1470.2 |
| 156.4 | 1444 | 1460.9 |

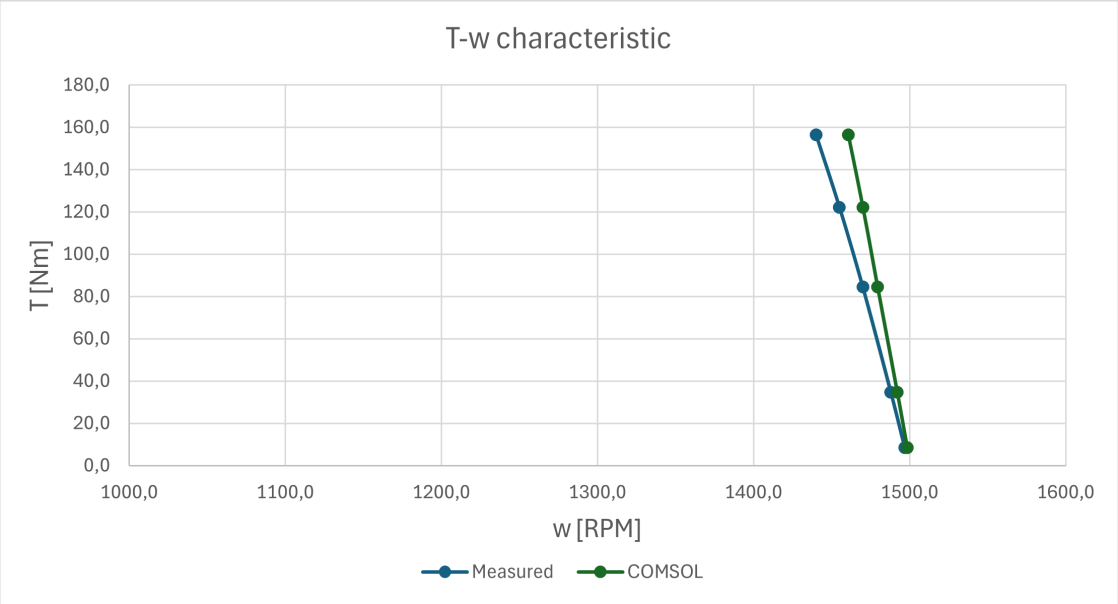


**Figure 47:** Stable Part of the Mechanical Characteristic: Comparison between Comsol Output and Experimental Results

Although the general pattern of the two curves is the same, in correspondence with the maximum value of torque applied ($156.4\ Nm$) the maximum error is reached, equal to $20.9\ RPM$ ($1.45\%$). As is well known from the theory of electric machines, the relation of the mechanical characteristic which links the torque "$T\ [Nm]$" with the slip "$s$" for $s \to 0$ is:

$$T|_{s\to 0} = 3 \cdot \frac{p}{\omega} \cdot \frac{\frac{R'_R}{s}}{\left(\frac{R'_R}{s}\right)^2 + (X_{eq} + X'_{lr})^2} \cdot V_{eq}^2 \approx 3 \cdot \frac{p}{\omega} \cdot \frac{V_{eq}^2}{R'_R} \cdot s \tag{45}$$

Where $p$ is the pole pairs, $\omega$ $[rad/s]$ is the electrical frequency, $R'_R$ $[\Omega]$ is the rotor resistance referred to the primary, $X_{eq}$ $[\Omega]$ is the equivalent Thevenin reactance, $X'_{dr}$ $[\Omega]$ is the rotor leakage reactance referred to the primary, $V_{eq}$ $[V]$ is the equivalent Thevenin voltage ($V_{eq} \propto V_{ph}$).

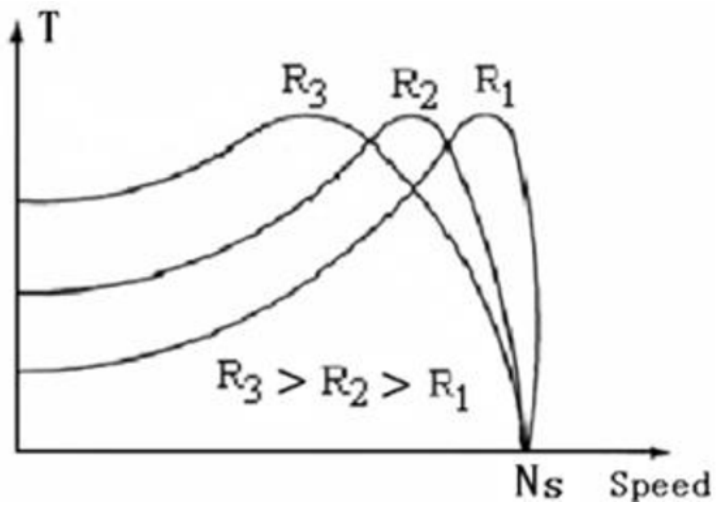


**Figure 48:** Torque-Speed Curves for Rotor Resistance Variation [29]

Thus, applying the same voltage and the same torque, the slip increases if the rotor resistance is also increased and vice versa. To have a mechanical characteristic faithful to the real one, the rotor resistance is appropriately calibrated by varying the resistance of the rotor rings ($k_{al}$).

### 4.4.1 Calibration of End-Rings Resistivity

By varying the value of $k_{al}$, it is concluded that for $k_{al} = 1.7$ the torque characteristics match almost perfectly, leading to the following values:

**Table 8:** Load Test Results: New End-Ring Resistivity

| Imposed Torque [Nm] | Experimental Speed [RPM] | Comsol Speed [RPM] |
|---|---|---|
| 8.5 | 1497 | 1496.7 |
| 34.8 | 1488 | 1487.4 |
| 84.5 | 1470 | 1469.8 |
| 122.2 | 1455 | 1454.8 |
| 156.4 | 1440 | 1439.6 |

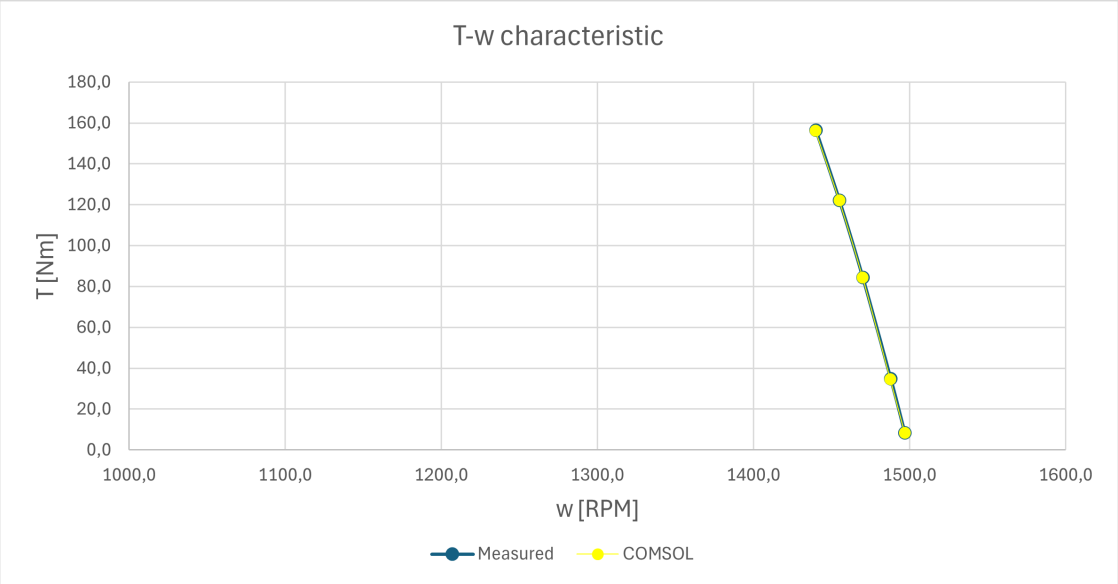


**Figure 49:** Stable Part of the Mechanical Characteristic: comparison between Experimantal Values and Comsol Outputs ($k_{al} = 1.7$)

Obviously, changing the rotor resistance value will also affect the voltage-current characteristic of the locked rotor test. By increasing the longitudinal impedance, the currents will tend to be lower than the desired value. Therefore, to decrease the impedance, the inductance relative to the skewing effect has been omitted. The final model has more than satisfactory characteristics in no-load tests, load tests and locked rotor tests (shown below):

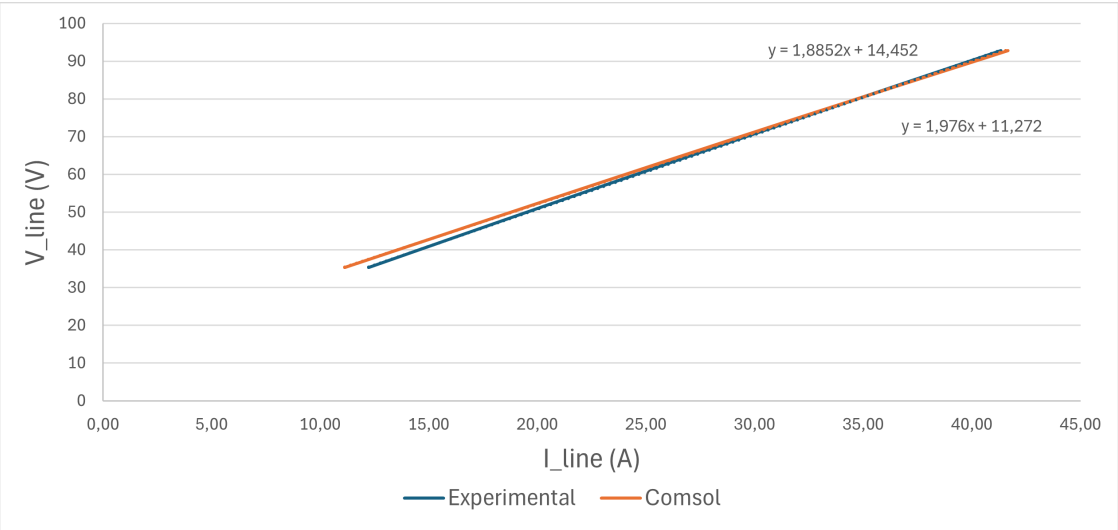


**Figure 50:** Locked-Rotor Characteristic with the Final Model

## 4.5 Determination of the Equivalent Circuit

To further validate the Comsol model, the equivalent motor circuit parameters are calculated from experimental tests and Comsol results following the instructions expressed in the IEEE Std 112-199[20]. The equivalent phase circuit of a general induction motor with closed rotor slots is shown in Fig.51.

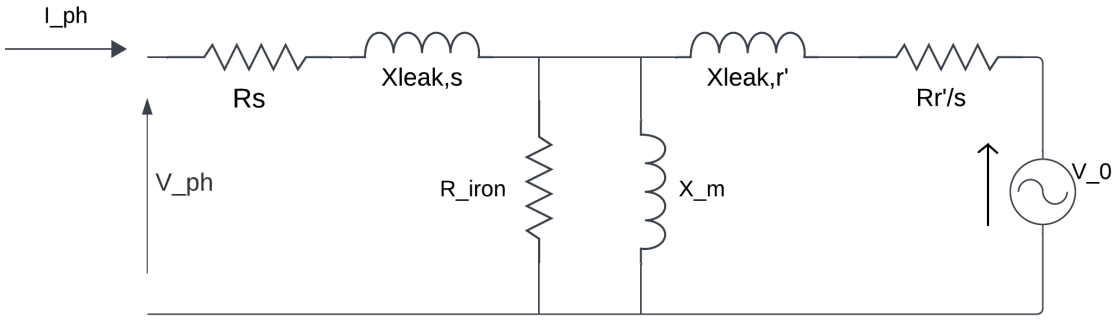


**Figure 51:** Equivalent Circuit of an Induction Motor

Where:

- $R_s$ is the stator phase resistance;
- $X_{ls}$ is the phase leakage reactance of the stator;
- $X_m$ is the phase magnetizing reactance;
- $X'_{lr}$ is the phase leakage reactance of the rotor referred to the stator;
- $R'_r$ is the phase rotor resistance referred to the stator;
- $s$ is the slip, defined as: $s = \frac{\omega_e - p\,\omega_m}{\omega_e}$ ($\omega_e$: electrical frequency; $\omega_m$: mechanical rotor speed; $p$: pole-pairs).
- $V_0$ is the reactive voltage source due to the geometry of rotor bars[10].

It is important to note that the iron resistance related to the iron losses is absent in the FEM model. Its effect are, in fact, calculated a posteriori with a dedicated study.

## 4.6 Calculation of Longitudinal Parameters from Locked-Rotor Test

It is possible, from the locked-rotor test results, to calculate the longitudinal parameters and the reactive voltage source.

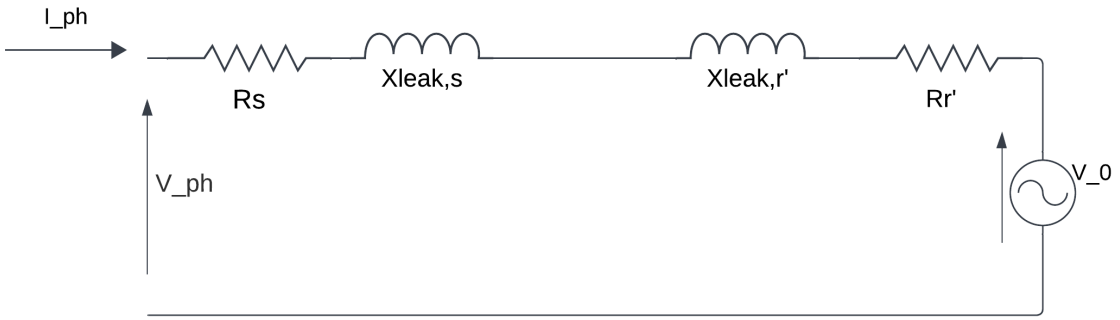


**Figure 52:** Locked Rotor IM Equivalent Circuit

The operating temperature during this test is $75\ °C$. The stator resistance, hence, will be:

$$R_s(75\ °C) = R_s(25\ °C)(1 + 0.00393 \cdot (75 - 25)) = 0.665\ \Omega \tag{46}$$

Where $0.00393$ is the temperature coefficient of copper at $25\ °C$.
Hereafter is shown the procedure to calculate the parameters in correspondence at $73\ V$, for the current is equal to $31\ A$, very close to the nominal value ($30\ A$):

- the total short-circuit resistance is calculated as:

$$R_{sct} = R_s + R'_r = \frac{P_{j,tot}}{I^2_{line}} \tag{47}$$

  Where $P_{j,tot}$ is the total Joule power of stator and rotor and $I_{line}$ is the line current equal to $\sqrt{3}$ time the phase current.

- by subtracting the stator resistance from this value, it is possible to estimate the rotor resistance at $75\ °C$:

$$Rr'(75\ °C) = R_{sct}(75\ °C) - R_s(75\ °C) \tag{48}$$

- the total leakage inductance is calculated as:

$$X_{l,tot} = X_{ls} + X'_{lr} = R_{sct}(75\ °C) \cdot tan(arccos(cos\phi(75\ °C))) \tag{49}$$

- the total leakage reactance is equally divided into stator and rotor contributions:

$$X_{ls} = X'_{lr} = \frac{1}{2} \cdot X_{l,tot} \tag{50}$$

In the same way, the parameters were calculated from both experimental and Comsol values. The only difference is in the calculation of stator resistance: whereas previously it was calculated analytically (Section4.1), Comsol allows to evaluate the Joule power dissipated in the stator windings. Thus it will be: $R_s = P_{J,stat}/I^2_{line}$.
Referring to what is stated in the paper "*Modelling of the closed rotor slot effects in the induction motor equivalent circuit*"[10], from the intercept with the y-axis of the locked rotor characteristic it is possible to determine the module of $V_0$ (Fig.41).

Finally, referring the resistances to 25°C according to the "IEEE Standard Test Procedure for Poly-phase Induction Motors and Generators" [20], the parameters will be:

**Table 9:** Comparison of Longitudinal Parameters from Locked-Rotor Test (T=25°C, f=50 Hz)

| **Parameter** | **Experimental** | **Comsol** | |
|---|---|---|---|
| Rs | 0.56 | 0.56 | Ω |
| Rr' | 1.20 | 1.08 | Ω |
| Xls=Xlr' | 1.72 | 1.79 | Ω |
| V0 | 11.3 | 14.5 | V |

## 4.7 Calculation of Transversal Parameters from No-Load Test

From the No-Load results, the magnetizing inductance can be extrapolated. Considering a temperature of $83\ °C$, the stator resistance will be:

$$R_s(83\ °C) = R_s(25\ °C)(1 + 0.00393 \cdot (83 - 25)) = 0.68\ \Omega \tag{51}$$

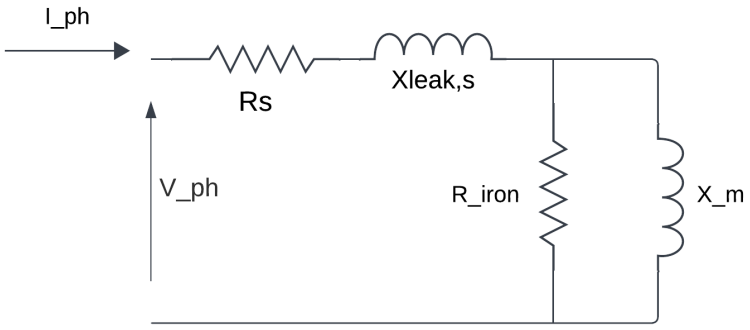


**Figure 53:** No-Load IM Equivalent Circuit

Considering the same mechanical losses measured experimentally, the magnetization reactance is calculated in correspondence of the nominal voltage as it follows::

- the Joule power in the stator is calculated:

$$P_{J,stat} = R_s^2 \, I_{line} \, (W) \tag{52}$$

- $P_0$, $Q_0$ and $S_0$ are the total active, reactive and apparent powers during no-load test:

$$P_0 = P_{J,stat} + P_{iron} + P_{mech} \, (W) \tag{53}$$

$$S_0 = \sqrt{3} \, V_{line} \, I_{line} \, (VA) \tag{54}$$

$$Q_0 = \sqrt{S_0^2 - P_0^2} \, (VAR) \tag{55}$$

- from the leakage reactance calculated previously, it is possible to evaluate the leakage reactive power in the stator:

$$Q_{leak,stat} = X_{l,s} \, I_{line}^2 \tag{56}$$

- by subtracting the contribution due to leakage fields from the total reactive power, it is possible to get the magnetizing reactive power $Q_m$, and, consequently, the apparent power absorbed by the transversal parameters $S_{tr}$

$$Q_m = Q_0 - Q_{leak,stat} \tag{57}$$

$$S_{tr} = \sqrt{P_{iron}^2 + Q_m^2} \tag{58}$$

- finally, the emf on transversal parameters is:

$$E_{s,0} = \frac{S_{tr}}{\sqrt{3} \cdot I_{line}} \tag{59}$$

- it is possible, now, to calculate the iron resistance $R_{iron}$ (at $83\ ^\circ C$) and the magnetizing reactance $X_m$:

$$R_{iron}(83\ ^\circ C) = \frac{3\ E_{s,0}^2}{P_{iron}} \tag{60}$$

$$X_m = \frac{3\ E_{s,0}^2}{Q_m} \tag{61}$$

In this case too, as for the locked rotor test, this procedure was used on both experimental and simulation data.

In Comsol, iron loss calculation with the RMM (Rotating Machinery, Magnetic) interface involves using the "*rmm.Qh*" variable, which represents the volumetric loss density, electromagnetic, in W/m³. This calculation relies on the magnetic flux density and frequency. Comsol provides built-in features to compute iron losses using models like the Steinmetz equation (used in this case) or Bertotti formulation.

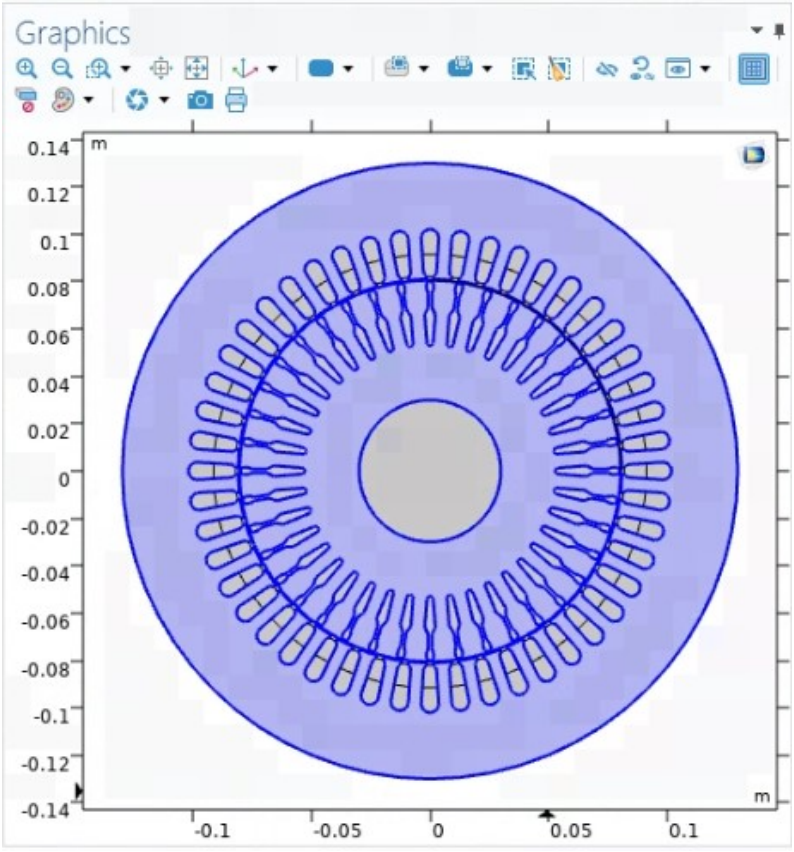


**Figure 54:** Comsol Interface: Selection of the Iron Domain to Evaluate Iron Losses

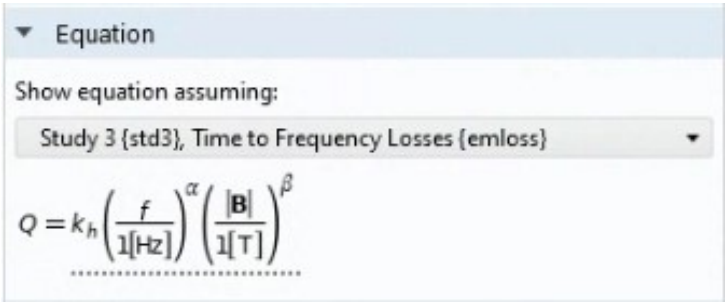


**Figure 55:** Steinmez Equation in Comsol

In the Steinmez Equation, shown in Fig.55, $f$ is the frequency, **B** [T] is the magnetic flux density and $k_h$, $\alpha$ and $\beta$ are coefficients. They are chosen as $\alpha = 1$ and $\beta = 2$. From the manufacturing data of the iron material, M400-50A, it is possible to evaluate the coefficient $k_h$. It is done by interpolating the core loss curve at 50Hz and by evaluating its coefficient (Fig.56):

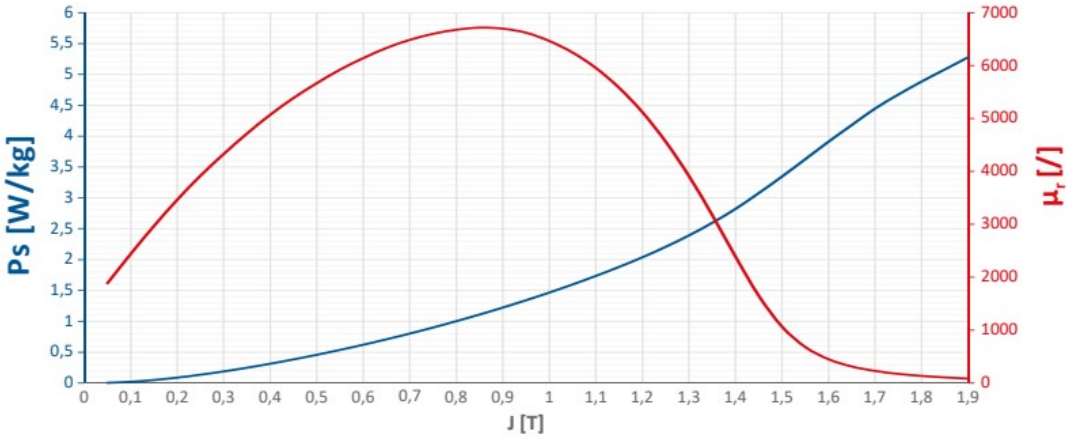


**Figure 56:** Typical Values of Core Loss Curve (blue) of M400-50A at 50 Hz

Due to the manufacturing processes of the laminated core, this curve undergoes changes. It is therefore opportune to calibrate the value of the coefficient $k_h$ to obtain the corrected values of iron losses. With a final value of $k_h = 418.32$, multiplying the power density [W/kg] by the core mass, the iron losses are obtained.

Finally, it is possible to calculate the transversal parameters referring the iron resistance to 25°C:

$$R_{iron}(25\ ^\circ C) = R_{iron}(83\ ^\circ C)/(1 + 0.004 \cdot (83 - 25)) \tag{62}$$

Where 0.004 is the typical electrical temperature coefficient of core at 25°C.

**Table 10:** Comparison of Transversal Parameters from No-Load Test (T=25°C, f=50 Hz)

| Parameter | Experimental | Comsol | |
|---|---|---|---|
| Xm | 50.07 | 50.3 | Ω |
| Riron | 963.34 | 966.1 | Ω |

## 4.8 Final Model

Downstream of the entire calibration process described in this section, the main features of the final Comsol model are summarized below:

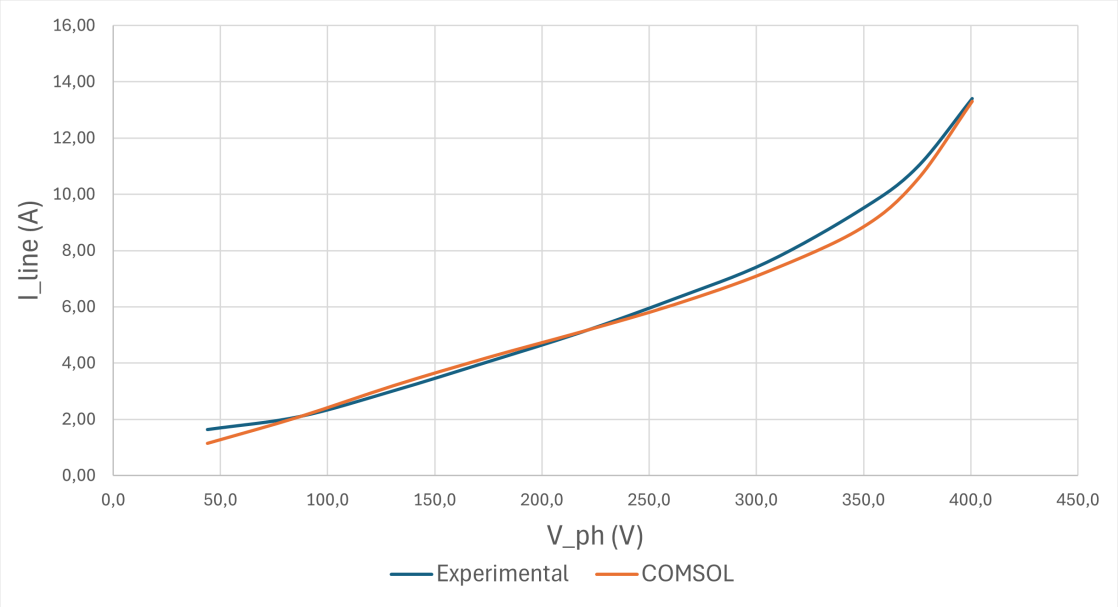


**Figure 57:** No-Load Characteristic: Final Model

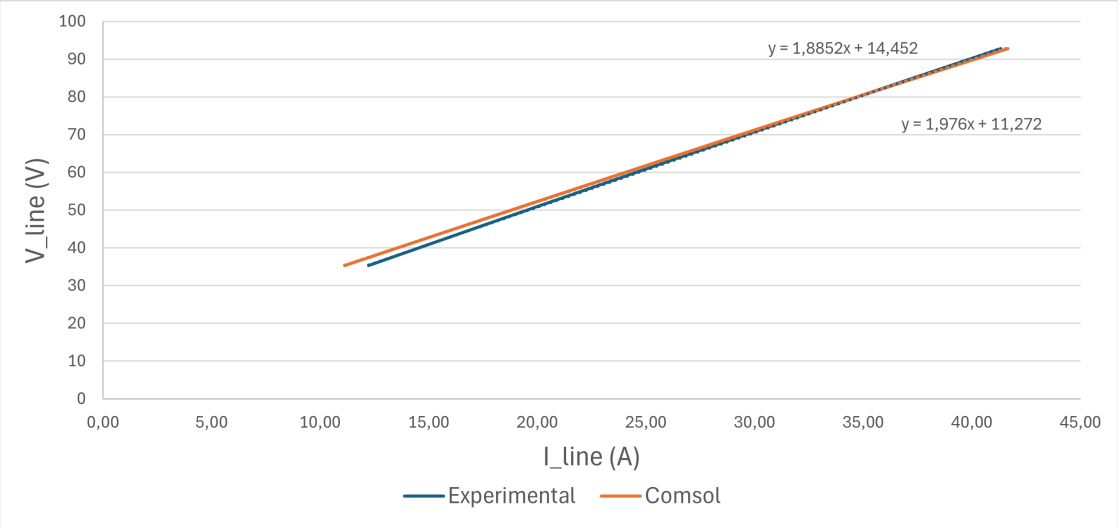


**Figure 58:** Locked-Rotor Characteristic: Final Model

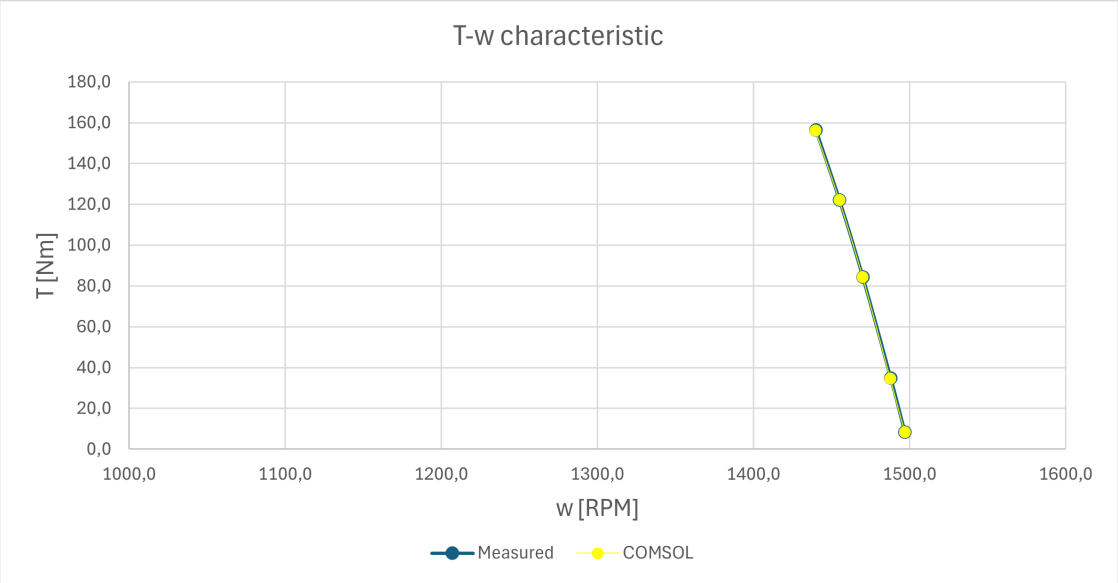


**Figure 59:** Mechanical Characteristic: Final Model

**Table 11:** Parameters of the Equivalent Circuit (T=25°C, f=50 Hz): Final Model

| **Parameter** | **Experimental** | **Comsol** | |
|---|---|---|---|
| Rs | 0.56 | 0.56 | Ω |
| Rr′ | 1.20 | 1.08 | Ω |
| Xls=Xlr′ | 1.72 | 1.79 | Ω |
| V0 | 11.3 | 14.5 | V |
| Xm′ | 50.07 | 50.3 | Ω |
| Riron′ | 963.34 | 966.1 | Ω |

# 5 Simulations in Cryogenic Conditions

In this section, it will be analyzed the operation of the motor in cryogenic conditions ($-196\ ^{\circ}C$). Cryogenic operation has a very significant effect on the electrical properties of conductive materials. At the liquid nitrogen temperature (–196°C), copper and aluminum resistivity decreases approximately by an order of magnitude compared with their room-temperature values. This has a direct effect on current distribution in the motor, the Joule losses, and produced torque. Although it may be thought that the parameters most affected are mainly resistive (stator resistance, rotor resistance and iron losses resistance), this is not the case. Changing the temperature of such a large gradient, also affects the inductive parameters of the equivalent circuit. For example, the leakage inductances vary due to the $K_L$ coefficient relative to skin effect which undergoes a not negligible change as shown in Section3.2.1. Furthermore, in the *"Iron Loss Characterization in Laminated Cores at Room and Liquid Nitrogen Temperature"*[5] article, where it is analyzed how the transversal parameters vary at cryogenic temperatures, it is shown how also that the core $B-H$ characteristic undergoes changes between these two states:

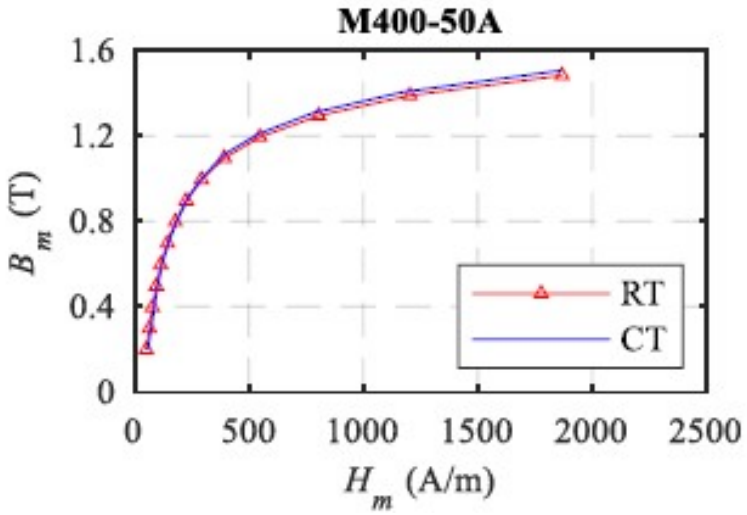


**Figure 60:** The BH curve of $M400-50A$ at 50 Hz, room (RT) and cryogenic (CT) temperature.[5]

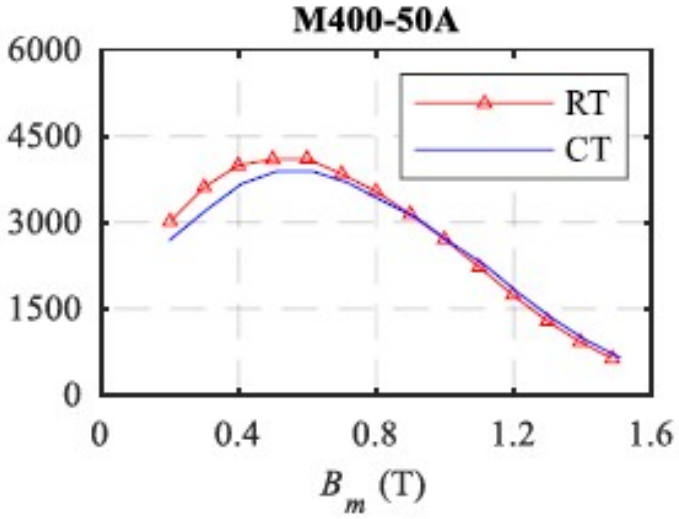


**Figure 61:** The relative permeability of $M400 - 50A$ at 50 Hz, room (RT) and cryogenic (CT) temperature[5].

It is evident from the figures that the magnetizing characteristic of iron is independent for most of the values of $H_m$ from temperature. In fact, under cryogenic conditions the maximum variation of magnetic permeability is $5.2\%$(Fig.61). It can therefore be concluded that by moving from reference conditions to cryogenic conditions, the variation in the magnetizing characteristic of the material under study is negligible.
Obviously the same can not be said about the resistance of stator windings and rotor bars, for which there is a substantial variation of almost an order of magnitude compared to conventional values. The variation of these parameters is due to the resistivity, which decreases considerably.
Regarding the copper in the stator, its resistivity $\rho_{cu}$ changes mostly linearly with the temperature, according to the following well known expression:

$$\rho_2(T) = \rho_1 \cdot \frac{|T_{cr}| + T_2}{|T_{cr}| + T_1} \tag{63}$$

Where $T_{cr}$ is the critical temperature of the material (i.e. for copper $T_{cr,cop} = -235°C$ and for aluminum $T_{cr,al} = -225°C$); $T_1$ and $T_2$ are the referring temperatures (in this case ambient and cryogenic temperature); $\rho_1$ and $\rho_2$ are the resistivities of the material at $T_1$ and $T_2$.

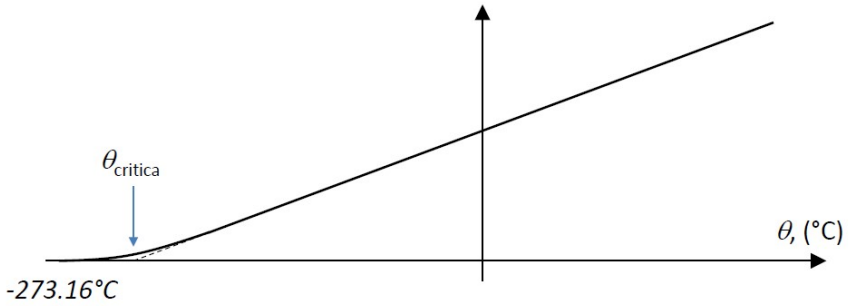


**Figure 62:** Linear Variation of Resistivity $\rho$ [$\Omega \cdot m$] with temperature $\theta$ [$^{\circ}C$].

At 25°C the resistivity of copper is:

$$\rho_{cop}(25\ ^{\circ}C) = 1.75 \cdot 10^{-8}\ \Omega \cdot m \tag{64}$$

Thus, at -196°C it will be:

$$\rho_{cop}(-196\ ^{\circ}C) = 2.63 \cdot 10^{-9}\ \Omega \cdot m \tag{65}$$

With a relative variation of $-84.97\%$ respect to the conventional one.
Similarly for the rotor resistance, it will vary due to the decrease in resistivity of aluminum as a function of temperature. Unlike copper, however, aluminum has non-linearity in its resistivity if the temperature varies considerably:

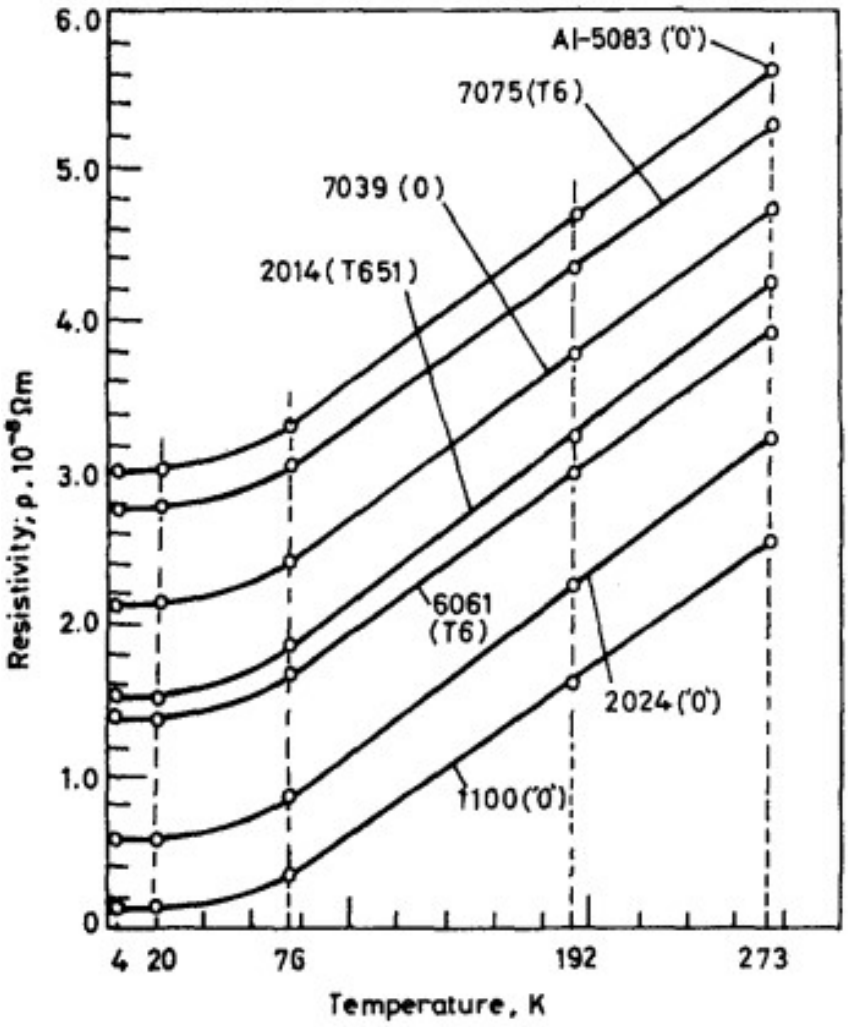


**Figure 63:** Resistivity of some Aluminum Alloys with Temperature [14].

Thus, it will be:

$$\rho_{Al}(25\ ^\circ C) = 2.88 \cdot 10^{-8}\ \Omega \cdot m \tag{66}$$

$$\rho_{Al}(-196\ ^\circ C) = 3.1 \cdot 10^{-9}\ \Omega \cdot m \tag{67}$$

In *"Iron Loss Characterization in Laminated Cores at Room and Liquid Nitrogen Temperature"*[5] it is also explained how iron losses vary when working under cryogenic conditions, thus determining a variation in the transversal resistance. The study adopted an energy-based loss separation approach using a two-term loss model, which divides the total losses into hysteresis and global dynamic components. The study showed that the core losses tend to increase when the temperature is reduced to cryogenic levels, particularly the dynamic component. The reason for this is the reduction of the resistivity of iron from ambient to cryogenic temperatures, which leads to an increase in eddy currents.

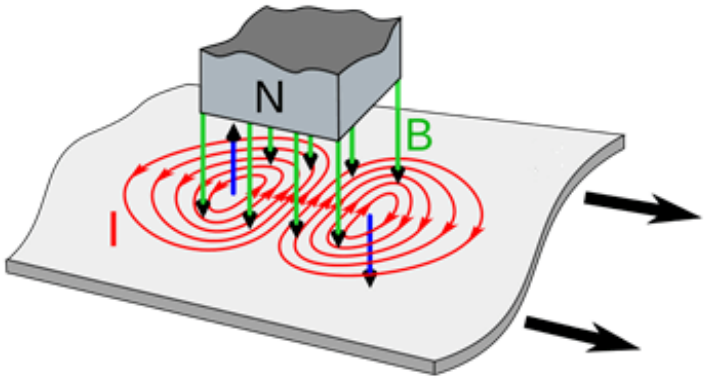


**Figure 64:** Eddy Currents

For instance, for M400-50A, with a magnetic induction field of $0.5\ T$ the relative increase of iron losses goes from $\approx 16\%$(at 50 Hz) to $\approx 22\%$ (at 400 Hz). At $1\ T$ the increase goes from $\approx 15\%$ to $\approx 27\%$, and for $1.5\ T$ it goes from $\approx 15\%$ to $\approx 33\%$.
In COMSOL, the temperature variation was modeled by appropriately varying the electrical resistivity of the various machine components, thus modifying their electromagnetic behavior and losses by joule effect. However, this operation does not intrinsically take into account the increase in iron losses. To appreciate their increase in COMSOL, the coefficient "$k_h$" of the Steinmetz equation must be adjusted to obtain the desired losses. Therefore, according to the literature[3][12], an increase in iron losses of $10\%$ is considered.

## 5.1 Implementation of Cryogenic Motor in COMSOL Multiphysics

To implement the cryogenic motor in Comsol, it will be sufficient to take as a starting point the conventional model analyzed above. It will simply be modified in the following ways:

- copper resistivity will be changed from $\rho_{Cu,80°C} = 2.12 \cdot 10^{-8}\ \Omega \cdot m$ to $\rho_{Cu,-196°C} = 2.63 \cdot 10^{-9}\ \Omega \cdot m$
- aluminum resistivity will be changed from $\rho_{Al,80°C} = 3.51 \cdot 10^{-8}\ \Omega \cdot m$ to $\rho_{Al,-196°C} = 3.1 \cdot 10^{-9}\ \Omega \cdot m$

All the precautions that allowed to have a conventional model coherent with the real motor will be kept also in this model: the external circuit which takes into account the leakage inductances that are not included in the 2D FEM, the use of the coefficients $k_{al}$ and $k_{cu}$ to take into

account the resistances of stator end-windings and rotor end-rings, as well as the calibrations of the air-gap and rotor bridges.

An important computational aspect to be considered is the timing of simulations. In cryogenic conditions, the time constant of the equivalent circuit of the motor will strongly increase being it qualitatively: $\tau = L/R$. To face this tricky "problem", the three-voltage circuit which feeds the machine has been multiplied by a ramp, allowing the electrical quantities to be progressively increased. The same has been done for the load torque set during the tests. In this way, excessively long transients are avoided and a smoother simulation is obtained:

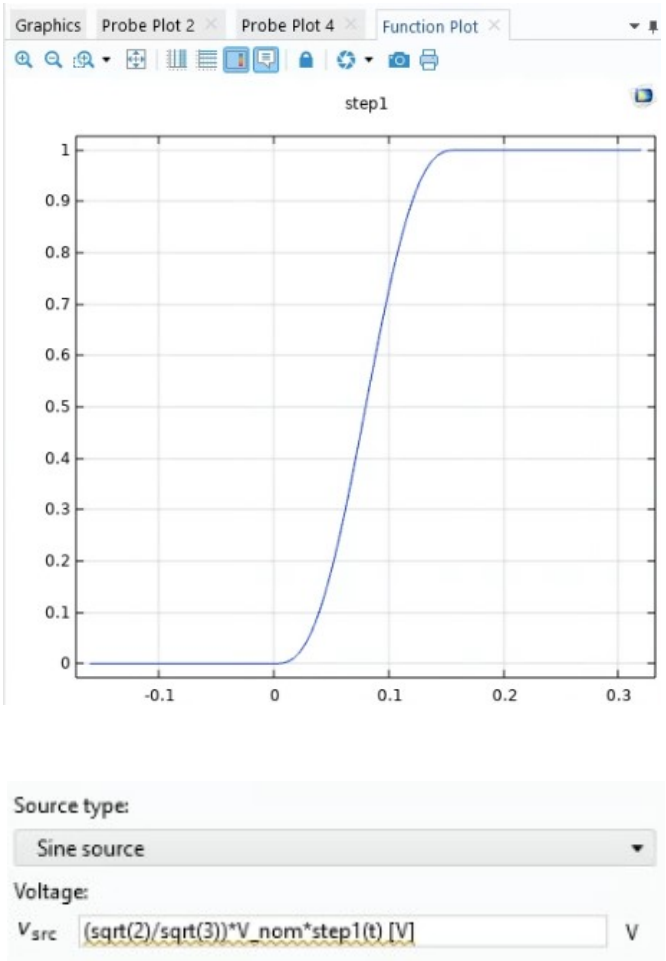


**Figure 65:** Comsol Interface: Step1(t) as a Function of Time [s] multiplied by the Voltage Source

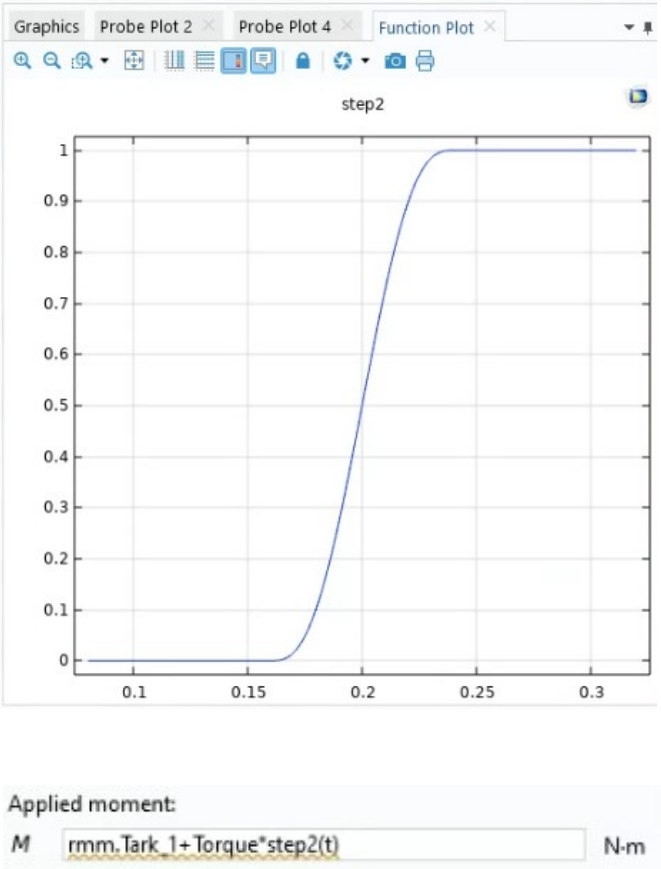


**Figure 66:** Comsol Interface: Step2(t) as a Function of Time [s] multiplied by the Load Torque

## 5.2 Simulation Results of the Cryogenic Model

In order to properly assess the performance effect of cryogenic operation on the motor, it is important to examine the mechanical characteristic of the motor in the stable region. The way in which this characteristic has been obtained is exactly the same used during the standard simulations: applying a load torque and imposing a 3-phase voltage source,the speed obtained in output at the mechanical equilibrium is evaluated.

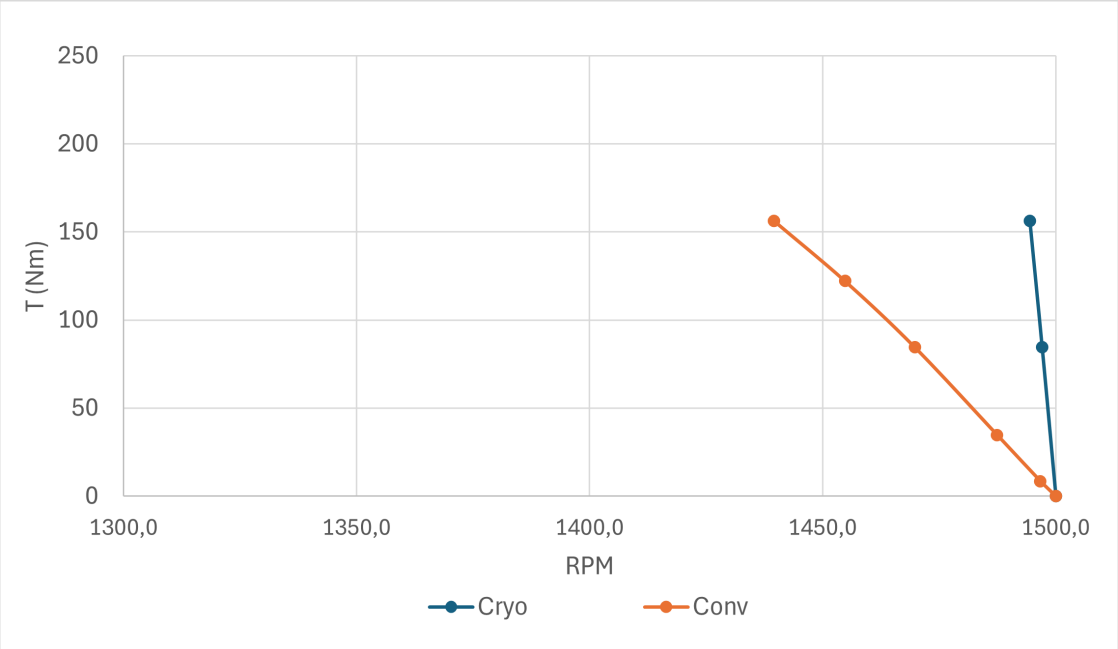


**Figure 67:** Stable Part of the Mechanical Characteristic from Comsol: Comparison between Conventional and Cryogenic Outputs.

The results, in accordance with what was theoretically expected, show a crogenic graph much steeper than the conventional one. Obviously, this is a manifestation of the fact that the torque speed characteristic in an induction motor strongly depends on the rotor resistance value (Fig.48). For the nominal torque of $84.5\ Nm$, for example, the speed goes from the rated one of $1470\ rpm$ to the new one equal to $1497.1\ rpm$ ($+2\%$). This increases markedly the power production (and hence the specific power). For a torque value of $156.4\ Nm$ conventionally it is obtained a speed of $1439.6\ rpm$ and the new one is of $1494.5\ rpm$, with an increase of $\approx 4\%$. The simulations performed under cryogenic conditions, moreover, reveal that the maximum torque reaches values more than two times higher than those observed in the conventional model at ambient temperature: $T_{max,cryo} \approx 920\ Nm$ and $T_{max,conv} \approx 400\ Nm$. This is also in line with what has been stated in the scientific literature [12] [3].

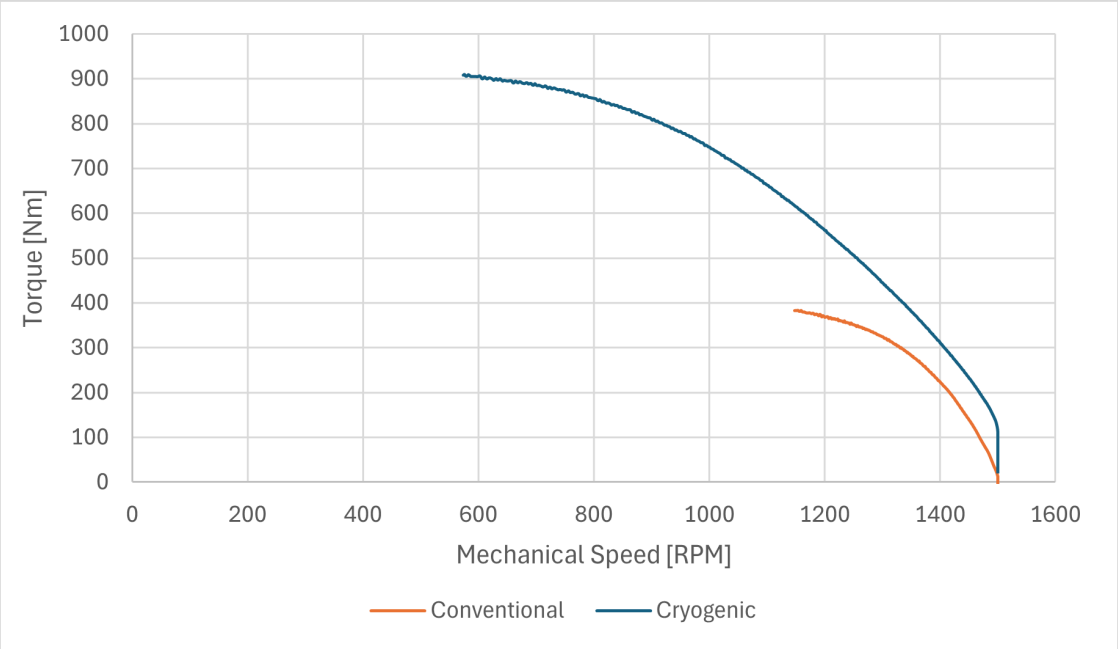


**Figure 68:** Maximum Values of the Mechanical Characteristics of the Cryogenic and Conventional Models.

Another interesting aspect to consider is efficiency and how it varies. Theoretically, an increase in efficiency is expected due to the fact that, at the same torque, the motor works at higher speeds. This implies that the amount of input power to be converted into mechanical power is greater than a conventional motor, reducing losses. In addition, a low resistivity also reduces the joule losses, contributing to increase the efficiency. However, as been said previously, the iron losses are expected to be higher (especially eddy currents) due to the increase in the electrical conductivity of the core[5].
In correspondence with the nominal torque (84.5 Nm), the efficiency is analyzed by studying the evolution of the input electrical power and the mechanical output for both the conventional and the cryogenic models:

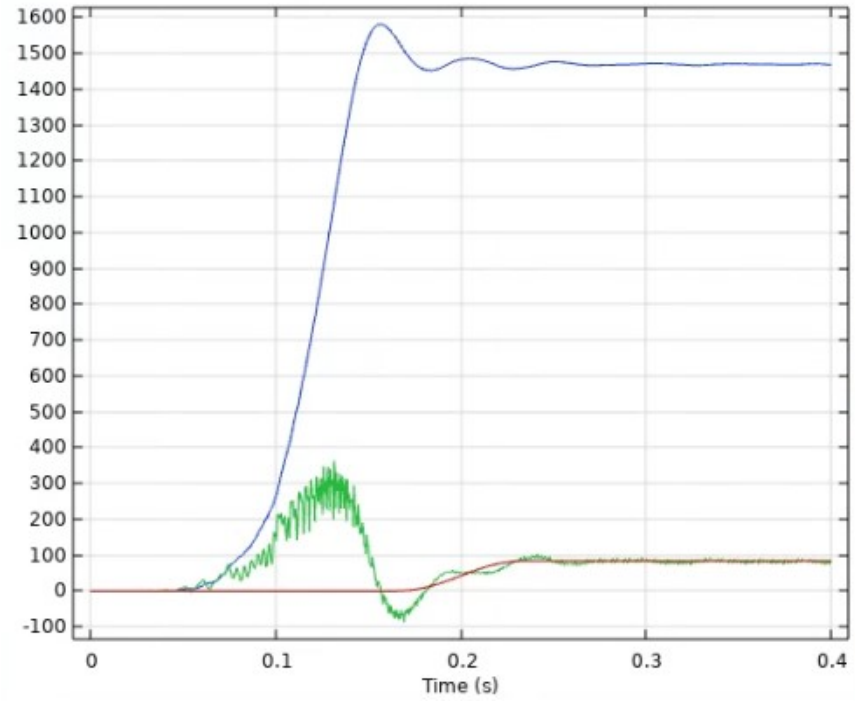


**Figure 69:** CONVENTIONAL MODEL: Evolution in Time of Mechanical Speed (blue) [rpm], Load Torque (red) [Nm] and Electromechanical Torque (green) [Nm].

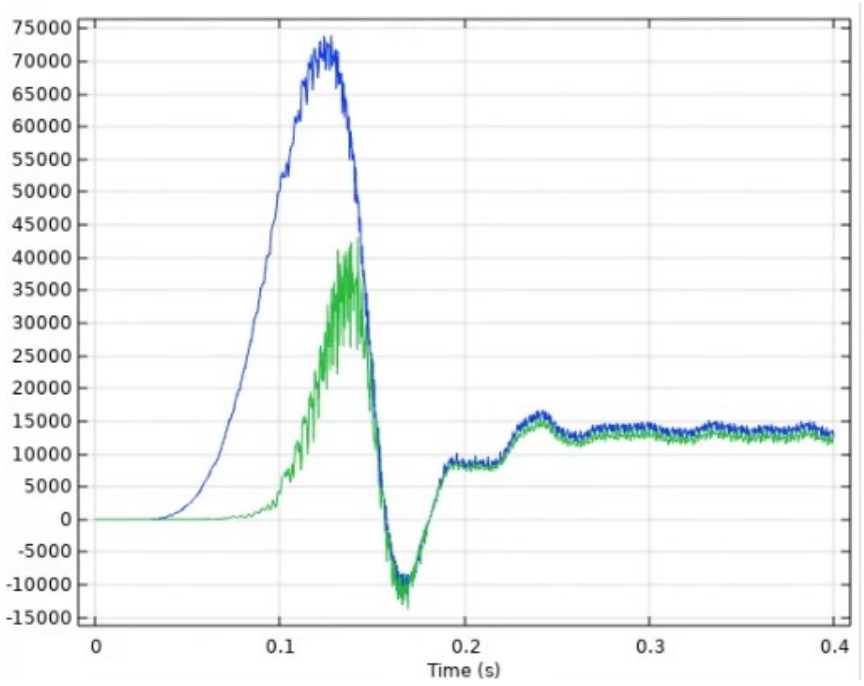


**Figure 70:** CONVENTIONAL MODEL: Evolution in Time of Input Electric Power (blue) [W] and Output Mechanical Power (green) [W].

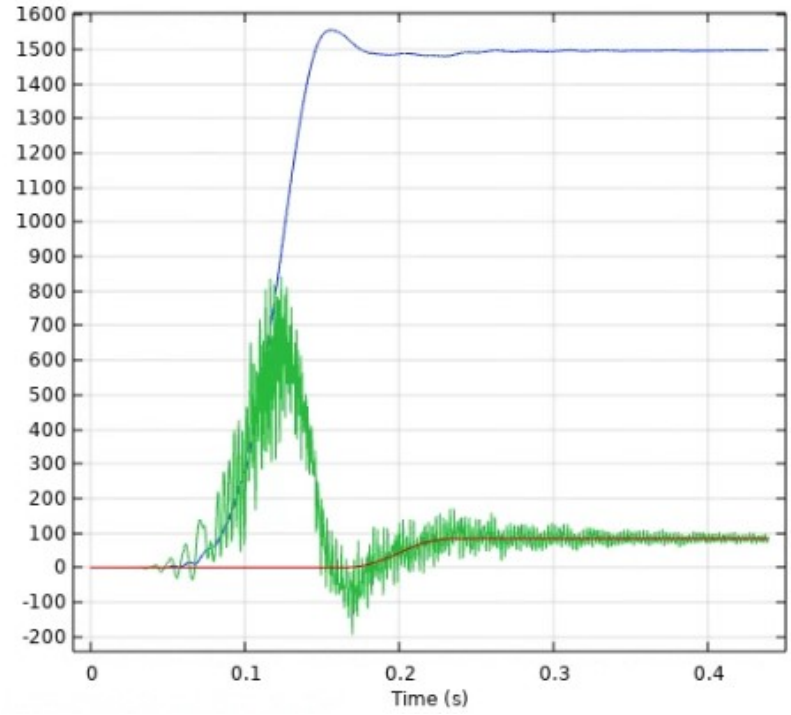


**Figure 71:** CRYOGENIC MODEL: Evolution in Time of Mechanical Speed (blue) [rpm], Load Torque (red) [Nm] and Electromechanical Torque (green) [Nm].

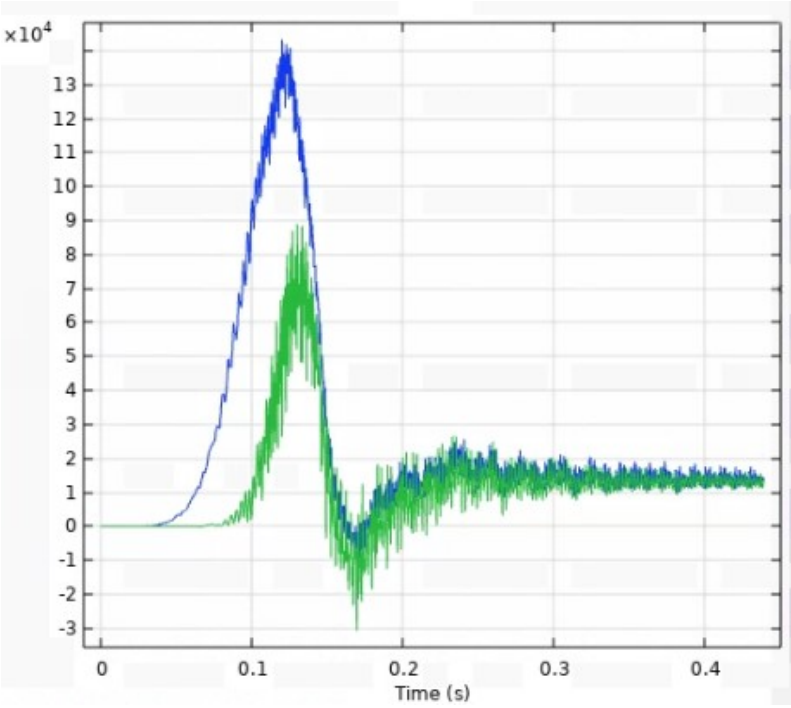


**Figure 72:** CRYOGENIC MODEL: Evolution in Time of Input Electric Power (blue) [W] and Output Mechanical Power (green) [W].

Before calculating the efficiency, it is interesting to make some considerations: first of all, the graphs seem to accurately reflect the physical behavior of the start of an asynchronous motor, with an initial transient and a subsequent stabilization. The torque ripple, which then translates into power ripple, is due in part to computational factors and in part to the high accuracy of finite element simulation. In this way, the spatial distribution of stator slots or rotor bars, also generates an evident ripple. In fact, it is more emphasized in the simulation under cryogenic conditions, since strong magnetomotive forces are involved. The slight final oscillation, on the other hand, could be due to computational factors, stator windings harmonics, or a non-total stabilization of the rotor speed.
As already mentioned, the mechanical losses are not taken into account in this study. The iron losses, on the other hand, are calculated in a subsequent study: *"Time to Frequency Losses"*. Therefore, in the calculation of efficiency they must be added to the input power:

$$\eta_{conv}|_{84.5\ Nm} = \frac{P_{mech,conv}}{P_{in,conv} + P_{iron,conv}} \approx \frac{13}{13.74 + 1.1} \cdot \frac{kW}{kW} \approx 87.6\% \tag{68}$$

$$\eta_{cryo}|_{84.5\ Nm} = \frac{P_{mech,cryo}}{P_{in,cryo} + P_{iron,cryo}} \approx \frac{13.25}{13.9 + 1.2} \cdot \frac{kW}{kW} \approx\ 88.8\% \tag{69}$$

## 5.3 Comparison of the Performances of the Two Models

Further to what has been said so far, the substantial differences in the motors performance are summarized below:

- at the same torque ($84.5; Nm$), the rotor speed is increased (i.e. from $\omega_{r,conv} = 1470\ rpm$ to $\omega_{r,cryo} = 1497.1\ rpm$ ($+2\%$);
- increase of maximum value of produced torque of more than two times, going from $T_{max,conv} \approx 400\ Nm$ to $T_{max,cryo} \approx 920\ Nm$;
- increase of efficiency (i.e. at nominal torque it goes from $\eta_{conv} = 87.6\%$ to $\eta_{cryo} = 88.8\%$);
- increase of output power: for the nominal torque, it goes from $P_{mech,conv} = \ 13kW$ to $P_{mech,cryo} = 13.3\ kW$. At $T = 156.4\ Nm$ the mechanical power changes from $P_{mech,conv} = 23.6\ kW$ to $P_{mech,cryo} = \ 24.5\ kW$.

**Table 12:** Comparison of Performances at Nominal Torque (84.5 Nm) between Conventional and Cryogenic Models

| **Parameter** | **Conventional Temperature** | **Cryogenic Temperature** | |
|---|---|---|---|
| $Speed$ (RPM) | 1470 | 1497.1 | $+1.8\%$ |
| $P_{mech}$ (kW) | 13 | 13.25 | $+1.9\%$ |
| $Eff.$ (%) | 87.6 | 88.8 | $+1.4\%$ |
| $P_{iron}$ (W) | 1092.7 | 1202 | $+10\%$ |
| $P_{J,stat}$ (W) | 446.3 | 113.8 | $-74.5\%$ |
| $P_{J,rot}$ (W) | 379.5 | 195.8 | $-48.4\%$ |

The relatively small improvement in efficiency and output power at cryogenic temperatures is in part because simulations were conducted at rated torque. Here, the standard motor is already optimized. However, the successes achieved are as predicted and confirm that cryogenic cooling is able to provide measurable benefits, even more exploitable if it is applied on machines designed for this kind of use.

# 6 Conclusions

This thesis is focused on the modeling, simulation, and experimental verification of a 15 kW squirrel-cage induction motor at ambient and cryogenic temperatures. The finite element approach, precisely COMSOL Multiphysics, is used to successfully simulate the electromagnetic performance of the machine, taking into account significant physical phenomena such as skin effect, rotor end-ring effects, and temperature-dependent variation of the material properties. The model is calibrated and verified according to standard no-load, locked-rotor, and load tests available for the real motor, following IEEE Std 112-1991 procedures. The results show satisfactory match between the simulation and the measured results, especially after critical parameters such as air-gap length and rotor end-rings resistance have been calibrated.

Once validated, the model is adapted for cryogenic use by scaling the electrical resistivity of aluminum and copper down to their low-temperature values. The results obtained by this new model show that cryogenic cooling generates measurable improvements in torque, efficiency, and power density. In particular, the torque-speed curve of the cryogenic motor is higher and steeper, with a maximum torque more than twice that of the ambient motor. Efficiency gains at rated torque, although modest, are in line with the scientific literature and show the potential of this technology.

Finally, the motor investigated in this paper was not initially intended to be used in cryogenic environments. Thus, the results achieved must be regarded as conservative estimates of what the gains could be with a machine specifically designed for low-temperature use, with optimized stator and rotor geometry.

In conclusion, the results show that there is an increase in performance to which an induction motor is subjected when cooled at VLT. Moreover, they confirm the use of FEM as a validable and flexible tool to simulate electromagnetic phenomena in advanced motor design.

# 7 References

# References

[1] João Arnaud, João F. P. Fernandes, and Paulo J. Costa Branco. "Use of Bulk Superconductors in the Excitation System of Low-Speed Synchronous Generators". In: *IEEE Transactions on Applied Superconductivity* 31.5 (2021), pp. 1–6. DOI: 10.1109/TASC.2021.3054721.

[2] Nicola Bianchi. *Electrical Machine Analysis Using Finite Elements*. Version Date: 20110713. Boca Raton, FL: CRC Press, Taylor & Francis Group, 2005. ISBN: 978-1-4200-5787-4. URL: http://www.crcpress.com.

[3] Marco Biasion et al. "A Comparison of Cryogenic-Cooled and Superconducting Electrical Machines". In: *2021 IEEE Energy Conversion Congress and Exposition (ECCE)*. 2021, pp. 4045–4052. DOI: 10.1109/ECCE47101.2021.9595182.

[4] Marco Biasion et al. "Design and Analysis of High-Speed Induction Machines for Submerged Cryogenic Pumps". In: *2023 IEEE International Electric Machines  Drives Conference (IEMDC)*. 2023, pp. 1–7. DOI: 10.1109/IEMDC55163.2023.10238967.

[5] Marco Biasion et al. "Iron Loss Characterization in Laminated Cores at Room and Liquid Nitrogen Temperature". In: *2022 IEEE Energy Conversion Congress and Exposition (ECCE)*. 2022, pp. 1–8. DOI: 10.1109/ECCE50734.2022.9948041.

[6] Marco Biasion et al. "Superconductivity and its Application in the Field of Electrical Machines". In: *2021 IEEE International Electric Machines  Drives Conference (IEMDC)*. 2021, pp. 1–7. DOI: 10.1109/IEMDC47953.2021.9449545.

[7] Aldo Boglietti, Andrea Cavagnino, and Mario Lazzari. "Computational Algorithms for Induction Motor Equivalent Circuit Parameter Determination—Part II: Skin Effect and Magnetizing Characteristics". In: *IEEE Transactions on Industrial Electronics* 58.9 (2011), pp. 3734–3740. DOI: 10.1109/TIE.2010.2084975.

[8] Aldo Boglietti, Andrea Cavagnino, and Mario Lazzari. "Computational Algorithms for Induction Motor Equivalent Circuit Parameter Determination—Part II: Skin Effect and Magnetizing Characteristics". In: *IEEE Transactions on Industrial Electronics* 58.9 (2011), pp. 3734–3740. DOI: 10.1109/TIE.2010.2084975.

[9] Aldo Boglietti, Andrea Cavagnino, and Mario Lazzari. "Computational Algorithms for Induction-Motor Equivalent Circuit Parameter Determination—Part I: Resistances and Leakage Reactances". In: *IEEE Transactions on Industrial Electronics* 58.9 (2011), pp. 3723–3733. DOI: 10.1109/TIE.2010.2084974.

[10] Aldo Boglietti, Andrea Cavagnino, and Mario Lazzari. "Modelling of the closed rotor slot effects in the induction motor equivalent circuit". In: *2008 18th International Conference on Electrical Machines*. 2008, pp. 1–4. DOI: 10.1109/ICELMACH.2008.4799834.

[11] Ion Boldea and Syed A. Nasar. *The Induction Machines Design Handbook*. Second. Electric Power Engineering Series. Boca Raton, FL, USA: CRC Press, Taylor & Francis Group, 2010. ISBN: 978-1-4200-6668-5.

[12] Luís F. D. Bucho et al. "Experimental Assessment of Cryogenic Cooling Impact on Induction Motors". In: *IEEE Transactions on Energy Conversion* 37.4 (2022), pp. 2629–2636. DOI: 10.1109/TEC.2022.3183939.

[13] Radoslav Cipín and Josef Běloušek. "Influence of a Skin Effect in the Squirrel Cage on a Speed-Torque Characteristics of the Induction Motor". In: *Proceedings of the Faculty of Electrical Engineering and Communication, Brno University of Technology*. Supervised by Miroslav Patočka. Brno, Czech Republic: Faculty of Electrical Engineering and Communication, Brno University of Technology, 2025. eprint: 102/06/1036, 0021630516. URL: mailto:xcipin00@stud.feec.vutbr.cz, %20xbelou00@stud.feec.vutbr.cz.

[14] A.F. Clark, G.E. Childs, and G.H. Wallace. "Electrical resistivity of some engineering alloys at low temperatures". In: *Cryogenics* 10.4 (1970), pp. 295–305. ISSN: 0011-2275. DOI: https://doi.org/10.1016/0011-2275(70)90056-1. URL: https://www.sciencedirect.com/science/article/pii/0011227570900561.

[15] European Commission et al. *Flightpath 2050 – Europe's vision for aviation – Maintaining global leadership and serving society's needs*. Publications Office, 2011. DOI: doi/10.2777/50266.

[16] L. Dlugiewicz et al. "Electrical motor for liquid gas pump". In: *International Symposium on Power Electronics, Electrical Drives, Automation and Motion, 2006. SPEEDAM 2006.* 2006, pp. 311–316. DOI: 10.1109/SPEEDAM.2006.1649790.

[17] D.I. Driscoll. "A review of superconducting motor technology development". In: *2001 IEEE Power Engineering Society Winter Meeting. Conference Proceedings (Cat. No.01CH37194)*. Vol. 2. 2001, 438–441 vol.2. DOI: 10.1109/PESW.2001.916881.

[18] H. Falkner and S. Holt. "Walking the Torque: Proposed Work Plan for Energy-Efficiency Policy Opportunities for Electric Motor-Driven Systems". In: *IEA Energy Papers* 2011/08 (2011). DOI: 10.1787/5kgg52g5bzmx-en. URL: https://doi.org/10.1787/5kgg52g5bzmx-en.

[19] GIIGNL. *Benefits of Liquefied Natural Gas (LNG)*. https://giignl.org/benefits-of-lng-2/. Accessed: 2025-06-24. 2024.

[20] *IEEE Standard Test Procedure for Polyphase Induction Motors and Generators*. Approved December 5, 1991. Revision of IEEE Std 112-1984. New York, NY, USA: Institute of Electrical and Electronics Engineers, 1991.

[21] S.S. Kalsi. "HTS ship propulsion motors". In: *IEEE Power Engineering Society General Meeting, 2004.* 2004, 2047–2048 Vol.2. DOI: 10.1109/PES.2004.1373238.

[22] Hui Min Kim et al. "Design of Cryogenic Induction Motor Submerged in Liquefied Natural Gas". In: *IEEE Transactions on Magnetics* 54.3 (2018), pp. 1–4. DOI: 10.1109/TMAG.2017.2751099.

[23] Jerzy Kolowrotkiewicz et al. "FE analysis of induction motor working in cryogenic temperature". In: *COMPEL: The International Journal for Computation and Mathematics in Electrical and Electronic Engineering* 26 (Aug. 2007), pp. 952–964. DOI: 10.1108/03321640710756294

[24] Philip R. LeGoy. "Utility Requirements for Power Recovery in the Cryogenic and Chemical Industry Using Variable Frequency Drives in the Regenerative Mode". In: *Proceedings of the Cryogenic and Chemical Industry Power Recovery Conference*. Presented by Ebara R&D, 1998 testing at a cryogenic–chemical process facility. Ebara International Corporation. Sparks, Nevada, USA, Aug. 1999.

[25] J. Lloberas et al. "A review of high temperature superconductors for offshore wind power synchronous generators". In: *Renewable and Sustainable Energy Reviews* 38 (2014), pp. 404–414. ISSN: 1364-0321. DOI: https://doi.org/10.1016/j.rser.2014.05.003. URL: https://www.sciencedirect.com/science/article/pii/S1364032114003190.

[26] Farshid Mahmouditabar and Nick Baker. "A Review on the Effect of Electrical Steel Manufacturing Processes on the Performance of Electric Machines". In: *Energies* 16.24 (2023). ISSN: 1996-1073. DOI: 10.3390/en16247954. URL: https://www.mdpi.com/1996-1073/16/24/7954.

[27] Fabrizio Marignetti and Guido Rubino. "Perspectives on Electric Machines with Cryogenic Cooling". In: *Energies* 16.7 (2023). ISSN: 1996-1073. DOI: 10.3390/en16072994. URL: https://www.mdpi.com/1996-1073/16/7/2994.

[28] Takashi Nakamura et al. "Development of a superconducting magnet for nuclear magnetic resonance using bulk high-temperature superconducting materials". In: *Concepts in Magnetic Resonance* 31 (Jan. 2006), pp. 65–70.

[29] Muhamad Omar et al. "Upgrading for overhead crane anti-sway method using variable frequency drive". In: *Bulletin of Electrical Engineering and Informatics* 11 (Aug. 2022), pp. 1837–1844. DOI: 10.11591/eei.v11i4.3731.

[30] Mehmet Burak Özakın and Serkan Aksoy. "Application of Magneto-Quasi-Static Approximation in the Finite Difference Time Domain Method". In: *IEEE Transactions on Magnetics* 52.8 (2016), pp. 1–9. DOI: 10.1109/TMAG.2016.2535415.

[31] Johannes H. J. Potgieter and Maarten J. Kamper. "Calculation Methods and Effects of End-Winding Inductance and Permanent-Magnet End Flux on Performance Prediction of Nonoverlap Winding Permanent-Magnet Machines". In: *IEEE Transactions on Industry Applications* 50.4 (2014), pp. 2458–2466. DOI: 10.1109/TIA.2013.2295468.

[32] James Schilling, Narelle Hillier, and N. Foroozani. "What have we learned from high-pressure experiments on Cu-oxide and Fe-based superconductors?" In: *Journal of Physics Conference Series* 449 (July 2013), pp. 2021–. DOI: 10.1088/1742-6596/449/1/012021.

[33] R. Shively and H. Miller. "Development of a submerged winding induction generator for cryogenic applications". In: *Conference Record of the 2000 IEEE International Symposium on Electrical Insulation (Cat. No.00CH37075)*. 2000, pp. 243–246. DOI: 10.1109/ELINSL.2000.845498.

[34] Francisco Ferreira da Silva, João F. P. Fernandes, and Paulo Jose da Costa Branco. "Barriers and Challenges Going from Conventional to Cryogenic Superconducting Propulsion for Hybrid and All-Electric Aircrafts". In: *Energies* 14.21 (2021). ISSN: 1996-1073. DOI: 10.3390/en14216861. URL: https://www.mdpi.com/1996-1073/14/21/6861.

[35] Jungwook Sim et al. "Development of a HTS squirrel cage induction motor with HTS rotor bars". In: *IEEE Transactions on Applied Superconductivity* 14.2 (2004), pp. 916–919. DOI: 10.1109/TASC.2004.830317.

[36] Jungwook Sim et al. "Test of an induction motor with HTS wire at end ring and bars". In: *IEEE Transactions on Applied Superconductivity* 13.2 (2003), pp. 2231–2234. DOI: 10.1109/TASC.2003.813053.

[37] G. Snitchler, B. Gamble, and S.S. Kalsi. "The performance of a 5 MW high temperature superconductor ship propulsion motor". In: *IEEE Transactions on Applied Superconductivity* 15.2 (2005), pp. 2206–2209. DOI: 10.1109/TASC.2005.849613.

[38] Taesoo Song, Akira Ninomiya, and Takeshi Ishigohka. "Experimental Study on Induction Motor With Superconducting Secondary Conductors". In: *IEEE Transactions on Applied Superconductivity* 17.2 (2007), pp. 1611–1614. DOI: 10.1109/TASC.2007.897834.

[39] Ludovic Ybanez et al. "ASCEND: The first step towards cryogenic electric propulsion". In: *IOP Conference Series: Materials Science and Engineering* 1241 (May 2022), p. 012034. DOI: 10.1088/1757-899X/1241/1/012034.